INVESTIGATION OF L-CYSTINE ASSISTED Cu_3BiS_3 SYNTHESIS FOR ENERGETICALLY AND ENVIRONMENTALLY IMPROVED INTEGRATION AS THIN-FILM SOLAR CELL P-TYPE SEMICONDUCTOR ABSORBER

by

BRIAN D. VIEZBICKE

A Dissertation submitted to the

Graduate School-New Brunswick

Rutgers, The State University of New Jersey

in partial fulfillment of the requirements

for the degree of

Doctor of Philosophy

Graduate Program in Materials Science and Engineering

written under the direction of

Dunbar P. Birnie, III

and approved by

_____

_____

_____

_____

New Brunswick, New Jersey

January, 2015

ABSTRACT OF THE DISSERTATION

INVESTIGATION OF L-CYSTINE ASSISTED Cu_3BiS_3 SYNTHESIS FOR ENERGETICALLY AND ENVIRONMENTALLY IMPROVED INTEGRATION AS THIN-FILM SOLAR CELL P-TYPE SEMICONDUCTOR ABSORBER

By BRIAN D. VIEZBICKE

Dissertation Director:

Dr. Dunbar P. Birnie, III

Solar photovoltaic energy technology is increasingly implemented in response to continuously growing global energy needs. While legacy technology utilizing silicon has captured much of the market, thin-film solar modules are projected to rise particularly in the U.S. production sector. Current materials utilized in production and deployment encounter resource and environmental impact constraints. This research investigates the viably controllable synthesis of multi-crystalline copper bismuth sulfide for potential use as an absorber layer in thin-film solar cells and early investigation of thin-film growth parameters which may enable a cost-effective route to full scale production of epitaxial copper bismuth sulfide films. The first step of this investigation has entailed a novel route for the solvo-thermally grown Cu_3BiS_3 films facilitated by L-cystine as a sulfur

donating and complexing agent. In the characterization of the nanoparticulate product UV-VIS spectra were analyzed via the Tauc method of bandgap interpolation. The validity of the Tauc method in application to polycrystalline films has been investigated and proven to be robust for the material class. This justifies the bandgap assessment of the subject material and provides support for wider use of the method. With the synthesis method established, the reaction was transferred to a custom built continuous flow reactor to explore this process and help understand its capabilities and limits with respect to producing single layers for an eventual photovoltaic cell stack. Though the published work has established novel chemistry, the need to deposit and/or grow a functional p-type layer for further characterization and eventual device incorporation is key to the material evolution. First evidence of continuous flow micro-reactor deposition of Cu_3BiS_3 has been shown with an array of resulting microstructures. The grown microstructures are evaluated with relevance to prior synthesis laboratory procedure and recommendations are made for continuing the pursuit of a functional Cu_3BiS_3 coating mediated by L-cystine in a continuous flow micro-reactor.

ACKNOWLEDGEMENT

I am indebted and deeply thankful to my advisor Dr. Dunbar P. Birnie, III for his insight, guidance, collaboration, and trust during my PhD research. His excitement for the topic of my dissertation as well the other fields together in which we worked was beneficial to my mind and my soul. His commitment to my growth and success was vital and unwavering.

I would like to extend my sincere thanks to my committee members Dr. Frederic Cosandey, Dr. George Celler, Dr. Piotr Piotrowiak and Robert Prunchak for their critical input and evaluation.

I am tremendously thankful to all of the department members who have assisted my over the years and special thanks are owed to a few. With admiration I thank Benjamin Davis and Shane Patel, who in addition to undergraduate class loads contributed significantly to our Tauc analysis assessment via plot digitizations and analyses. I would like to thank Josh Epstein, Sean Langan, and Sukanya Murali for characterizations including some of the XRD and SEM work presented here. It is with appreciation I note Josh Epstein is continuing this work.

I would like to thank additional group members JD Majewski, Saquib Ahmed, Eric Sobolewski, and Vishnu Vijayakumar for much needed scientific and sideline discussions. In particular I thank Vishnu for jumping into a divergent research stream simultaneously and maintaining his infectious sense of optimism.

I am thankful to my department mates Jesse Kohl, Ben Groth, Terence Whalen, Hulya Bicer, Steve Bottiglieri, Paul Mark and Yun Jiang who went beyond intellectual support to make me smile, if only with one of theirs.

I am happy to thank Phyllis Cassell and Claudia Kuchinow for their support and navigation, as well as the Rutgers Materials Science and Engineering Department for funding for through the McLaren and the IGERT Fellowships.

With love I am thankful far beyond these words for the unending patience and support of my mother, father, sister, brother-in-law, and of my wife. With their belief they have buoyed me. I dedicate this work to my wife, Meg, whose beauty, strength and heart I am so very lucky to have found.

There was a sunrise in the lake…

TABLE OF CONTENTS

LIST OF TABLES

LIST OF FIGURES

Chapter 3

Chapter 4

Chapter 5

Chapter 7

CHAPTER 1

Introduction

1.1 Research Impetus

It is increasingly evident to the general populace and quite clear to those who study the climate science literature that our consumption of fossil fuels for energy has set a course of irreversible climate change which will undoubtedly impact global populations in negative manners which we continue to elucidate.[1] Our current global energy consumption resides between the CY 2000 benchmark of 13 TW and the projected consumption of 28 TW in CY 2050.[2,3] A myriad of energy studies predicts anything from peak oil within ten years and an associated rise in global conflict as we fail to meet the 2050 demand projections, to a virtually endless reservoir of petroleum locked in increasingly difficult to breach sub-surface strata. These sub-surface reservoirs which we may yet burn to meet ever increasing demand are the target and subject of many contentious and costly debates, including but not limited to the current fracking investigation.[4] One can easily agree that a population recently topping seven billion individuals, most of whom will learn to consume more energy than the currently industrialized world, needs to find renewable energy sources in order to maintain the current quality of life into the next centuries. This need is increasingly evident as the scientific community's consensus only grows that the consumption of fossil fuels for energy has a set a course of irreversible climate change.

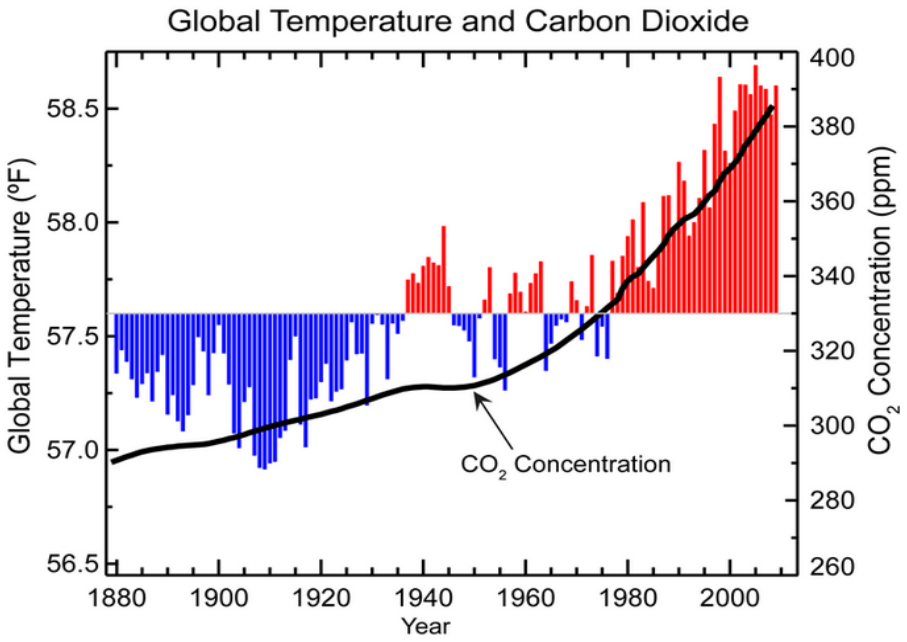

Fig. 1.1.1: Global historic average temperature (ºF) and atmospheric CO_2 concentration (ppm) per year. [5]

Many research and production initiatives exist to support the necessary movement from fossilized to renewable energy sources, including wind, solar, wave and geothermal. As one piece of this new energy puzzle, electricity production from solar energy through photovoltaics continues to harness a vastly untapped energy source. The solar energy striking the Earth (1.7×10^5 TW) is reduced to approximately 600 TW in potentially absorbable terrestrial strike,[6] and with production solar cell efficiencies easily achieving 10% with current technology approximately 60TW of power could be produced. [7] This significantly exceeds the projected demand of the CY 2050.

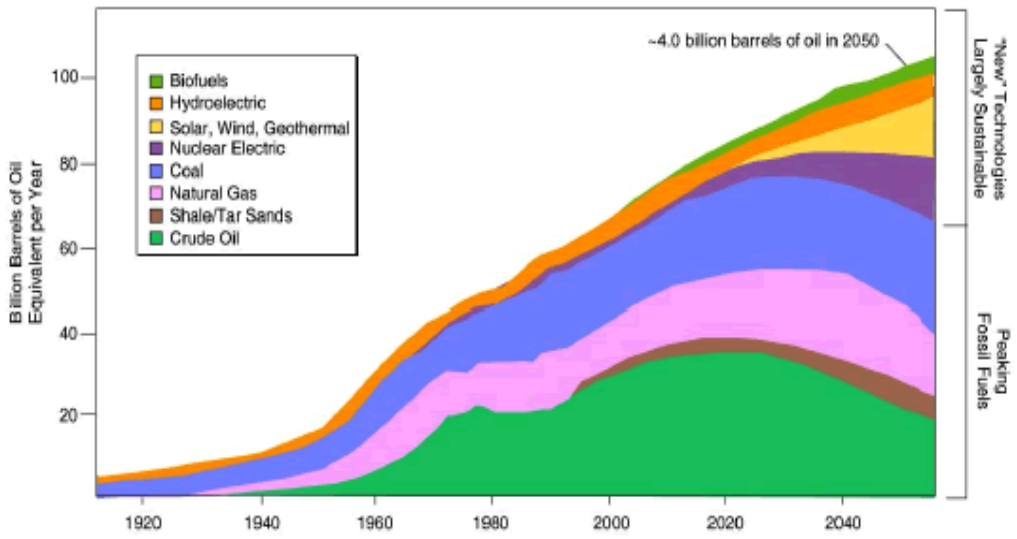

Fig. 1.1.2: Global historic and projected energy sources to 2060 in equivalent billions of barrels of oil per year. [8]

Assuming that solar photovoltaics will provide a portion of the projected future energy demand, the vast quantities of physical devices to be produced will require a more beneficial energy balance and greening of production methods in order to sustain the industry, the population and the environment.[9] Production-ready thin-film solar cell technology often relies on mineral resources already under increasing demand from the digital display and battery sectors. In light of toxicity concerns for device lifecycle and contemporary restrictions on global mineral trade, a replacement absorber semiconductor with suitable bandgap for thin-film photovoltaics is needed to satisfy cost and sustainability concerns. Our early investigation of candidate materials having high abundance and low toxicity resulted in choosing Cu_3BiS_3 for focused study. The relatively green, cheap sourcing and refinement of the elements copper, bismuth and sulfur satisfy the sourcing stream requirements to a greater degree than the commonly

implemented element tellurium, cadmium, gallium, and indium.[10] The chemistry implemented herein also satisfies to a much greater degree the drive for green manufacturing on-site.

Three goals for energy and environmental impact minimization have been met with the established chemistry to be investigated. Firstly, the precursor copper and bismuth metal salts have been adapted from the chlorides identified from the research literature to the nitrates in this author's publication[11]. Secondly, the solvent has been retained from prior literature as ethylene glycol. The production, recycling and eventual remediation of such a benign solvent has been established in industry and provides little danger beyond unlikely, massive ingestion by a human or household pets' attraction to the sweet taste and smell.[12] Finally, the use of L-cystine as both a complexing agent and sulfur donator is distinguished by the lack of reliance on aggressive reducing agents previously employed and its biologic source stream which the medical and nutritional supplement industries have thoroughly vetted.[13]

1.2 Background of Photovoltaics

Explained by Einstein in 1905, the photoelectric effect wherein short wavelength, visible light shone on a metal induces electrons to escape from that metal may be harnessed in a photovoltaic device with a configuration of appropriate semiconductors. Instead of allowing the complete liberation of the excited electrons, if the energy of a photon impacting a photovoltaic device is sufficient to excite an electron from the lower energy level across the gap to the higher one in the absorbing region, an electron-hole pair is created. A built-in asymmetry of energy levels within the device provides an

energetically favorable cascading path to drive the separation of the electron-hole pair and a potential difference is created (Fig. 1.2.1). When connected to an external circuit, the continuous cascade of electron energy is used to perform work.

Various implementations of this harnessable, photo-induced current have been developed in several generations of solar cells. The most basic and earliest widespread usage was the silicon solar cell. Each of the amorphous, polycrystalline and single crystal morphologies have been investigated and commercialized. This is a classic implementation of the p-n homojunction, where two similar materials doped to supply an abundance of hole carriers on one side and an abundance of electron carriers on the corresponding layer result in a field which effectively separates the electron-hole pair created during a photon mediated excitation event.

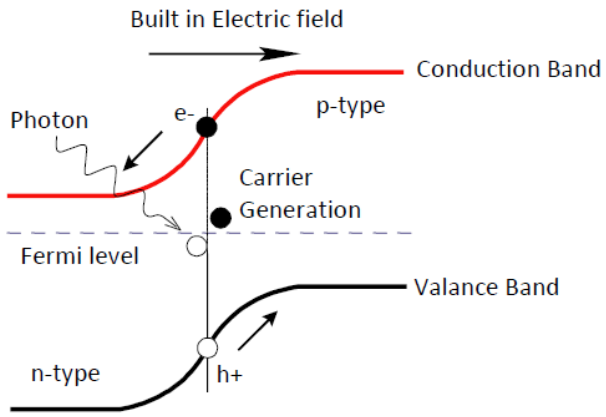

Fig. 1.2.1: Representation of photon-mediated carrier generation event within a P-N junction resulting in electron transport along the conduction band and corresponding hole transport along the valence band.

Many variations on this effect have been investigated and commercialized, as evident in an efficiency versus time plot (Fig. 1.2.2). From the mid-1970's through early 1990, research groups achieved milestones in development of single crystal, multicrystalline and amorphous silicon cells, single and dual junction gallium arsenide (GaAs) cells (with corresponding layers), and thin-film cadmium telluride (CdTe) and copper indium gallium sulfur-selenide (CIGS) technology. In approximately years 1990 and 2000 respectively, next generation dye-sensitized cells and organic cells broke into the development scene. It is critical to note that the best research cell efficiencies of the two and three junction cells carry with them significant eventual cost for production, and as such have either been limited to high capital investment projects such as NASA space-based energy needs or have required low-cost solutions for concentration methods. There does exist great potential for energy efficient implementation of multi-junction cells if industry can find efficiencies in sourcing, production and implementation of the associated balance of system required for the concentration of sunlight which predicates ultimate achieved efficiencies in stacked photovoltaics.

Below this threshold of capital investment for balance of system costs associated with the mirror and lens configurations as well as the associated infrastructure to support the apparati, it is clear that research silicon cells continue to provide greater efficiencies than those of thin-film, dye-sensitized and organic cells. While it is expected that for the near future this trend will continue, the additional design constraint for implementation of potential energy production is the manufacturing cost.

Whereas China has successfully reduced silicon solar cell (and associated panel) cost by way of purchasing power and reduced labor cost, the future holds the need and

potential for thin-film solar production to experience the same pressures. As such, candidate materials which exhibit reductions in both material sourcing and cell/module processing cost are critical not only to improving module efficiency, but to improving module production cost effectiveness, too. The investigated material here, Cu_3BiS_3, holds potential for sourcing and production cost efficiencies that may enable the U.S. thin-film solar production sector to remain a player in the global market.

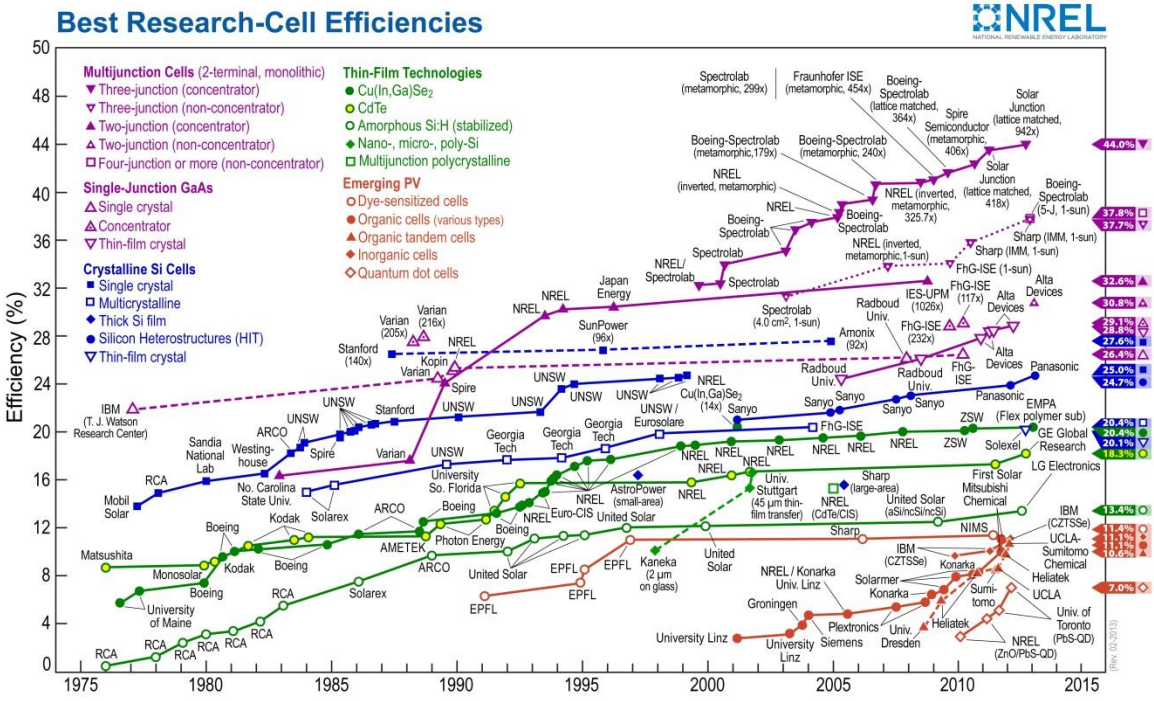

Fig. 1.2.2: NREL documentation of research level photovoltaic efficiencies delineated by fundamental cell type.[14]

1.3 Background of Thin-Film Photovoltaics

An appropriate case-study for explaining the generic thin-film photovoltaic architecture and operation in greater depth is the CdTe cell. This architecture is

reproduced to a close degree in CIGS and copper zinc tin sulfur-selenide (CZTSSe) cells as well. From the bottom (back) of the cell, a metallized back reflector provides the reflection of any unabsorbed photons back into the bulk as well as a conduction path for the completion of the voltaic circuit. This film may be sputtered aluminum, molybdenum or other metal with appropriate work function to allow the necessary conduction band cascade through the cell. In the figure shown (1.3.1), a carbon paste containing copper or other metals is illustrated, which also provides the required reflection and conductance. Moving up one stratum, the p-type absorber layer CdTe is shown with thickness ranging from 2-8 micrometers. This thickness is determined for any given absorber by balancing the absorbance (extinction) behavior against carrier lifetimes. Optimally, all incident photons will be absorbed while each excited carrier (hole and electron) is allowed to traverse a distance to surface before a recombination event.

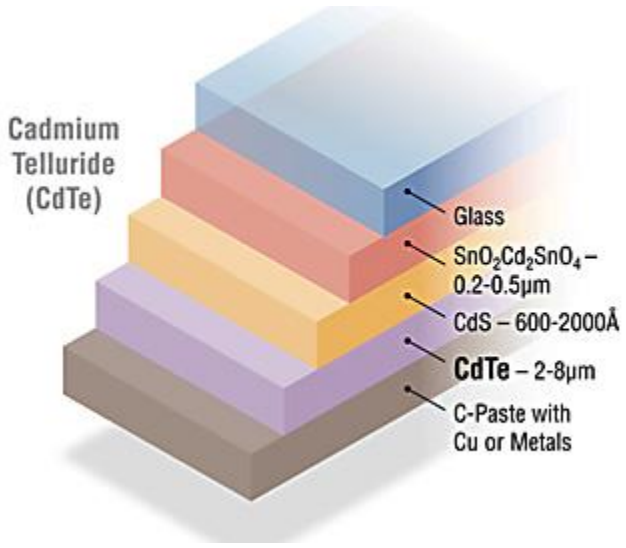

Fig. 1.3.1: Illustration of typical production CdTe photovoltaic cell strata including layer types and range of thicknesses.[15]

Cadmium sulfide (CdS) is the next layer illustrated and is the n-type layer of the p-n junction. Other thin-film stacks may employ alternative n-type layers, including varied doping of zinc oxide (ZnO). Moving upward towards incident light is the transparent conduction oxide (TCO). These are commonly fluorine or indium doped tin oxides with large bandgaps to allow transmission of incident photon energies of interest while providing a conduction pathway to complete the voltaic pathway opposite the metallized back contact. Finally, shown here only on top but also existing on the reverse side in some cells, is the glass encapsulation also transparent to photon energies of interest but essentially providing environmental protection for the interior strata. Also present in some implementations is a buffer layer of CdS in between the p-type CdTe and alternative n-type ZnO strata.[16] This buffer layer is the subject of some speculation as to its function, with the prevailing suggestion that the space-charge region necessary for electron and hole separation is broadened resulting in reduced recombination (elevated efficiency). Commercial implementation also includes anti-reflective coatings on the surface of the glass to prevent external efficiency reductions due to incident light reflection increasing as the incident angle increases with respect to normal.

There are cost advantages inherent in thin film photovoltaics that are derived from reduced material consumption and production efficiencies. The ultrathin semiconductor layers (100nm to 8μm) require less front end mining and refinement of elemental ingredients. Additionally, the thin layers and materials are amenable to high throughput production methods including ink printing, roll-to-roll production lines and scalability.[17] Concerns do exist regarding the toxicity of some device materials and associated production waste. In particular cadmium, indium and gallium which are present in

varying degrees in CdTe, CIGS and CZTS cells are problematic for eventual disposal/recycling of devices and safe containment of production refuse**.** This has recently been highlighted through an investigation of the previously unaccounted carbon footprint involved in the transport of toxic residue to safe sites which may be hundreds of miles from the point of production.[18]

A market induced cost pressure in international trade is the movement of the Chinese production sector's acquisition of legacy silicon cell production equipment. The resulting over-supply of cheaply manufactured panels has depressed profit margins for all photovoltaic manufacturing companies. Addressing U.S. based thin film product viability can improve supply of high quality product at a competitive price. While industry is experienced in optimizing current production materials and methods, it remains the goal of progressive university research to provide new materials that might eventually be even cheaper.

While prior research has established the photocurrent capability of Cu_3BiS_3 both in literature and within our own laboratories, there are several key material properties necessarily optimized for appreciable efficiencies in a completed photovoltaic cell. An absorbing semiconductor must be optimized with respect to electron and hole mobility, conduction, morphology which minimizes the predominance of grain boundary induced recombination events, layer thickness which is within the constraints of carrier mobility limitations, and layer surface roughness which simultaneously provides for efficiency improving refraction but also a reduction in short circuit currents along interfacial aberrations.

As such, the examination of a facile, low-temperature, and low toxicity chemical synthesis/precipitation route for Cu_3BiS_3 as a replacement absorber layer in a traditional thin-film photovoltaic stack is investigated here to first establish a reliable and efficient method of thin-film growth. Only once a consistent thin-film production method has been established can many of the characterization techniques providing the aforementioned electrical properties be employed. The research method herein is therefore one which incorporates both the materials science and the engineering components of the discipline.

In a similar manner to industry research and development, an initial plan to develop a novel material synthesis route (Chapt. 2) enabling the subsequent engineering of a useful process to produce it (Chapt. 4-5) was followed. During the characterization of the early synthesis work it was found in literature that the employment of the Tauc method to analyze UV/Vis spectroscopy data was employed inconsistently. To be sure of the initial synthesis success in achieving a fundamental goal (i.e. a bandgap of approximately 1.5 eV), it became necessary to investigate, validate and refine the employment of the Tauc method (Chapt. 3). The process, research and results provide a base from which further refinement of the reactor deposition may occur and an eventual employment within a thin-film photovoltaic stack may occur. The envisioned novel device is described in detail in the final portion of the Future Work section within this dissertation.

CHAPTER 2

Solvothermal Synthesis of Cu_3BiS_3 Nanocrystals

2.1 Background of Cu_3BiS_3 and Synthesis Thereof

Increasing attention is being directed toward the development of alternative and earth-abundant semiconductors for photovoltaic and other optoelectronic applications. One promising class is the I-V-VI family which includes Cu_3BiS_3. Naturally occurring in the "Wittichenite" mineral form[19], the compound is stable for a broad range of processing temperatures.[20,21] The phase diagram in Fig 2.1.1 suggests stability to 527ºC, but in actual processing groups have reported stoichiometric inconsistencies above 250-300ºC as sulfur is lost to a vaporization process without over pressurization of sulfur vapor or nitrogen. [22,23] Experimentally derived properties for Cu_3BiS_3 are presented in Table 2.1.1, with ranges provided where relevant and available.

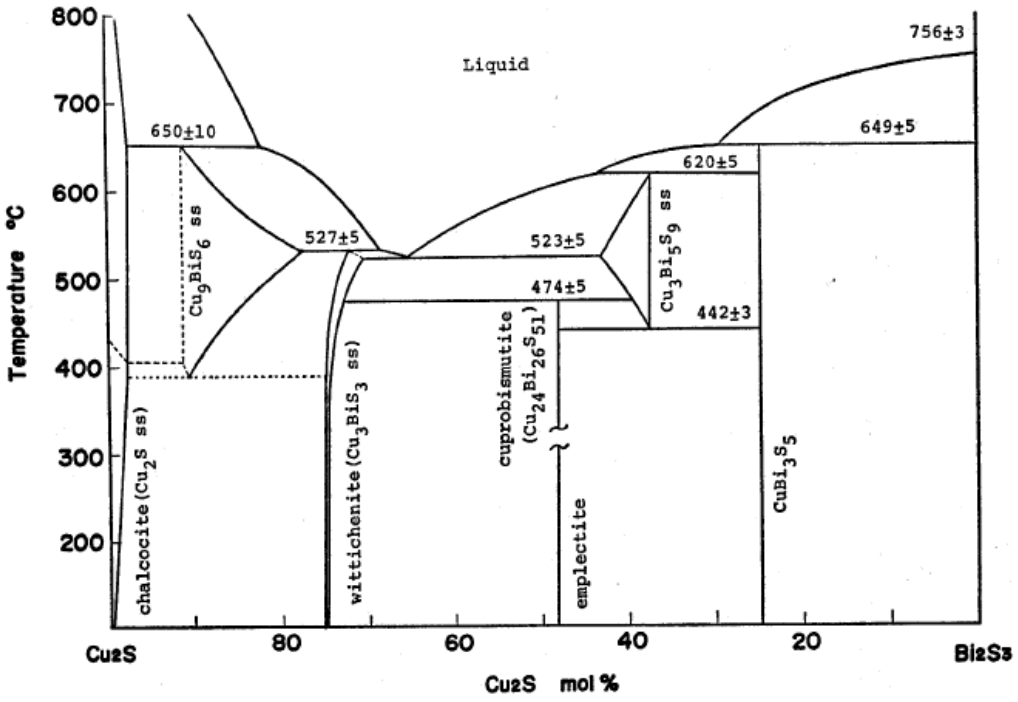

Fig. 2.1.1: Phase diagram of the Cu_2S—Bi_2S_3 system.[20]

Space Group[19]	$P2_12_12_1$
Point Symmetry[19]	C_i
Crystal Structure[19]	Orthorhombic
Lattice Dimensions[19]	a=7.723 Å b=10.395 Å c=6.716 Å
Density[24]	6.11 x 10^3 kgm^{-3}
Bandgap Type[25]	Direct
Bandgap Value[9,24–35]	1.2-1.86 eV
Absorption Coefficient[24,25,27,30,31,33,34,36]	4 x 10^4 -- 1 x 10^5 cm^{-1}
Conductivity[24,34,36]	1 x 10^{-4} -- 1 x 10^{-3} Ω^{-1} cm^{-1}
Resistivity[27,37]	3-200 Ω cm
Sheet Resistance[36,37]	3 x 10^4 -- 1 x 10^{12} $\Omega\square^{-1}$
Carrier (Hole) Concentration[25,38]	2 x 10^{16} cm^{-3}
Hall-mobility[39]	4 $cm^2V^{-1}s^{-1}$
Work Function[39]	4.37 +/- 0.04 eV
Thermo-electric Power[38]	0.73 mVK^{-1}
Dielectric Constant[25]	7.87

Table 2.1.1: Experimentally derived properties of Cu_3BiS_3.

Various techniques have been employed to synthesize Cu_3BiS_3 and other ternary sulfide films and nanostructures. Sputtering[9,23,27,28,36,37], co-evaporation[30,31,40], and solid-state reactions[24,36,41] have been successful in producing stoichiometric compounds depending on the nature of the processes. Solution based syntheses of both hydrothermal[42] and solvothermal[36,43–47] routes have been demonstrated with a range of precursors. While most rely on thermal heating to exceed the reaction threshold, microwave heating has also been demonstrated.[47]

Solution based synthesis of ternary chalcogenides also brings with it the risk of producing counterproductive binary compounds. Strong reducers are often employed to facilitate and expedite ternary syntheses, but their toxicity is a growing concern if any process is to be scaled for manufacturing. In a rising trend toward green synthesis, the employment of biological complexing agents has been successful. The use of L-cystine as a sulfur donator was demonstrated for Sb_2S_3,[43] and its use as a complexing agent for the closely-related ternary Cu_3SbS_3 system followed quickly.[46] The Cu_3BiS_3 nanoparticles produced in a similar fashion have resulted in varying morphologies, including dendrites,[41,47] rods[44] and flower (or coral) like structures.[35] There remains until now a lack of Cu_3BiS_3 synthesis employing a solvothermal system, L-cystine as a sulfur donator and a complexing agent, radiant heating and nitrate salt precursors; this new and useful method is presented here.

2.2 Overview of Synthesis

The method for synthesis of the Cu_3BiS_3 nanoparticles and the eventual film deposition relies on the complexing of metal ions (Cu^{2+}, Bi^{3+}) from dissolved nitrate salts with L-cystine in anhydrous polyethylene glycol with subsequent solvo-thermal reaction

under stirring. The use of nitrate salts in replacement of chlorides as well as utilizing L-cystine as a complexing agent and sulfur donator are combined here to yield a novel route with respect to prior literature.

Separate complexing of each pre-cursor ion is performed to prevent the binary sulfide formation of each, which would result in non-stoichiometric ternary compound formation. The reaction proceeds in a reflux column fitted, two neck flask heated with mantle at 187±3ºC for 3.5 hrs. Though rapid, homogeneous nucleation occurs upon reaching the L-cystine dissociation temperature of 156ºC, the elevated progressing temperature allows for full reaction of the reagents into Cu_3BiS_3 nanoparticles.

Copper bismuth sulfide (Cu_3BiS_3) has been prepared by a solvothermal method which relies on precursor complexing to achieve the desired ternary chalcogenide preferentially over possible binary sulfides in the system. The complexing agent L-cystine also simultaneously donates sulfur to the compound when the complexes are dissociated at a single temperature. This low temperature and the use of nitrate salts instead of the commonly employed but less environmentally friendly chloride salts provide a path toward cleaner methods, as described in greater detail below. The reaction progression has been characterized by X-ray powder diffraction (XRD) of sequential samples and shows complete reaction of reagents to form the Wittichenite phase. Spectroscopy analysis reveals confirmation of a direct bandgap at approximately 1.5 eV. Microscopy images reveal varying morphology dominated by particles with aspect ratios approaching 1:1 and including nano-rods. A low temperature Cu_3BiS_3 synthesis employing L-cystine as a sulfur source and complexing agent, nitrate salt precursors and pure ethylene glycol has thus been successfully developed.

2.3 Experimental Reagents

All chemicals in this work were used as obtained and include entirely: (i) copper(II) nitrate trihydrate, 99-100% purity, purchased from Sigma-Aldrich; (ii) bismuth(III) nitrate pentahydrate, 99.99% purity, purchased from Sigma-Aldrich; (iii) L-cystine, 99.5% purity, purchased from Sigma-Aldrich; (iv) ethylene glycol, ≥ 99% purity, purchased from Sigma Aldrich; (v) absolute ethanol, 99.99% purity, purchased from Fischer Scientific.

2.4 Experimental Preparation

In a typical procedure, 3 mmol $Cu(NO_3)_2 – 3(H_2O)$ was dissolved in 50ml ethylene glycol and 3 mmol L-cystine was added by stirring. Separately, 1 mmol $Bi(NO_3)_3 – 5(H_2O)$ was dissolved in 50ml ethylene glycol and 1 mmol L-cystine was added by stirring. The two solutions were added under stirring to a two-neck flask fitted with a reflux column to prevent solvent loss. The flask was fitted with a thermometer and heated by mantle. Upon heating to 153ºC the blue solution changed to brown/black and the synthesis continued at 187+/- 3ºC for 3.5 hours. See Figure 2.4.1 for experimental schematic. Regular aliquot sampling of the particle suspension was collected by a glass pipette. After cooling to room temperature the precipitates were washed in absolute ethanol and either dried to a powder or drop-cast in suspension onto soda-lime glass.

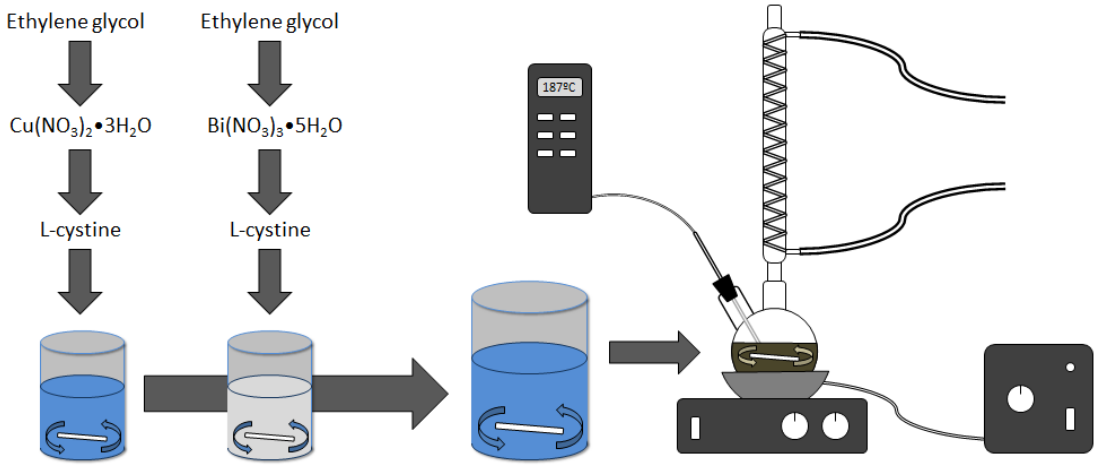

Fig. 2.4.1: Graphic representation of parallel metal ion (Cu^{2+}, Bi^{3+}) nitrate salt complexing with L-cystine in ethylene glycol and subsequent synthesis in a heated, stirred, reflux-column fitted two neck flask.

2.5 Experimental Instrumentation

The x-ray diffraction patterns for the time-sampled study were recorded using Cu-K_α radiation with a wavelength of 1.54 Å on a Siemens Kristalloflex diffractometer controlled by MDI Data Scan. The scan range was 10º to 70º with a step size of 0.02º and a 2.3 second dwell time. The absorbance spectra of a particle solution were collected on a PerkinElmer UV/Vis Lambda 850 Spectrometer. Microstructure details were obtained from uncoated powder samples with a field-emission scanning microscope (FESEM), model Zeiss Sigma.

2.6 Results and Discussion

The reaction developed here was built on earlier work of Jiasong,[46] wherein the antimony based system was complexed in a similar manner. Pure ethylene glycol (EG) is used as solvent to allow for a reaction suitable for benchtop heating. The high boiling point of the solvent allows for heating in the presence of a reflux tube to capture lost vapor, a process which would not be as effective with the lower boiling point of EG-H_2O mixtures.

Independent from each other, the dissolved copper nitrate hydrate supplied copper ions complex with the dissolved L-cystine (Eq. 2.6.1), and the dissolved bismuth nitrate hydrate supplied bismuth ions complex with the dissolved L-cystine (Eq. 2.6.2). The dimer form of the monomer L-cysteine, the L-cystine ($C_6H_{12}N_2O_4S_2$) structure (Fig. 2.6.1) is mirrored about a double sulfur bond. After combination under heating and stirring in the reflux column fitted two neck flask the complexed metal ions receive donated sulfur from the L-cystine and react to form Cu_3BiS_3 (Eq. 2.6.3).

$$Cu^{2+} + nL - \text{cystine} \rightarrow [Cu(L - \text{cystine})_n]^{2+} \quad (2.6.1)$$

$$Bi^{3+} + nL - \text{cystine} \rightarrow [Bi(L - \text{cystine})_n]^{3+} \quad (2.6.2)$$

$$[Cu(L - \text{cystine})_n]^{2+} + [Bi(L - \text{cystine})_n]^{3+} \rightarrow Cu_3BiS_3 \quad (2.6.3)$$

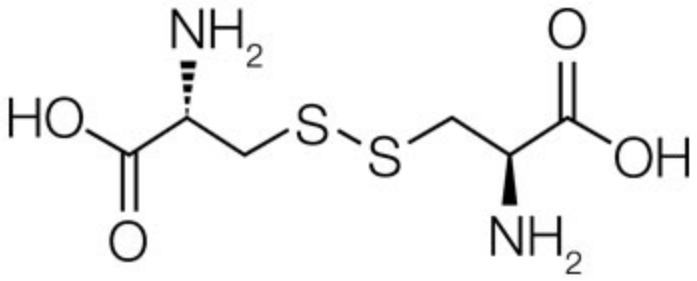

Fig. 2.6.1: Skeletal representation of the L-cystine molecule ($C_6H_{12}N_2O_4S_2$).

The reaction initiation appears at 153ºC as a quick sweeping color change from the azure blue of the copper ion containing solution through amber to a dark brown within minutes. Continued growth and purification is inferred from the analysis of XRD patterns of drop cast precipitate collected progressively during the synthesis (Fig. 2.6.2). At one hour post nucleation no evidence exists for the presence of the Wittichenite crystal, but the small particle size may inhibit diffraction sufficient for XRD detection. At 1.5 hours characteristic Cu_3BiS_3 peaks appear as well as a strong peak around 28 degree 2Θ. This intense peak which diminishes through 2.5 hours and disappears by 3.5 hours is proposed to be an H_2S intermediary,[48] which is seen in other reactions. By 3.5 hours all of the diffraction peaks can be indexed as those from the known Wittichenite crystal (Fig. 2.6.3). Continued heating and stirring of the solution to 4.0 hours results in strengthening of XRD peaks and likely indicates the growth of individual particles.

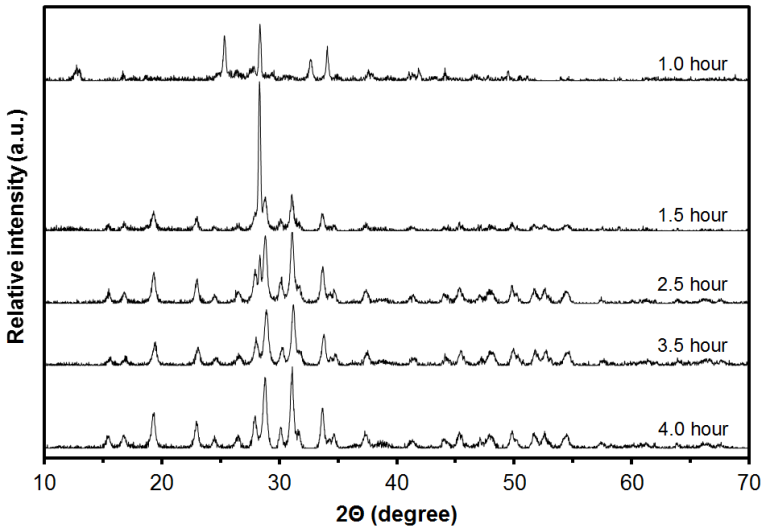

Fig. 2.6.2: XRD pattern of precipitate as synthesized at various stages during reaction.

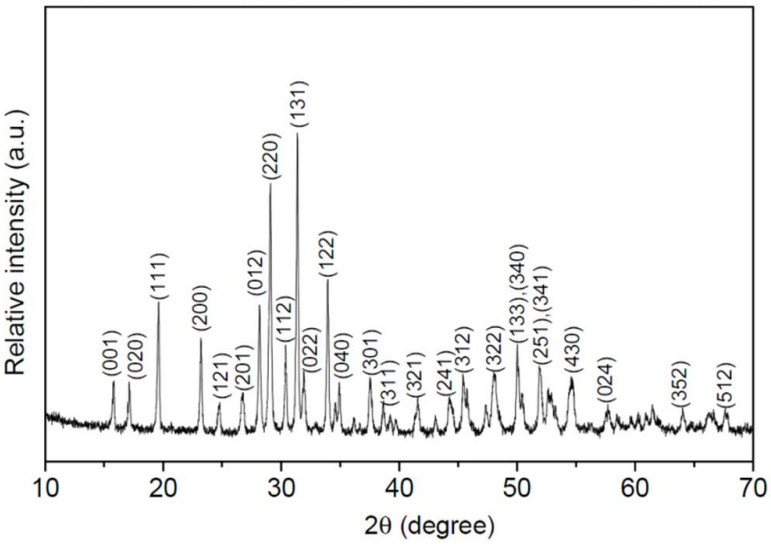

Fig. 2.6.3: XRD reference pattern for pure Cu_3BiS_3 Wittichenite crystal.

UV-Vis analysis of a particle solution in ethanol and a subsequent conversion of data into a Tauc plot (Fig. 2.6.4) allows for an estimation of the bandgap.[49] A curve fit of the linear region extended to the X intercept provides a bandgap estimated at 1.56 eV, in

good agreement with published values.[28,30,35,37] In Chapter 3, we examine the Tauc method more closely to evaluate its accuracy and better understand the tail absorption, which is often seen in published Tauc plots for many materials.

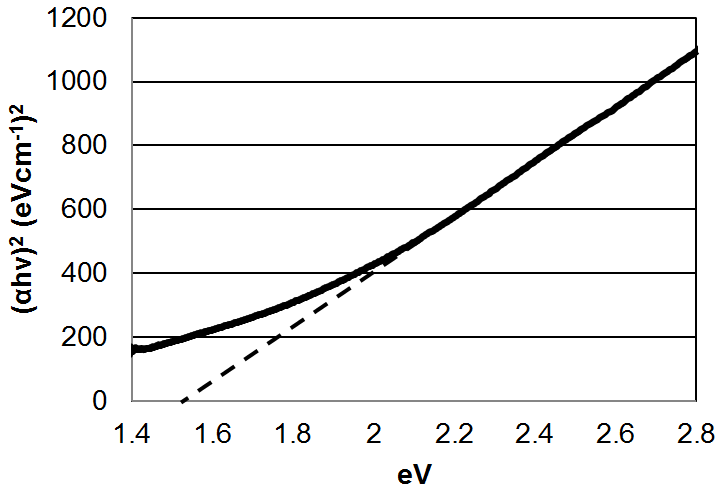

Fig. 2.6.4: Tauc Plot from UV-Vis spectrum of precipitate as synthesized four hours into reaction with estimated intercept at direct band gap of 1.5eV.

The structure of the nanoparticles is varied and includes rods and more spherical particles approaching an aspect ratio of 1:1 (Fig. 2.6.5). Regions of higher concentration for each particle type are present and this may indicate two different growth processes occurring during synthesis. The rods are on the order of 100-300 nm wide and up to two microns in length. The more spherical particles are 50-150 nanometers in diameter. As no substrate was provided for growth, there is no ordering or alignment of the rod shapes. The possible beneficial use of this precipitation in the presence of a substrate is explored in Chapters 4 and 5 where a flow-reactor is constructed and tested.

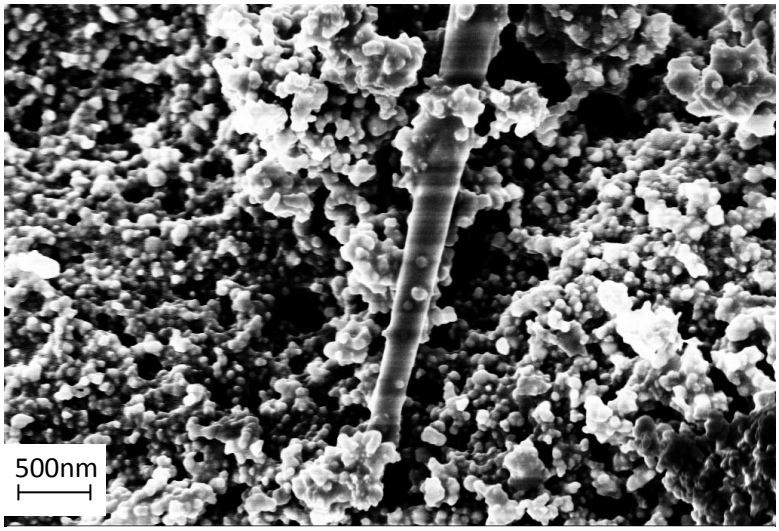

Fig. 2.6.5: SEM image (50kX) of as grown spherical particles and rods within Cu_3BiS_3 nanostructure.

The nucleation and growth of spherical particles is expected in the absence of any substrate or seeding nucleus. The presence of rod structures may best be attributed to the spontaneous formation of one or more screw dislocations within a growing sphere which result in nanowire growth.[50]

2.7 Conclusions

Cu_3BiS_3 nanoparticles have been successfully synthesized through the use of a complexing agent in a solvothermal process. Benchtop, conductive heating drives the reaction of nitrate precursors complexed with L-cystine, which also serves as the sulfur source. The transfer from previously established sealed reaction bombe syntheses to the open benchtop heating has allowed for sampling and subsequent characterization of product throughout the reaction. The improved mixing of the stirring employed has also

shortened the reaction time from 10-12 hours as previously published to the current four hour process. XRD patterns confirm a pure Wittichenite crystal structure, UV-Vis spectra confirm a bandgap of approximately 1.56 eV, and SEM image analysis reveals particles on the scale of 20-500nm.

CHAPTER 3

Analysis of Tauc Method and Application to Cu_3BiS_3

3.1 Overview

This chapter provides an in-depth analysis of the Tauc method of optical absorption edge analysis as applied to direct band gap materials, like those desired most for optical absorbers in solar cell fabrication (and as carried out on our Cu_3BiS_3 material presented in Chapter 2). The Tauc method, which uses simple multi-wavelength absorption spectroscopy, is relied upon for materials evaluation of functional photovoltaic layers. The seminal work by Tauc in 1966[51] developed a simple and useful method for assessing amorphous thin-film materials, though the method is broadly applied to crystalline thin films as well.

While extensively used to explore phase development, there remains some question about its application to polycrystalline materials as well as on the accuracy of the method. During the research, development and synthesis of Cu_3BiS_3 first in a materials science realm and following in an engineering realm through deposition reactor design, it became apparent that verification of the validity of the Tauc method for the semiconductor of interest was necessary. Further, the varied application and interpretation methods employed in the literature provided an opportunity to investigate and clarify the method for the community.

As a means of testing the Tauc method, a widely-studied composition with plentiful data was selected. We chose a composition that is expected to be very stoichiometric and does not display significant valence variances under most normal processing situations. Further, we wanted a material known to form easily from many chemical routes. These considerations led to the selection of ZnO as the basis for our standardization studies. Further background on the ZnO material, its properties and applications is given below in Section 3.2, followed by a short section (3.3) reviewing the basic Tauc analysis[51] and its normal implementation. Our review of zinc oxide (ZnO) literature was performed first seeking papers that cited Tauc's seminal work irrespective of processing route or other limitation; this resulted in over 400[*] publications. This listing was culled to remove data that was solely devoted to doped compositions (which otherwise would have allowed for wider variability in actual band-gap properties) or didn't provide graphical Tauc plots. The remaining literature[52–203] yielded a large set which included Tauc analyses[52,53,58,59,62,63,68,69,72–75,77,78,82,84,88,90–95,116,117,133,135,136,144–147,149,150,163,169–175,180–184,186–194,196,198–202] on undoped ZnO thin films prepared by various methods. These literature instances of Tauc analyses on ZnO were digitized and reanalyzed using a rigorous process, as described below in Section 3.4. Using this large population we were able to look for trends based on coating thickness, microstructure characteristics and processing technique. The results of these analyses are given in Section 3.5, along with a fuller discussion of possible sources of potential error using this

[*] While this seems like a large number of Tauc analyses, we know that there are far more ZnO analyses in the literature that have also used the Tauc method, but have not cited Tauc's work; this makes it difficult to track them down without complete reading of all ZnO papers. The population of studies used here is believed to be large enough to provide a good representation of the larger body of ZnO works – and the Tauc method more specifically.

method. This leads to the development of a simple figure of merit which can be easily applied to Tauc analyses and is shown to be correlated with better quality samples.

3.2 Introduction to Zinc Oxide (ZnO)

Zinc oxide is a versatile, functional material in industrial and research applications from structural to optical, which has been employed for nearly a century.[204–206] In more recent development it has proven valuable in humidity sensors[62] and in various other gas sensing.[207,208] Photovoltaics have been improved with the inclusion of the natural n-type semiconductor properties and the direct, high bandgap (~3.27 eV).[206,209,210] These same bandgap properties also make the material attractive for transparent conducting electrodes[211] and integration in optical wave guides and acousto-optic devices.[212] Deposition methods available for zinc oxide include metal organic vapor phase epitaxy (MOCVD), molecular beam epitaxy, thermal evaporation, hydro- or solvo- thermal growth, magnetron sputtering and pulsed laser deposition (PLD).[62] It is stable in a hexagonal wurtzite structure with lattice parameters of (c=5.205 A, a=3.249 A).[206] While every nominally stoichiometry compound must thermodynamically have point defects at some level (and therefore by definition be *non*-stoichiometric), the phase of ZnO has been experimentally studied and found to have very little deviation from the ideal 1:1 ratio. For example, the early work of Allsopp and Roberts found a slight zinc excess, but less than 50 ppm.[213] This is much more stoichiometric than many phases and thus provides a good calibration for the Tauc process, as described further below.

3.3 Background on Tauc Method

While investigating the optical and electronic properties of amorphous Germanium, Tauc et al proposed and substantiated a method for determining the bandgap of a semiconductor from a relationship of optical absorbance data plotted appropriately with respect to energy[51] (Eq. 4).

$$(\alpha h \nu)^{1/n} = A (h \nu - E_g) \qquad (4)$$

Here h is Planck's constant, ν is the photon's frequency, α is the absorption coefficient, E_g is the band gap and A is a proportionality constant. The value of the exponent denotes the nature of the sample transition, whether allowed or forbidden and whether direct or indirect:

For direct allowed transition	n=1/2
For direct forbidden transition	n=3/2
For indirect allowed transition	n=2
For indirect forbidden transition	n=3

Typically, the allowed transitions dominate the basic absorption processes, giving either n=1/2 or n=2.

The procedure for a Tauc analysis then is to acquire optical absorbance data for the sample in question that contains a range of energies from below the transition to above it. Plotting the $(\alpha h \nu)^{1/n}$ versus $(h \nu)$ is a matter of testing n=1/2 or n=2 to

evaluate the correct transition coefficient. For well investigated materials, such as zinc oxide in the case of this inquiry, it is a matter of a literature review investigation. For emerging or less understood materials, the exponential may be tested until a linear region is evident within the absorption vs. energy plot.

Figure 3.3.1 gives one example Tauc plot for ZnO where the absorption coefficient times the photon energy to the second power is plotted versus the incident energy.[78] The second power was used as zinc oxide is confirmed to have a direct allowed transition.[206] Regression of the linear region of the data resulted in an intercept along the x-axis corresponding to the bandgap of the material, here found to be 3.26 eV.

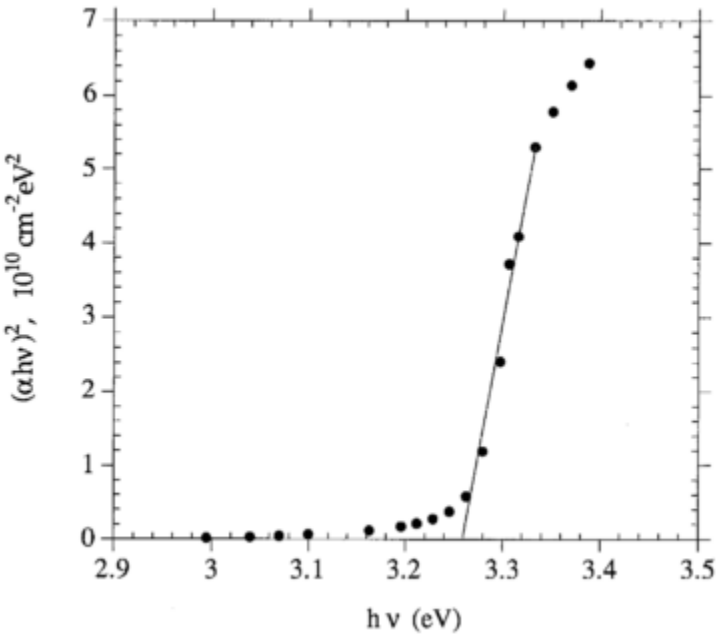

Fig. 3.3.1: Example Tauc Plot from UV-Vis spectrum of a ZnO thin film which has been overlayed with a linearization of the transition to obtain the sample bandgap (3.26 eV).[78]

It is worth noting that the selection of a linear region within typical absorption data as exemplified in Figure 3.3.1 requires the consideration of the non-linear regions at lower than and higher than bandgap energies. To select and justify a linear region for interpolation one must understand the reasons for these deviations from linear absorption behavior.

On the low end, the deviation from linearity has been investigated by Urbach[214] and in subsequent years, therefore, identified as an Urbach Tail. The slowly rising absorption common in many semiconductor UV-Vis spectra below the band edge is attributable to lattice disorder and the resulting sub-conduction band states available for excitation. These states are usually described by an exponential function, corresponding to a typical distribution of density of states, evident in the absorption spectra seen in the example (Fig. 3.3.1). On the high end, saturation of available transition states is responsible for an exponential decay of absorption in most collected spectra.

The value of the Tauc method in semiconductor research is two-fold. Toward the expansion of current materials knowledge, the analysis is vital for identifying the viability of new or adapted candidate materials in such areas as photovoltaics, transparent conducting oxides for the electronics and residential consumer products (e.g. active or passive window tinting), and burgeoning technologies such as optical transmission and amplification within processing chips for computers. The bandgap of materials implemented in such applications must be above the visible spectrum, and also tunable to each application. The second and more valuable use for Tauc analysis implementation is the interrogation of deposition and doping performed within the laboratory environment. Each deposition method, whether liquid, vapor or plasma mediated, brings with it certain

possibility for contamination. The sensitivity of the Tauc analysis, as examined here, can be a valuable metric for assessing the quality of the sample fabricated. As such, the intentional distortion (higher or lower) of the intrinsic bandgap of a material by doping or other means may quickly and accurately be evaluated for success or failure.

The extensive literature survey of zinc oxide performed here for the evaluation of the Tauc method also revealed the power of the method in just this manner. The improvement of microstructure during ZnO growth and crystallization, and the purposeful manipulation of the bandgap are evident in many papers we surveyed. Perhaps best exemplifying the usefulness of the Tauc analysis for evaluating sample microstructure, Mandal et al.[131] prepared four samples via RF sputtering; through manipulation of the deposition conditions from a minimum of 27ºC to a maximum of 300ºC, a corresponding grain size within each sample was produced in a range of 29-53nm. The simultaneous application of a Tauc analysis tied the investigation together revealing an inverse relationship between bandgap and sputtering temperature and bandgap and grain size, for their experimental conditions. The absorption edge was effectively moved from 3.24 eV at the highest processing temperature and largest grain size to 3.32 eV at the lowest processing temperature and smallest grain size. Through doping, Bandyopadhyay et al. were able to accurately quantify the effect on band gap of zinc oxide with minor (1-2%) introduction of aluminum, effectively raising the absorption edge from 3.19-3.24 eV.[58] Marotti et al. were able to employ electrochemical deposition and varying post-processing temperatures to develop samples from 3.18-3.26 eV.[132] While the specific band gap values varied between laboratories (using different

equipment and deposition techniques and fitting methods), the increases or decreases have been tied to changes in microstructure and chemistry in useful ways.

Though zinc oxide is a single material evaluated here with respect to the Tauc analysis, the value of the method in quickly assessing the relative quality of the prepared sample for any material is obvious. With distortion of the crystal structure of a semiconductor by inclusion of intended dopants as well as accidental contamination by environmental elements the adaptation of the bandgap may be used as an indicator of those effects. It was with this in mind that the Tauc method was evaluated by consistent re-calculation of bandgaps using published data to evaluate the method and to test its application to not only amorphous but also semi-crystalline and purely crystalline materials.

3.4 Model

As noted above, an extensive literature survey was undertaken to collect published Tauc analyses of un-doped ZnO that included plots of the absorbance data against the photon energy. This requirement was critical, as an assessment of the application of the Tauc method for this material, and for broader application, required the digitization of each data set within a given published paper and the consistent application of a fitting method, as described below. Through the following method over 150 individual Tauc plots were re-assessed for extracting bandgaps and compared to the originally published results.

3.4.1 Digitization of Published Tauc Plots

To ensure a representative population of zinc oxide absorption data and Tauc plot analyses, a literature survey was conducted on zinc oxide research after 1995 which included both nominally pure zinc oxide investigations as well as any investigation of zinc oxide which included undoped samples. Search results were reviewed to select those which included published Tauc analysis plots resulted in the collection of approximately 150 individually analyzed zinc oxide samples. This population contained materials made with many deposition methods and varying process conditions with each method (Table 3.4.3.1). One example of a published Tauc plot further analyzed is present in Figure 3.4.1.1, where Tüzemen, et al[166] investigated varying oxygen pressure on vacuum arc deposition of zinc oxide thin films.

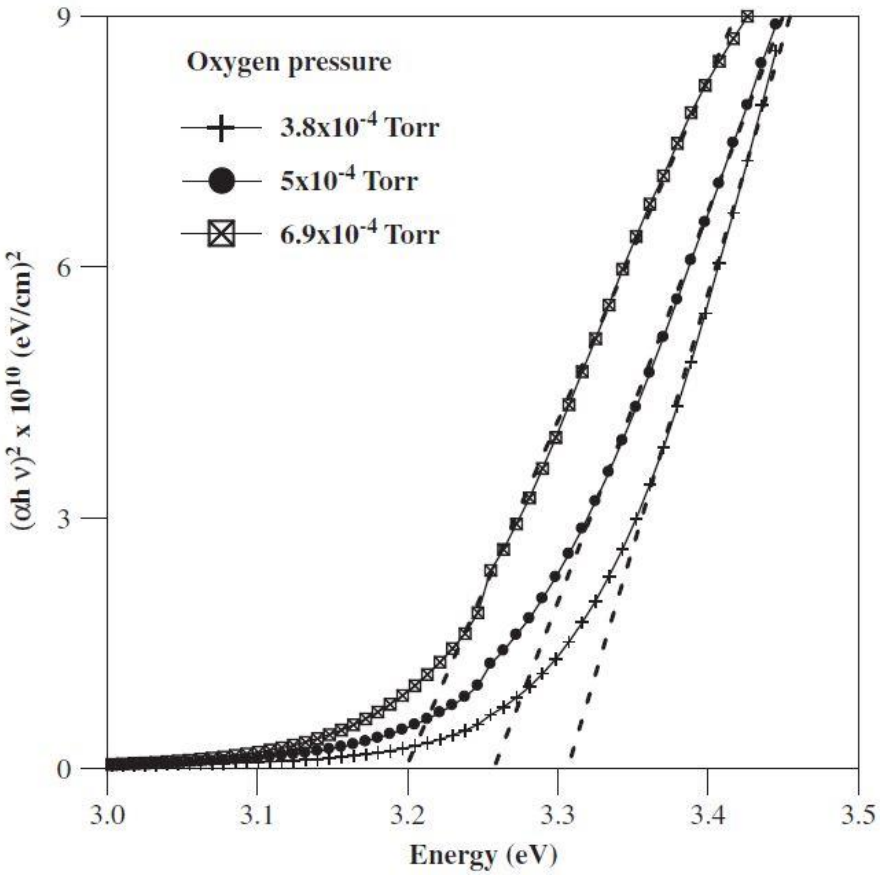

Fig. 3.4.1.1: Example Tauc Plot of absorbance data ($(\alpha\ h\ \nu)^2$) plotted versus Energy (eV) containing three sample curves typical of those digitized for evaluation.[166]

The digitization was done using "Plot Digitizer" (v. 2.6.2 - December 17, 2012 Build), written and freely distributed by Joseph A. Huwaldt and Scott Steinhorst, to acquire data from digital (PDF) copies of the journal articles in question. The population was arranged alphabetically by first author and divided among three researchers for re-digitization of the published, plotted data. Content bias was eliminated to ensure the method was properly vetted. This massive digitizing effort was conducted with the assistance of two MSE undergraduate students (Ben Davis and Shane Patel).

Each Tauc analysis plot was collected and digitized in the following manner. A screen print digital copy of the plot was collected at the highest resolution possible. The saved JPG image was imported into the digitizing software previously noted. Once imported, the process for digitization began with the assigning of origin, axes, and scale according to the published data. Then each distinct data point was logged, or for smooth curves then reasonably closely spaced data points were digitized. Each "click" logged by the software was then saved in a data file specifying X (Energy [eV]) and Y (Absorption $[(\alpha\ h\ \nu)^2]$) values (or other units, as applicable). Representative data from the digitization of one absorption curve ($3.8x10^{-4}$ Torr oxygen over-pressure) from an arc-deposited thin-film zinc oxide coating[166] is shown in Table 3.4.1.1.

Energy (eV)	Absorption $(\alpha h \nu)^2$	Energy (eV) (continued)	Absorption $(\alpha h \nu)^2$ (continued)
3.001830	0.049300	3.255540	0.649728
3.009129	0.049060	3.263760	0.731725
3.018253	0.048760	3.274721	0.846539
3.025552	0.048519	3.282946	0.977895
3.037414	0.048129	3.290262	1.142189
3.049275	0.047739	3.299404	1.322876
3.058397	0.030985	3.304897	1.503683
3.072087	0.063442	3.315871	1.750123
3.089424	0.079325	3.325934	2.013047
3.103110	0.078874	3.335089	2.325361
3.113147	0.078544	3.342419	2.621282
3.127748	0.110970	3.352492	2.982926
3.138697	0.110610	3.36257	3.393930
3.151473	0.126643	3.370828	3.854355
3.156038	0.159400	3.380914	4.347626
3.165162	0.159099	3.389179	4.873864
3.173375	0.175283	3.399272	5.432949
3.179764	0.191526	3.406633	6.041484
3.188891	0.224132	3.415817	6.633505
3.197108	0.273222	3.421318	6.896579
3.204407	0.272982	3.426834	7.307734
3.213533	0.289135	3.433258	7.669498
3.221751	0.354678	3.437852	7.981962
3.229970	0.420222	3.441531	8.278003
3.238183	0.436405	3.449776	8.606800
3.246403	0.518402	3.453459	8.935748

Table 3.4.1.1: Example of extracted absorbance data ($(\alpha h \nu)^2$) and energy (eV) from digitization of one curve of Tuzeman et al (3.8×10^{-4} Torr).[166] Data is extracted from lowest curve in Figure 3.4.1.1 above.

During the digitization process each publication was also evaluated for potentially significant processing and sample parameters. Noted for each publication and each

individual absorption data set were: bandgap (Eg) as assessed and reported by the author(s); the maximum temperature (T_{max} ^{o}C) that the sample was subjected to including any post processing steps; the sample grain size (nm); the sample thickness (nm); and the deposition/synthesis method. This would all be important for the later reported investigation of data trends within the ZnO sample population. The output of the assessment is available in Table 3.4.3.1, which include bandgap values assessed by the following methods.

3.4.2 Linear Regression Modelling of Extracted Data Sets from Digitized Tauc Plots and Assessment of Bandgap for Comparison to Published Values

Each of the digitized data sets was first replotted and visually examined to ensure no artifacts of digitization were present as unrealistic outliers not corresponding to the originally published figures. One example of these digitized plots is available in Figure 3.4.2.1, where the function $((\alpha\ h\ \nu)^2)$ is plotted versus energy (eV). Data is extracted from the lowest curve in Fig. 3.4.1.1 above.

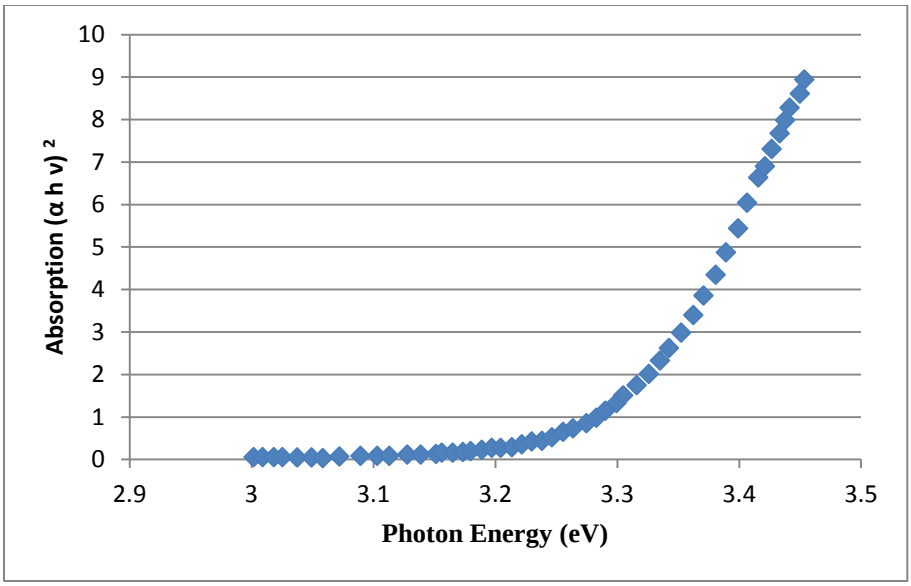

Fig. 3.4.2.1: Example Tauc Plot of re-digitized absorbance data ($(\alpha\ h\ \nu)^2$) plotted versus energy (eV) to which linear regression model was applied for assessment of bandgap (eV) at the regression x-intercept.

Though there was no particular disagreement with the Tauc fitting presented by the source authors in any case, the present work sought to develop a completely unbiased method for selecting the linear portion of a plot and determining a band-gap value. The raw digitized data were thus processed in a spreadsheet to achieve a series of linear regressions corresponding to incremental portions of each data set: a new linear regression was derived for all combinations of 11 adjacent data-points to produce a data set of extrapolated band gaps (x-intercept) per the Tauc method.[51] One example of these results is shown in Figure 3.4.2.2. The rising slope of the original absorbance data (Fig. 3.4.2.1) is seen to produce a gradually increasing assessed bandgap shown on the Y-axis as the Extrapolated Band Gap (eV) as the 11-point data series starting point progresses

along the X-axis (Energy in eV). This is completely consistent with the curvature shown in Figure 3.4.2.1, especially in the region of 3.2 to 3.4 eV.

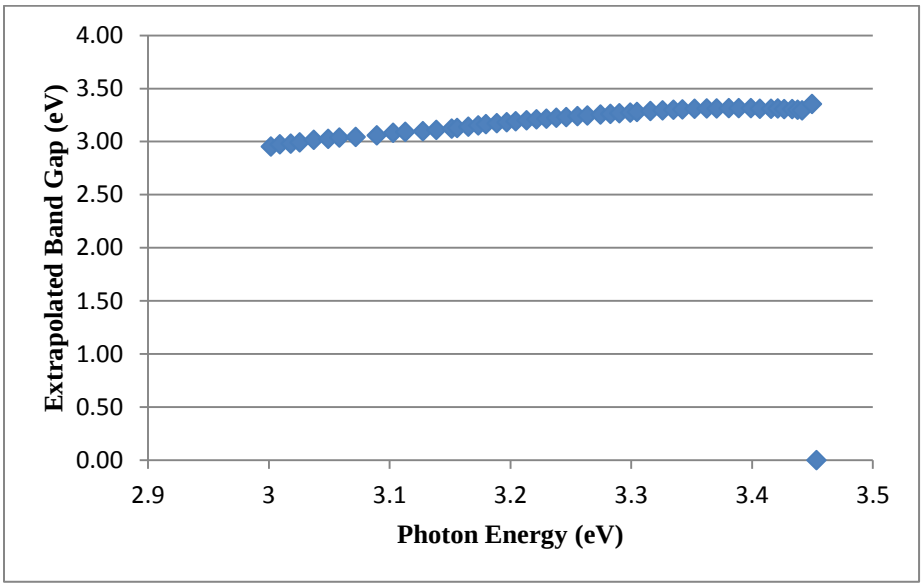

Fig. 3.4.2.2: Example extrapolated band gap (eV) plot of re-digitized absorbance data.

The assessment of the bandgap from this plot alone is not possible, as the criteria for choosing which extrapolated band gap might be best is not immediately evident from this figure. Two additional calculations were performed and the data plotted to aid in the assessment of the interpolated bandgap. The first calculation was using the R^2 value of the correlation between the fit of the consecutively and simultaneously moving 11-point series in the re-digitized data and the consecutive parabolic to find a curvature inflection. An example plot of R^2 is shown in Fig. 3.4.2.3. While the R^2 values found are all very close to unity (and therefore represent relatively good fits), we can see that the *best* values are found for data sequences starting about 3.35 to 3.40 eV (and including the 10

other adjacent data points). Referring back to Fig. 3.4.2.2 we see that the E_{gap} values found for these regressions were all 3.31 eV – which is the same E_{gap} that was found by the original authors (see line fit and extrapolation in Fig. 3.4.1.1). This is an interesting point: the energy values for photons in the linear part of the Tauc plot are significantly higher than the band-gap that is ultimately found by the extrapolation.

The poorer R^2 values found in the first two-thirds of the data set and in the highest energy values (eV) are probably resulting from different causes. At low energies the signal to noise ratio associated with collecting low absorption values results in added variability in linearity. As the UV-Vis data begins to show increasing absorption in the mid-range of data, including the often present Urbach tail[214], linearity decreases with rising curvature. At the highest energies, the absorption is so strong that it results in a negative curvature and a deviation from linearity. The region which remains highly linear, as evidenced by the near unity R^2 values of the correlation, is the appropriate region from which one can extract the bandgap per Tauc.

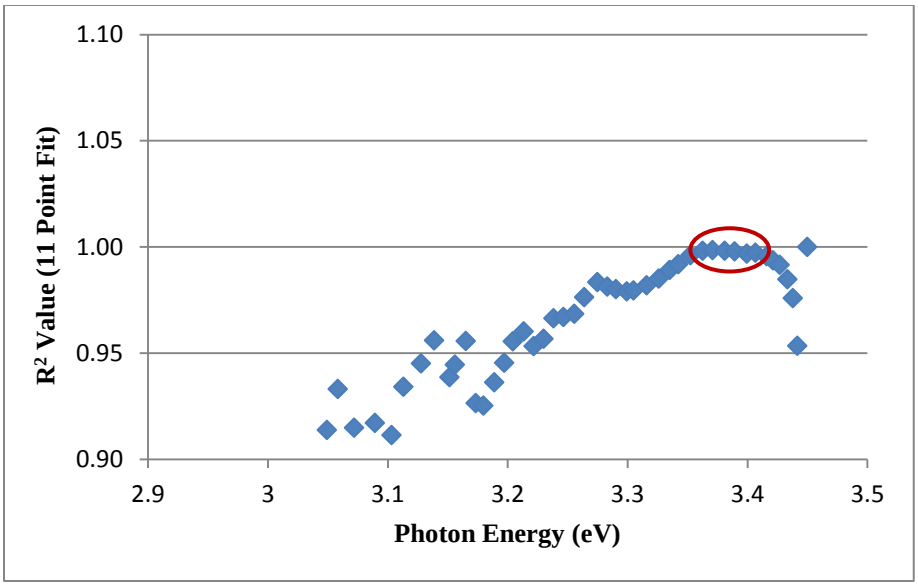

Fig. 3.4.2.3: Example R^2 value for fit of consecutive 11-point series in the re-digitized data and in the corresponding linear regression data set. Highest (*best*) values are found for data sequences starting about 3.35 to 3.40 eV (circled). E_{gap} values found for these regressions were all 3.31 eV – which is the same E_{gap} that was found by the original authors.

Critical to the consistent re-assessment of zinc oxide band gaps executed by multiple researchers from published Tauc plots was the establishment of evaluation criteria. Toward this end consistent conditions for assignment of the linear region to be used were determined and agreed upon prior to the assessment of each individual set of curves. Each original author asserted a linear region of transition corresponding to an x-intercept relating band gap per the method in their evaluation most often without description of linearity evaluation criteria. The investigation here required specific conditions be met on the extrapolated bandgap plots, the R^2 value for linear regression fit plots, and the curvature of parabolic fit plots.

The extrapolated bandgap plot data were evaluated for their maximum, corresponding to the greatest slope available to linearization. The R^2 values for fit data were observed to approach 1.0, corresponding to a good fit of a linear region of absorbance data. Finally the curvatures of parabolic fit data were evaluated for a minimization of the absolute curvature, corresponding to the most linear region of absorbance data. With assessment criteria for each of the four data sets associated with a particular original Tauc analysis, the bandgap was identified for each by examining these criteria; the full results of these analyses are given below.

3.4.3 Results of the Bandgap Reassessment and the Investigation of Data Trends within the ZnO Sample Population

Table 3.4.3.1 provides the results of the bandgap reassessment, the bandgap (Eg) as assessed and reported by the original author(s), the maximum temperature (Tmax ºC) to which each sample was subjected, including any post processing, the sample grain size (nm), the sample thickness (nm), and the deposition/synthesis method. The deposition/synthesis methods were grouped into categories thought to yield more similar phase/product materials in order to facilitate the evaluation of any correlation between processing route and eventual bandgap. For example, the “Liquid Thermal” grouping included both hydrothermal and solvothermal.

	Year	First Author	E_g (ref.)	E_g (exp.)	T_{max} (C)	Grain size (nm)	Thickness (nm)	Deposition Method
1	2010	Abraham	3.21	3.53	27	3.8	unknown	Colloid Chemical
2	2010	Abraham	3.21	3.46	27	4.7	unknown	Colloid Chemical
3	2010	Abraham	3.21	3.40	27	unknown	unknown	Colloid Chemical
4	2010	Abraham	3.21	3.39	27	6.4	unknown	Colloid Chemical
5	2010	Abraham	3.21	3.38	27	7.1	unknown	Colloid Chemical
6	2010	Abraham	3.21	3.63	27	3.2	unknown	Colloid Chemical
7	2002	Bandyopadhyay	3.19	3.20	550	90	818	Sol-gel
8	2002	Bandyopadhyay	3.22	3.21	550	40	805	Sol-gel
9	2002	Bandyopadhyay	3.24	3.24	550	40	763	Sol-gel
10	2009	Baviskar	3.28	3.30	90	unknown	40000	CBD
11	2013	Baviskar	3.28	3.24	200	20-30	2000	CBD
12	2013	Baviskar	3.82	3.77	27	62	unknown	CBD
13	2013	Baviskar	3.20	3.13	200	41	6000	Ion Layer
14	2013	Baviskar	3.22	3.17	200	40-60	24000	Ion Layer
15	2013	Baviskar	3.25	3.23	200	41	4000	Ion Layer
16	2013	Biswas	3.41	3.39	400	unknown	unknown	CVD
17	2011	Bojorge	3.29	3.29	400	175	unknown	Electrochemical
18	2008	Caglar	3.28	3.29	450	unknown	unknown	Spray Pyrolysis
19	2008	Caglar	3.29	3.29	450	unknown	unknown	Spray Pyrolysis
20	2008	Caglar	3.29	3.29	450	unknown	unknown	Spray Pyrolysis

Table 3.4.3.1: Analysis of Tauc method summary information, including: year published; first author; bandgap published (E_g (ref.)); bandgap assessed per this analysis (E_g (exp.)); maximum temperature sample was subjected to (T_{max} (C)); sample grain size (nm); sample thickness (nm); method of sample deposition.

	Year	First Author	E_g (ref.)	E_g (exp.)	T_{max} (C)	Grain size (nm)	Thickness (nm)	Deposition Method
21	2008	Caglar	3.30	3.30	450	unknown	unknown	Spray Pyrolysis
22	2012	Chand	5.57	5.95	200	63	unknown	Liquid Thermal
23	2012	Chand	5.68	5.92	200	37	unknown	Liquid Thermal
24	2012	Chand	5.79	5.91	200	23	unknown	Liquid Thermal
25	2007	Chawla	3.21	3.35	n/a	0.53	2180	Sputtering
26	2011	Chen	3.27	3.27	500	unknown	unknown	CVD
27	2006	Choi	3.36	3.34	500	unknown	300	CVD
28	2006	Choi	3.47	3.50	500	unknown	300	CVD
29	2006	Choi	3.54	3.55	500	unknown	300	CVD
30	1994	Craciun	3.26	3.26	350	unknown	300	PLD
31	2012	Dimitriev	3.22	3.25	400	<50	unknown	Mechanochemical
32	2012	Dimitriev	3.25	3.27	200	<50	unknown	Mechanochemical
33	2012	Dimitriev	3.27	3.29	400	<50	unknown	Mechanochemical
34	2012	Dimitriev	3.27	3.25	200	<50	unknown	Mechanochemical
35	2011	Faraj	3.45	3.45	unknown	unknown	100	Thermal Evaporation
36	2011	Faraj	3.42	3.47	unknown	unknown	200	Thermal Evaporation
37	2011	Faraj	3.38	3.49	unknown	unknown	300	Thermal Evaporation
38	2010	Ghodsi	3.28	3.27	400	amorphous	348	Sol-gel
39	2008	Gulino	3.30	3.30	500	5-10	300-500	Rapid Quenching
40	2010	Gurav	3.30	3.25	673	19	1690	Soft chemical

Table 3.4.3.1 $^{(cont'd)}$: Analysis of Tauc method summary information, including: year published; first author; bandgap published (E_g (ref.)); bandgap assessed per this analysis (E_g (exp.)); maximum temperature sample was subjected to (T_{max} (C)); sample grain size (nm); sample thickness (nm); method of sample deposition.

	Year	First Author	E_g (ref.)	E_g (exp.)	T_{max} (C)	Grain size (nm)	Thickness (nm)	Deposition Method
41	2010	Gurav	3.90	3.77	27	15	1690	Soft chemical
42	2012	Hammouda	3.27	3.28	27	unknown	250	Sputtering
43	2012	Hantehzadeh	3.18	3.16	n/a	16.25	68.7	Sputtering
44	2012	Hantehzadeh	3.20	3.11	n/a	12.15	unknown	Sputtering
45	2012	Hantehzadeh	3.24	3.17	n/a	9.85	80.8	Sputtering
46	2010	He	3.41	3.41	140	unknown	unknown	Liquid Thermal
47	2010	He	3.47	3.48	140	unknown	unknown	Liquid Thermal
48	2010	Ho	3.24	3.25	400	10	40	Sol-gel
49	2010	Ho	3.24	3.24	500	25	40	Sol-gel
50	2010	Ho	3.26	3.24	600	unknown	40	Sol-gel
51	2006	Hong	3.24	3.23	27	14	110	Sputtering
52	2006	Hong	3.20	3.19	27	14	110	Sputtering
53	2006	Hong	3.16	3.17	27	16	110	Sputtering
54	2006	Hong	3.14	3.16	27	15	110	Sputtering
55	2006	Hong	3.12	3.17	27	14	110	Sputtering
56	2012	Hsu	3.42	3.42	27	16.5	86.6	Sputtering
57	2012	Hsu	3.36	3.36	27	17.5	121.1	Sputtering
58	2012	Hsu	3.32	3.33	27	16.9	115.6	Sputtering
59	2012	Kumar	3.21	3.25	200	28	unknown	Liquid Thermal
60	2012	Kumar	3.24	3.25	150	23	unknown	Liquid Thermal

Table 3.4.3.1 (cont'd): Analysis of Tauc method summary information, including: year published; first author; bandgap published (E_g (ref.)); bandgap assessed per this analysis (E_g (exp.)); maximum temperature sample was subjected to (T_{max} (C)); sample grain size (nm); sample thickness (nm); method of sample deposition.

	Year	First Author	E_g (ref.)	E_g (exp.)	T_{max} (C)	Grain size (nm)	Thickness (nm)	Deposition Method
61	2012	Kumar	3.29	3.31	100	15	unknown	Liquid Thermal
62	2012	Kumar	3.32	3.34	50	12	unknown	Liquid Thermal
63	2004	Li	3.24	3.40	750-900	unknown	7-10	PVD
64	2004	Li	3.45	3.68	750-900	unknown	7-10	PVD
65	2004	Li	3.52	3.84	750-900	unknown	7-10	PVD
66	2008	Liu	3.25	3.28	unknown	10	250	Unknown
67	2008	Liu	3.25	3.25	unknown	5	100	Unknown
68	2008	Liu	3.26	3.26	unknown	3	50	Unknown
69	2009	Lu	3.02	3.17	90	unknown	unknown	Electrochemical
70	2009	Lu	3.19	3.26	70	unknown	unknown	Electrochemical
71	2010	Ma	3.36	3.33	27	24	344	PLD
72	2010	Ma	3.38	3.34	27	22	285	PLD
73	2010	Ma	3.39	3.36	27	32	277	PLD
74	2013	Malek	3.27	3.27	500	39	270	Sol-gel
75	2013	Malek	3.27	3.28	500	30	210	Sol-gel
76	2013	Malek	3.27	3.28	500	24	180	Sol-gel
77	2013	Malek	3.27	3.26	500	35	250	Sol-gel
78	2013	Malek	3.27	3.26	500	32	240	Sol-gel
79	2008	Mandal	3.24	3.25	300	53	145	Sputtering
80	2008	Mandal	3.28	3.28	200	48	115	Sputtering

Table 3.4.3.1 $^{(cont'd)}$: Analysis of Tauc method summary information, including: year published; first author; bandgap published (E_g (ref.)); bandgap assessed per this analysis (E_g (exp.)); maximum temperature sample was subjected to (T_{max} (C)); sample grain size (nm); sample thickness (nm); method of sample deposition.

	Year	First Author	E_g (ref.)	E_g (exp.)	T_{max} (C)	Grain size (nm)	Thickness (nm)	Deposition Method
81	2008	Mandal	3.30	3.31	100	36	112	Sputtering
82	2008	Mandal	3.32	3.32	27	29	110	Sputtering
83	2007	Marotti	3.18	3.18	89	unknown	unknown	Electrochemical
84	2007	Marotti	3.21	3.22	77.5	unknown	unknown	Electrochemical
85	2007	Marotti	3.26	3.25	62	unknown	unknown	Electrochemical
86	2000	Millon	3.28	3.28	500	unknown	150	PLD
87	2012	Mir	3.17	2.98	450	2000-3500	unknown	Inorganic Precursors
88	2010	Mishra	3.14	3.14	n/a	single crystal	5000000	Purchased
89	2005	Mohamed	3.16	3.16	300	amorphous	100	E-beam
90	2005	Mohamed	2.41	2.38	250	amorphous	100	E-beam
91	2012	Moore	3.10	3.13	600	unknown	200	Sputtering - Oxidized
92	2012	Moore	3.25	3.26	300	unknown	200	Sputtering - Oxidized
93	2010	Mouet	3.17	3.17	450	15	85	Electrochemical
94	2013	Nagaraja	2.83	2.70	900	35	553	Sputtering
95	2013	Nagaraja	3.37	3.4	28	29	553	Sputtering
96	2012	Nehru	3.19	3.18	n/a	10	unknown	Liquid Thermal
97	2012	Ozutok	3.24	3.23	375	42.2	247	Spray Pyrolysis
98	2012	Ozutok	3.26	3.25	200	37.1	331	Spray Pyrolysis
99	2012	Ozutok	3.27	3.27	300	14.8	340	Spray Pyrolysis
100	2012	Ozutok	3.25	3.23	400	36.8	300	Spray Pyrolysis

Table 3.4.3.1 $^{(cont'd)}$: Analysis of Tauc method summary information, including: year published; first author; bandgap published (E_g (ref.)); bandgap assessed per this analysis (E_g (exp.)); maximum temperature sample was subjected to (T_{max} (C)); sample grain size (nm); sample thickness (nm); method of sample deposition.

	Year	First Author	E_g (ref.)	E_g (exp.)	T_{max} (C)	Grain size (nm)	Thickness (nm)	Deposition Method
101	2012	Panda	3.11	3.14	100	unknown	500	Thermal Evaporation
102	2012	Panda	3.20	3.23	200	unknown	500	Thermal Evaporation
103	2012	Panda	3.24	3.22	300	300	500	Thermal Evaporation
104	2012	Panda	3.24	3.26	400	570	500	Thermal Evaporation
105	2012	Pang	3.07	3.05	120	14.4	1590	Sputtering
106	2012	Pang	3.11	3.06	120	14.9	2740	Sputtering
107	2012	Pang	3.16	3.14	120	29.9	3370	Sputtering
108	2012	Pang	3.17	3.15	120	25.2	3590	Sputtering
109	2012	Pang	3.19	3.18	120	21.8	1560	Sputtering
110	2007	Ramirez	3.41	3.41	80	unknown	1300	Electrochemical
111	2009	Raoufi	3.26	3.27	300	14	500	Sol-gel
112	2009	Raoufi	3.27	3.27	400	19	500	Sol-gel
113	2009	Raoufi	3.28	3.27	500	28	500	Sol-gel
114	2011	Rusu	3.17	3.16	327	26.23	900	Thermal Oxidation
115	2011	Rusu	3.19	3.16	327	30.93	780	Thermal Oxidation
116	2012	Sali	3.28	3.28	480	15	90	Spray Pyrolysis
117	2009	Sharma	3.56	3.37	50	40	unknown	Coprecipitation
118	2009	Sharma	3.82	3.65	50	15	unknown	Coprecipitation
119	2009	Sharma	4.07	4.11	50	3	unknown	Coprecipitation
120	2007	Shinde	3.12	3.02	450	400	unknown	CBD

Table 3.4.3.1 $^{(cont'd)}$: Analysis of Tauc method summary information, including: year published; first author; bandgap published (E_g (ref.)); bandgap assessed per this analysis (E_g (exp.)); maximum temperature sample was subjected to (T_{max} (C)); sample grain size (nm); sample thickness (nm); method of sample deposition.

	Year	First Author	E_g (ref.)	E_g (exp.)	T_{max} (C)	Grain size (nm)	Thickness (nm)	Deposition Method
121	2007	Shinde	3.28	3.27	450	unknown	unknown	CBD
122	2008	Singh	3.43	3.55	1000	35.7	unknown	CVD
123	2008	Singh	3.43	3.53	700	21.8	unknown	CVD
124	2007	Singh	3.17	3.21	200	20.8	unknown	Spray Pyrolysis
125	2007	Singh	3.18	3.2	300	21.3	unknown	Spray Pyrolysis
126	2007	Singh	3.20	3.24	350	24.2	unknown	Spray Pyrolysis
127	2007	Singh	3.25	3.35	400	24.9	unknown	Spray Pyrolysis
128	2007	Singh	3.43	3.64	n/a	unknown	unknown	Spray Pyrolysis
129	2010	Smirnov	3.19	3.17	500	unknown	468	Spin Coating
130	2010	Smirnov	3.21	3.18	500	unknown	606	Spin Coating
131	2005	Tan	3.30	3.29	500	unknown	550	CVD
132	2005	Tan	3.35	3.36	450	unknown	420	CVD
133	2005	Tan	3.40	3.43	350	unknown	280	CVD
134	2005	Tan	3.40	3.43	400	unknown	330	CVD
135	2005	Tan	3.41	3.39	300	unknown	350	CVD
136	2005	Tan	3.44	3.52	250	unknown	260	CVD
137	2005	Tan	3.45	3.47	200	unknown	130	CVD
138	2011	Tansanken	3.25	3.23	150	unknown	100	ALD
139	2012	Tari	3.29	3.29	600	16.5	80	Sol-gel
140	2012	Tari	3.30	3.31	600	15	70	Sol-gel

Table 3.4.3.1 $^{(cont'd)}$: Analysis of Tauc method summary information, including: year published; first author; bandgap published (E_g (ref.)); bandgap assessed per this analysis (E_g (exp.)); maximum temperature sample was subjected to (T_{max} (C)); sample grain size (nm); sample thickness (nm); method of sample deposition.

	Year	First Author	E_g (ref.)	E_g (exp.)	T_{max} (C)	Grain size (nm)	Thickness (nm)	Deposition Method
141	2010	Tricot	3.28	3.28	700	44	200	E-beam
142	2010	Tsay	3.22	3.22	500	13.9	170	Sol-gel
143	2010	Tsay	3.26	3.27	500	8.9	180	Sol-gel
144	2010	Tsay	3.26	3.26	500	11.5	180	Sol-gel
145	2010	Tsay	3.27	3.27	500	11.6	185	Sol-gel
146	2007	Tuzemen	3.20	3.21	n/a	22.6	350	Sputtering
147	2007	Tuzemen	3.26	3.26	n/a	22.5	350	Sputtering
148	2007	Tuzemen	3.31	3.31	n/a	16.9	350	Sputtering
149	2009	Tuzemen	3.19	3.18	unknown	22.53	427	Vacuum Arc
150	2009	Tuzemen	3.20	3.17	unknown	22.52	227	Vacuum Arc
151	2009	Tuzemen	3.21	3.19	unknown	14.97	139	Vacuum Arc
152	2008	Wang	3.27	3.28	unknown	unknown	780	Vacuum Arc
153	2011	Xia	3.02	3.03	75	single crystal	unknown	Electrochemical
154	2011	Xia	3.05	3.06	75	single crystal	unknown	Electrochemical
155	2011	Yang	3.18	3.21	300	13.4	unknown	Precipitation
156	2008	Yang	3.25	3.24	600	unknown	unknown	PLD
157	2010	Yang	3.34	3.35	700	34.36	154.2	Sol-gel

Table 3.4.3.1 (cont'd): Analysis of Tauc method summary information, including: year published; first author; bandgap published (E_g (ref.)); bandgap assessed per this analysis (E_g (exp.)); maximum temperature sample was subjected to (T_{max} (C)); sample grain size (nm); sample thickness (nm); method of sample deposition.

3.4.3.1 Bandgap Reassessment – Author vs. Results

The method of bandgap assessment from re-digitized plots was found to be remarkably accurate. It is recognized that the above table brings together an extremely large number of measurements of (ideally) the same ZnO material in thin film form. As a measure of the overall accuracy of the Tauc method of bandgap determination it is useful to evaluate the distribution of E_g values found. Figure 3.4.3.1.1 displays the cumulative probability distribution of reported bandgap values of zinc oxide based on Tauc analysis. The mean value was found to be 3.266 with a standard deviation of 0.078 eV. The median of the data was 3.26. All of these are in good agreement with published single crystal values for zinc oxide.[136] Still, the distribution shape is not a clean sigmoidal shape that would be associated with a single Gaussian population, but rather exhibits some higher frequencies for E_g values above and below the median, which is discussed further in a later section.

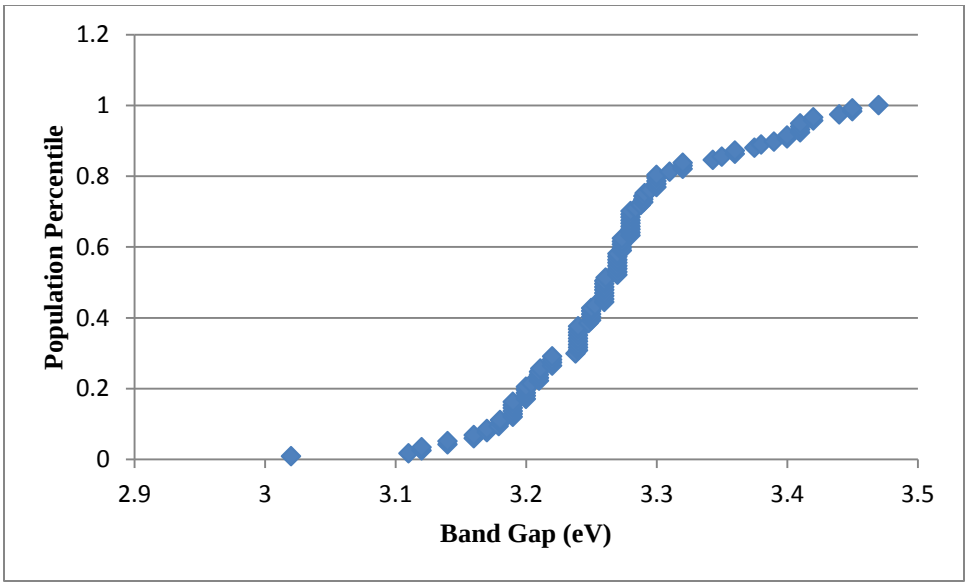

Fig. 3.4.3.1.1: Cumulative probability distribution of reported bandgap of zinc oxide based on Tauc analyses from the literature.

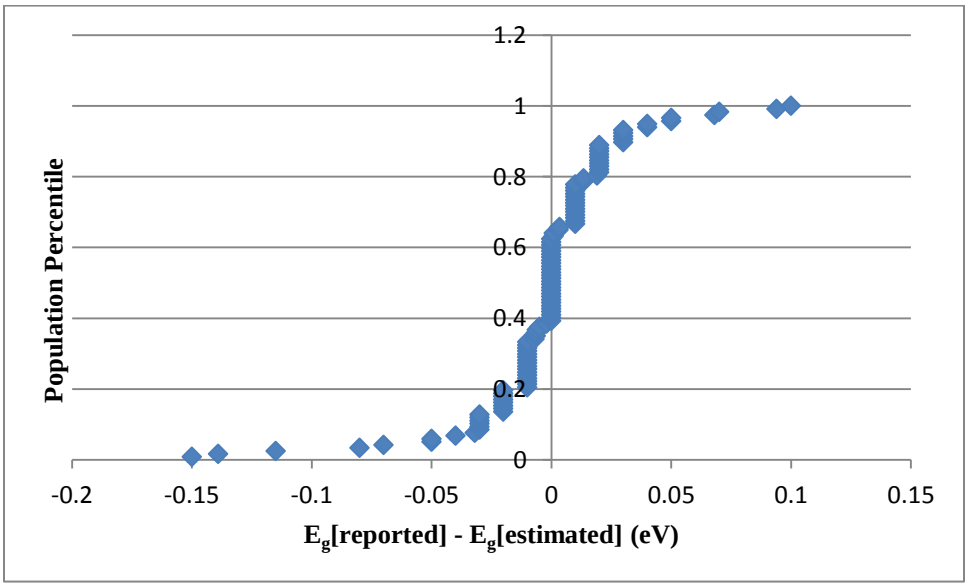

Fig. 3.4.3.1.2: Comparison of bandgap as reported by orginal author(s) (E_g [reported]) to the assessed bandgap (E_g [estimated]), where the difference between the two is plotted with respect to the cumulative probability distribution for the population.

Based on this population of E_g values from the literature, it is important to know how precise the digitization process is for reassessing the bandgap from graphical data. Figure 3.4.3.1.2 displays the cumulative probability distribution of the difference between the bandgap reported by the orginal author(s) (E_g [reported]) to the assessed bandgap (E_g [estimated]), where the difference between the two is plotted with respect to the cumulative probability within the population. The difference data follow a distribution much more tightly grouped around zero difference between the two populations, with tails extended on the low and high end. The central 60% of the studies have an agreement of +/- 0.01 eV when comparing the reported E_g. While there may be many sources of error (see discussion below), the tight distribution shown here substantiates the simple Tauc method and should also be considered as the precision of the method when performed on individual datasets.

That the variability of the difference within one standard deviation is 0.01 eV establishes two principles. First, the Tauc analysis itself is shown to accurately assess the bandgap of poly-crystalline semiconductors in addition to the originally defined amorphous semiconductor candidate class. Second, the methods outlined here are a consistent reproduction of the previous Tauc analyses and may serve as a standardization of the analysis method.

3.4.3.2 Analysis of Trends within ZnO Population

With the robustness of the original Tauc analyses and the consistent application of an analysis rubric demonstrated, the population of zinc oxide bandgap studies was investigated for trends regarding various processing variables, including maximum temperature to which the sample was subjected (T_{max}), sample grain size, sample thickness, and the deposition/synthesis method. Figures 3.4.3.2.1 – 3.4.3.2.3 show these regressions and associated fits.

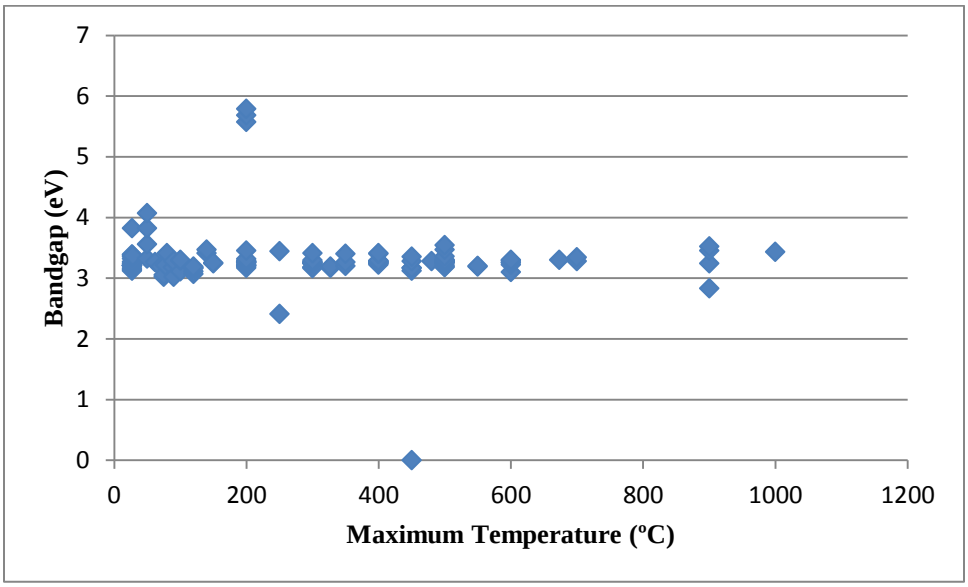

Fig. 3.4.3.2.1: Variability of bandgap of zinc oxide with respect to maximum temperature to which sample was subjected (ºC), including post-processing.

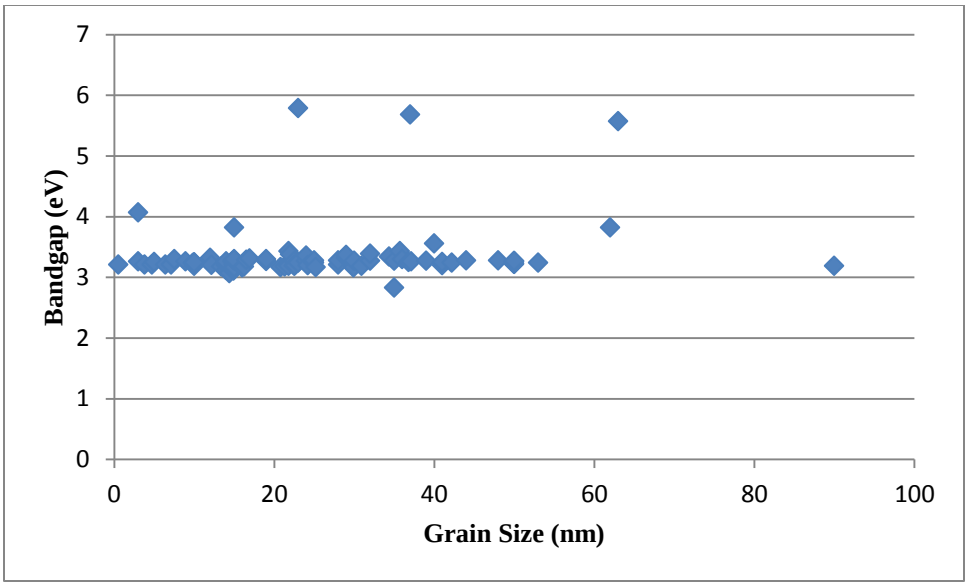

Fig. 3.4.3.2.2: Variability of bandgap of zinc oxide with respect to grain size (nm) of the sample.

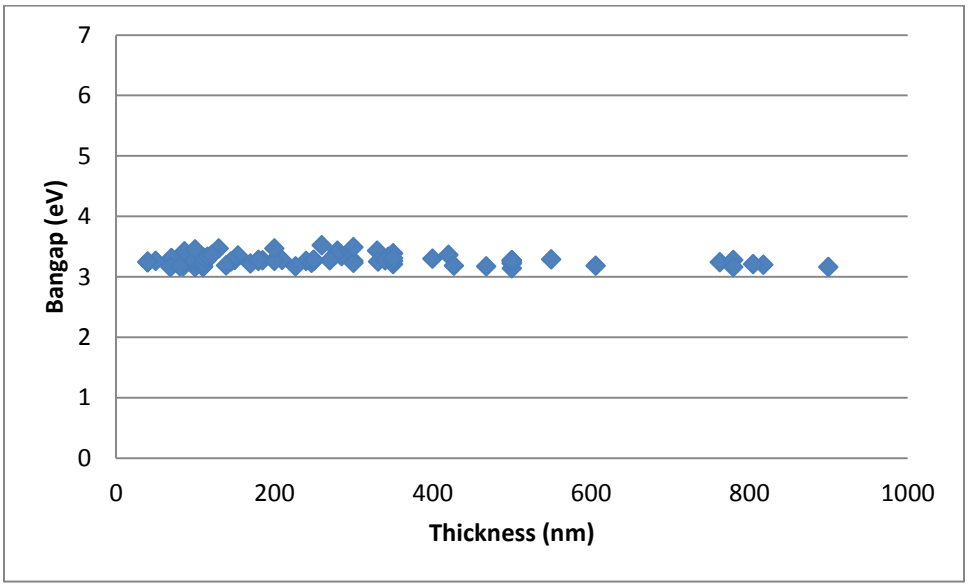

Fig. 3.4.3.2.3: Variability of bandgap of zinc oxide with respect to thickness (nm) of the sample.

While there are often reports in the literature of quantum confinement effects that might push band gap values up as grain size is reduced, the large population analysis assessed here does not support that conclusion. The resulting lack of correlation with any of the factors investigated reflects the consistently accurate 1:1 stoichiometry of synthesized zinc oxide, and further supports the choice of it as a standard material with in which to evaluate the Tauc analysis method.

3.5 Discussion

As noted above, the Tauc method is substantiated as a method for determining the band gap of a thin film material and found to have an accuracy of 0.078eV or better and a precision of 0.01eV or better. However, as shown in Fig. 3.4.3.1.1 the distribution of E_g values in the large population of data was not well represented by a simple Gaussian distribution. Rather, there appears to be secondary, smaller subpopulations with somewhat smaller and larger E_g values, respectively, that increased the breadth of the overall distribution.

The variability in overall population and even within subpopulations may derive from random composition fluctuations in the sample. While many of the referenced works rely on vacuum environments, even ppm contaminants may contribute to absorption levels outside of the targeted ZnO bandgap in each particular assessment. Outside of a vacuum environment, many of the remaining solution synthesis methods inherently are subject to the threat of environmental contamination. Supposing pure zinc oxide elemental presence, one must also consider possible phase contaminants. While the 1:1 ZnO stoichiometry is remarkably the predominant stable phase, the myriad of

processing conditions employed within the literature surveyed provide for other phases and stoichiometries. Most basically, the thickness of a thin-film is paramount to accurate calculation of absorption, and the determination of such is subject to error. Beyond the sample production within a laboratory environment, the characterization of absorption spectra may introduce variation. The calibration and offset of any light absorption/reflection measurement device is paramount to accurate measurements across a range of photon energies which may be well beyond the onset and decay of absorption for a given sample but which may be present in the Tauc analysis of any given absorption plot.

All of these experimental issues may cause changes in the shape of the Tauc plots and perhaps lead to the determination of inaccurate band-gap values. Additionally, even in the best case the method requires extrapolating from a linear region above the bandgap to find the intercept with the photon-energy axis. These inherent influences led to a further analysis of the Tauc plot shapes. In particular, a "figure of merit" is introduced that quantitatively relates to the tailing of the absorption data toward lower energy values, as discussed in the following chapter.

3.5.1 Figure of Merit Proposed

The presence of Urbach tails within absorbance spectra, owing to available states above the valence and below the conduction bands, are usually indicative of crystal disorder, randomness, or defectiveness. While the Tauc analysis utilizes only the linear region of absorption data for the extrapolation of a semiconductor bandgap, the superposition of values from the tail states can make that extrapolation less accurate. To

quantify and provide a figure of merit, a test using a ratio of the Tauc absorption value ($(\alpha\ h\ \nu)^2$) at the extrapolated bandgap energy to the absorption value ($(\alpha\ h\ \nu)^2$) evaluated at a somewhat higher energy value is performed – here arbitrarily selected to be higher by two percentage points. For future reference, this ratio is identified as the "Tauc Ratio".

$$[\ (ahv)^2 \text{ at } E_g\ ] / [\ (ahv)^2 \text{ at } E_g+2\%\ ] = \text{Tauc Ratio}$$

Ideally, the Tauc Ratio should be less than unity and samples having fewer mid-gap states or smaller Urbach tails should have especially smaller values. Because the absorption curves had been digitized before then it was a simple matter to calculate this ratio for all samples in this population. The calculation results, shown in Table 3.5.1.1, reflect a representative sub-population of the original literature survey dataset chosen to encompass the full range of bandgaps (E_g (ref.)) as assessed by the original author(s). The Tauc Ratio range varies from 0.099 to 0.916, nearly encompassing the full zero to unity range possible for the figure of merit.

	Year	First Author	E_g (ref.)	Tauc Ratio
1	2007	Shinde	3.02	0.524
2	2012	Hantehzadeh	3.11	0.916
3	2013	Baviskar	3.13	0.790
4	2010	Mishra	3.14	0.187
5	2012	Panda	3.14	0.425
6	2007	Shinde	3.14	0.674
7	2005	Mohamed	3.16	0.453
8	2011	Rusu	3.16	0.579
9	2011	Rusu	3.16	0.651
10	2006	Hong	3.16	0.739
11	2012	Hantehzadeh	3.16	0.796
12	2009	Tuzemen	3.17	0.236
13	2010	Smirnov	3.17	0.365
14	2013	Baviskar	3.17	0.595
15	2009	Lu	3.17	0.642
16	2010	Mouet	3.17	0.664
17	2006	Hong	3.17	0.683
18	2006	Hong	3.17	0.782
19	2012	Hantehzadeh	3.17	0.813
20	2009	Tuzemen	3.18	0.308
21	2010	Smirnov	3.18	0.371
22	2012	Nehru	3.18	0.472
23	2009	Tuzemen	3.19	0.389
24	2006	Hong	3.19	0.582
25	2002	Bandyopadhyay	3.20	0.163

Table 3.5.1.1: Calculated Tauc Ratios for a representative sample of band gap analyses, where author(s) reported bandgap spans the range of the population and Tauc Ratios range from near zero to near unity.

	Year	First Author	E_g (ref.)	Tauc Ratio
26	2008	Yang	3.21	0.147
27	2007	Tuzemen	3.21	0.352
28	2002	Bandyopadhyay	3.21	0.384
29	2007	Marotti	3.22	0.157
30	2010	Tsay	3.22	0.252
31	2012	Panda	3.22	0.700
32	2011	Tansanken	3.23	0.272
33	2012	Ozutok	3.23	0.274
34	2012	Ozutok	3.23	0.313
35	2013	Baviskar	3.23	0.377
36	2006	Hong	3.23	0.526
37	2012	Panda	3.23	0.572
38	2002	Bandyopadhyay	3.24	0.321
39	2010	Ho	3.24	0.420
40	2010	Ho	3.24	0.427
41	2010	Yang	3.24	0.449
42	2013	Baviskar	3.24	0.536
43	2012	Ozutok	3.25	0.164
44	2007	Marotti	3.25	0.196
45	2012	Kumar	3.25	0.300
46	2010	Ho	3.25	0.315
47	2008	Mandal	3.25	0.322
48	2008	Liu	3.25	0.377
49	2012	Dimitriev	3.25	0.456
50	2010	Gurav	3.25	0.574

Table 3.5.1.1 $^{(Cont'd)}$: Calculated Tauc Ratios for a representative sample of band gap analyses, where author(s) reported bandgap spans the range of the population and Tauc Ratios range from near zero to near unity.

	Year	First Author	E_g (ref.)	Tauc Ratio
51	2012	Dimitriev	3.25	0.634
52	2012	Kumar	3.25	0.650
53	1994	Craciun	3.26	0.124
54	2013	Malek	3.26	0.220
55	2010	Tsay	3.26	0.234
56	2008	Liu	3.26	0.268
57	2013	Malek	3.26	0.333
58	2007	Tuzemen	3.26	0.414
59	2012	Panda	3.26	0.640
60	2009	Lu	3.26	0.886
61	2009	Raoufi	3.27	0.169
62	2009	Raoufi	3.27	0.179
63	2013	Malek	3.27	0.188
64	2012	Ozutok	3.27	0.192
65	2009	Raoufi	3.27	0.224
66	2010	Tsay	3.27	0.253
67	2011	Chen	3.27	0.317
68	2010	Ghodsi	3.27	0.366
69	2010	Tsay	3.27	0.376
70	2012	Dimitriev	3.27	0.469
71	2007	Shinde	3.27	0.838
72	2012	Sali	3.28	0.111
73	2013	Malek	3.28	0.160
74	2013	Malek	3.28	0.166
75	2008	Wang	3.28	0.234

Table 3.5.1.1 (Cont'd): Calculated Tauc Ratios for a representative sample of band gap analyses, where author(s) reported bandgap spans the range of the population and Tauc Ratios range from near zero to near unity.

	Year	First Author	E_g (ref.)	Tauc Ratio
76	2012	Hammouda	3.28	0.252
77	2008	Liu	3.28	0.265
78	2008	Mandal	3.28	0.329
79	2000	Millon	3.28	0.347
80	2010	Tricot	3.28	0.600
81	2008	Caglar	3.29	0.154
82	2012	Tari	3.29	0.155
83	2008	Caglar	3.29	0.161
84	2008	Caglar	3.29	0.191
85	2011	Bojorge	3.29	0.268
86	2005	Tan	3.29	0.321
87	2012	Dimitriev	3.29	0.466
88	2008	Gulino	3.30	0.099
89	2009	Baviskar	3.30	0.433
90	2008	Mandal	3.31	0.291
91	2012	Tari	3.31	0.305
92	2007	Tuzemen	3.31	0.393
93	2012	Kumar	3.31	0.419
94	2008	Mandal	3.32	0.357
95	2010	Ma	3.33	0.285
96	2012	Hsu	3.33	0.470
97	2010	Ma	3.34	0.333
98	2012	Kumar	3.34	0.534
99	2011	Yang	3.35	0.409
100	2007	Chawla	3.35	0.846

Table 3.5.1.1 (Cont'd): Calculated Tauc Ratios for a representative sample of band gap analyses, where author(s) reported bandgap spans the range of the population and Tauc Ratios range from near zero to near unity.

	Year	First Author	E_g (ref.)	Tauc Ratio
101	2010	Ma	3.36	0.315
102	2005	Tan	3.36	0.396
103	2012	Hsu	3.36	0.402
104	2013	Biswas	3.39	0.305
105	2005	Tan	3.39	0.380
106	2007	Ramirez	3.41	0.183
107	2010	He	3.41	0.262
108	2012	Hsu	3.42	0.359
109	2005	Tan	3.43	0.312
110	2011	Faraj	3.45	0.519
111	2005	Tan	3.47	0.540
112	2011	Faraj	3.47	0.868
113	2011	Faraj	3.49	0.838
114	2005	Tan	3.52	0.135

Table 3.5.1.1 (Cont'd): Calculated Tauc Ratios for a representative sample of band gap analyses, where author(s) reported bandgap spans the range of the population and Tauc Ratios range from near zero to near unity.

3.5.2 Figure of Merit Assessed

The calculation of this Tauc Ratio resulted in a broad distribution of the ratio from nearly zero to nearly unity (as shown in Figure 3.5.2.1). The median value is about 0.365, but the distribution extends broadly to both sides. The average is 0.40 and the standard deviation is 0.20.

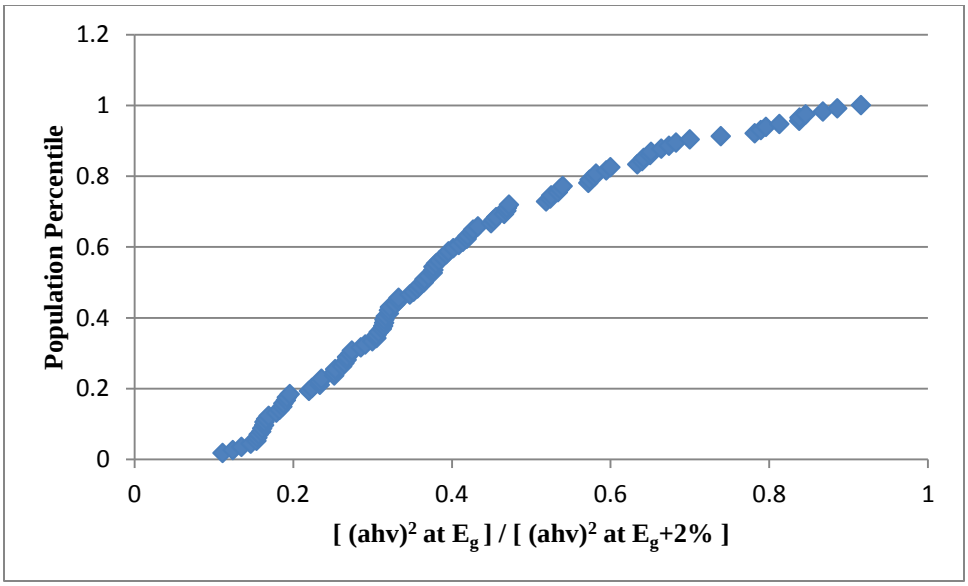

Fig. 3.5.2.1: Distribution of calculated Tauc Ratios for a representative sample from the literature survey population.

Since the larger Tauc Ratios were thought to arise from samples with larger extents of tail states in their absorption data (larger Urbach tails), an effort was made to explore its association with the different parts of the bandgap determinations found earlier. Three sub-groups of the data were selected to elucidate any relationship between published bandgaps and the calculated Tauc Ratios. Referring back to Figure 3.4.3.1.1 it was noted that there appeared to be somewhat excessive percentages of samples with notably lower or notably higher bandgap values. For further analysis published Eg values of <3.23 and >3.29 eV were chosen to demark the "low gap" and "high gap" groups with the remainder held as the "medium gap" grouping. The Tauc Ratio cumulative probability distribution for each of these three groups was then calculated and plotted, as shown in Figure 3.5.2.2. The low-bandgap range (defined with bandgap less than 3.23) resulted in a Tauc Ratio having a median of 0.472. The mid-bandgap range resulted in a

Tauc Ratio having a median of 0.315. The high-bandgap range (defined with bandgap above 3.29) resulted in a Tauc Ratio distribution with a median of 0.359.

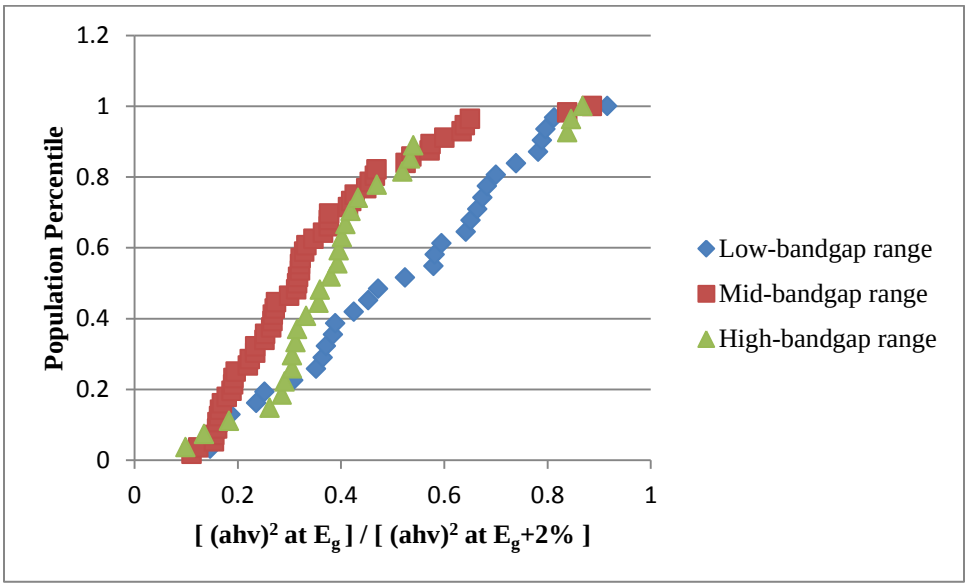

Fig. 3.5.2.2: Distribution of calculated Tauc Ratios for a representative sample from the literature survey population, separated into Low, Mid and High Bandgap ranges, as defined in the text.

These three sub-groupings of Tauc Ratio suggest that the low-bandgap group is correlated with the population having the larger Tauc Ratios in the population. It is likely that samples with more defect states below the band edge also experience a great amount of broadening of all the absorption states which can sometimes lead to difficulty in finding a good linear region for use in bandgap evaluation. This corresponds to the influence of the Urbach tail, and the likely influence of the corresponding lattice disorder in decreasing the resultant bandgap in a Tauc analysis.

3.5.3 Recommendation for Application of Figure of Merit

To investigate the hypothesis that the low Tauc Ratio population would represent those samples influenced by less lattice disorder associated with Urbach Tails, a further sampling of the population was plotted as shown in Figure 3.5.3.1. Here the entire data range is shown (essentially a re-plotting of Fig. 3.4.3.1.1) and the overlay is the cumulative probability distribution for samples with Tauc Ratios less than 0.35 (chosen at approximately the midpoint of the full population).

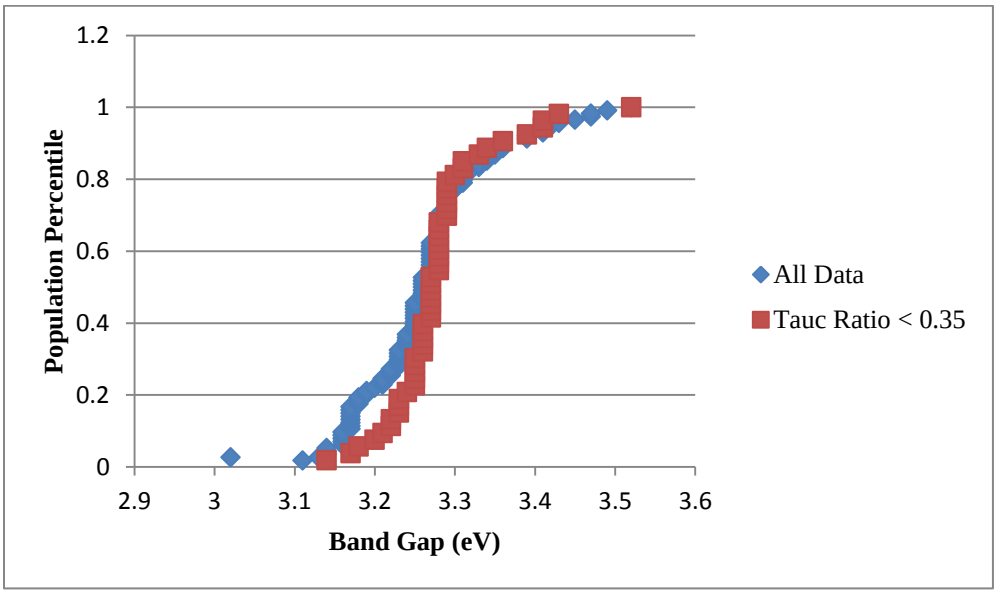

Fig. 3.5.3.1: Distribution of calculated Tauc Ratios for the entire data set and for Tauc Analyses resulting in a Tauc Ratio less than 0.35.

Clearly, the subpopulation with small Tauc Ratios has a much tighter distribution of bandgap values determined using the Tauc method. This subpopulation has an average bandgap value of 3.279 with a standard deviation of 0.065. The distributions show that while the higher bandgap assessments are represented in both populations, the lower

bandgap assessments are excluded when the defining criteria is a Tauc Ratio less than 0.35. The Urbach tails responsible for the lower bandgap assessments are not artifacts and are not noise, but do complicate the use of the Tauc analysis. There is a potential misuse if the Tauc Ratio is found to be large (e.g. > 0.35). If the ratio is small (e.g. < 0.35), there exists a greater probability of good Tauc analysis usage.

The recommendation is therefore proposed that the calculation of the Tauc Ratio for poly-crystalline absorption spectra is a valuable tool to assess the relative crystallographic disorder within a sample, where the lower the ratio the greater the order of the lattice. This may provide a quick microstructural evaluation during processing refinement, requiring few resources. Also proposed is a rating of confidence for an individual Tauc Analysis, wherein the greater the Tauc Ratio as it approaches unity the lower the confidence in the bandgap values assessed.

As a relevant and immediate implementation of the Tauc Ratio, the method of assessment was applied to the previously presented solvo-thermally grown, nano-crystallite Cu_3BiS_3 suspension Tauc analysis (Sect. 2.6 and Fig. 2.6.3 re-plotted as Fig. 3.5.3.2 below). The calculated Tauc Ratio for the Cu_3BiS_3 as produced in Chapter 2 was 0.95. Per the prior discussion, this ratio approaching unity (and well above the 0.35 benchmark demarcated) implies a great deal of crystallographic disorder and resultant intermediate states below the E_g.

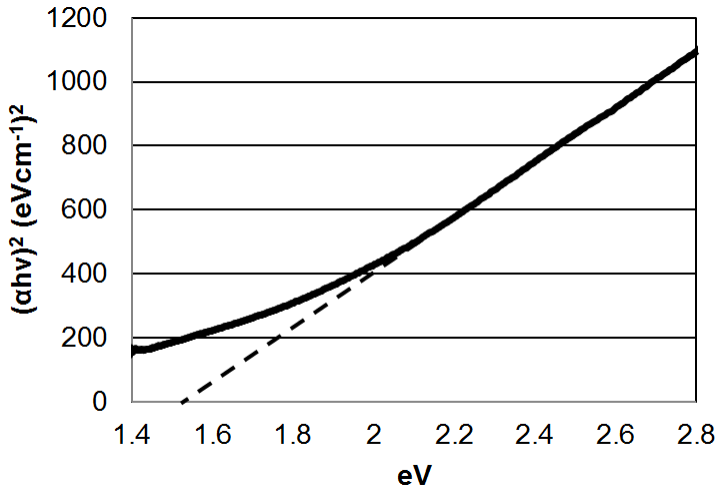

Fig. 3.5.3.2: Tauc Plot from UV-Vis spectrum of Cu_3BiS_3 precipitate as synthesized four hours into reaction (Chapt. 2) with estimated intercept at direct band gap of 1.56eV.

The elevated Tauc ratio is likely do to the physical nature of the sample as interrogated in the UV-Vis analysis. The sample was a nano-particulate suspension, and as such an inherently high degree of surface disorder may be associated with the elevated surface to bulk ratio for the material. Additionally, the material characterized was a ternary compound synthesized through homogeneous nucleation solvo-thermally, rather than a smooth thin-film initiated and grown on a clean substrate within a controlled reactor environment. The opportunity available here is the system parameter refinement for both the previously presented benchtop solvo-thermal synthesis and the reactor based deposition presented below with the aid of feedback from established Tauc analysis methods and the Tauc Ratio figure of merit methods described.

3.6 Conclusions

An assessment of the Tauc analysis method with respect to consistency, accuracy, application to polycrystalline materials and potential risk of underestimation of the bandgap was undertaken. The reproduction of a broad survey of literature based analyses in a consistent manner found that the method is robustly accurate even when applied by multiple researchers. The precision of the method was established with the finding that among over 150 analyses, the population within one standard deviation was within 0.1 eV of the accepted bandgap. This variation includes intentional or unintentional distortion of the bandgap, and so this result is particularly notable. The investigation involved the interrogation of zinc oxide, a typically stoichiometrically pure semiconductor of polycrystalline nature. That the Tauc analyses are accurate and valid for this polycrystalline semiconductor suggests that the analysis technique is applicable to not just the amorphous materials originally examined by Tauc et al[51], but to polycrystalline semiconductors as a class. Finally, the Tauc Ratio quantification of the degree of disorder imparted by Urbach tails when present and the potential for the distortion of an assessed bandgap was proposed and supported.

Four significant findings result from the work. First, it was found that there is remarkably little variance in bandgap characterization regardless of deposition or processing conditions for this simple 1:1 stoichiometric compound (ZnO). Second, the method produces results within the accepted bandgap values for this polycrystalline material, supporting the Tauc method as a robust assessment of absorption edges for not just amorphous but also polycrystalline materials. Third, the application of the digitization, extraction and determination of Tauc related bandgap data was able to be

consistently applied by three different researchers, thus confirming the robust nature of the analysis. Finally, a figure of merit addressing the degree of non-linearity in lower energy absorption, the Urbach tail, and in higher energy absorption successfully provides a method for relating the degree of purity in experimental samples.

CHAPTER 4

Continuous Flow Reactor Design

4.1 Background of continuous flow micro-reactors

Micro-reactors of varying scales are commonly employed in organic synthesis to precisely combine and react reagents in a controlled space or upon a preferred substrate. The micro designation differentiates benchtop/lab scale reactors employed for research efforts from the production scale reactors which may be modular or industrial vat sized. Established micro-reactor designs may include 10-1000μm channels into which reagent solutions are pumped via syringe or peristaltic pumping. The separate channels combine within a heated manifold to initiate the desired reaction (Fig. 4.1.1). The heated manifold may also exclude any incorporated channels and instead consist only of an enclosed chamber of several centimeters square with a chamber height of 0.1-2mm.

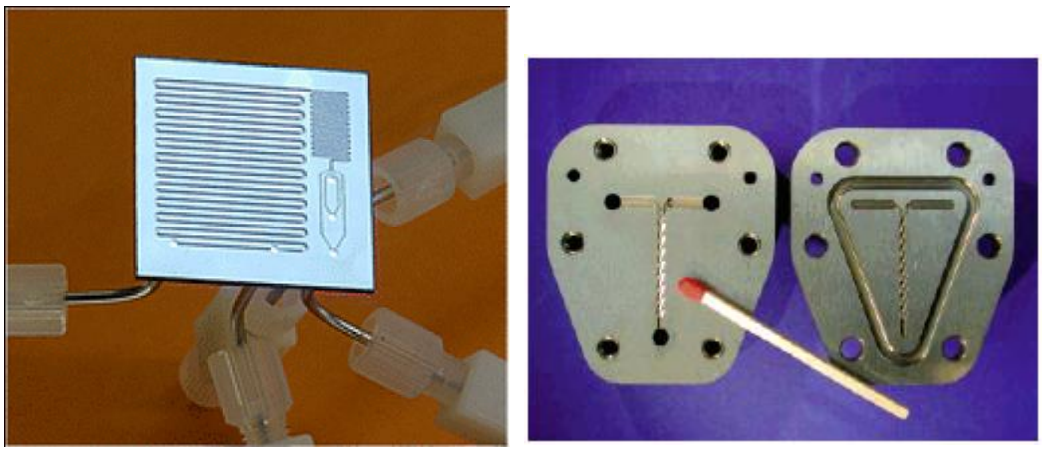

Fig. 4.1.1: Established micro-fluidic reactor designs.

Common reactor materials include silicon, stainless steel, glass and plastics. Each material must be selected with consideration for thermal resistance or conductivity, chemical inertness, durability, and machinability. While many reactions may be catalyst mediated, often the reactor environment must be heated to drive the desired process. Resistive heating methods such as jackets or strip heaters are employed from the micro to the macro scale to achieve desired temperature profiles. With these considerations, the design and build of each reactor is customizable to a specific process while allowing for rapid adaptation at the benchtop scale.

4.2 Emulating the design evolution of an inorganic continuous flow reactor

The application of previously demonstrated organic synthesis micro-reactor designs for inorganic semiconductor syntheses and deposition has been investigated and established as viable most prominently in the CdS system at Oregon State University.[215–219] Through successive design and trial from simple drop-casting of preheated reagents onto a hot platen to fully enclosed and flow optimized heated reactors (Figs. 4.2.1-4.2.4), the iterative efforts have yielded encouraging success.

The initial CdS synthesis by Chang, et al. [216] is similar to the Cu_3BiS_3 synthesis investigated here, involving the separate preparation of two solutions which are mixed prior to a pre-heating stage and eventual introduction to a heated environment for final nucleation and growth of the desired product. In Fig. 4.2.1 the simplest set-up is shown wherein the reaction space in not enclosed, but instead a heated platen exposed to atmosphere. This method is essentially the drop-cast method of semiconductor depostion,

which this thesis work involved prior to the eventual design of a Cu_3BiS_3 specific micro-reactor. Encountered in both the drop-cast and micro-reactor research streams is the need to rapidly remove reacted solution waste from the depostion area so as to allow the introduction of unreacted reagents to the surface.

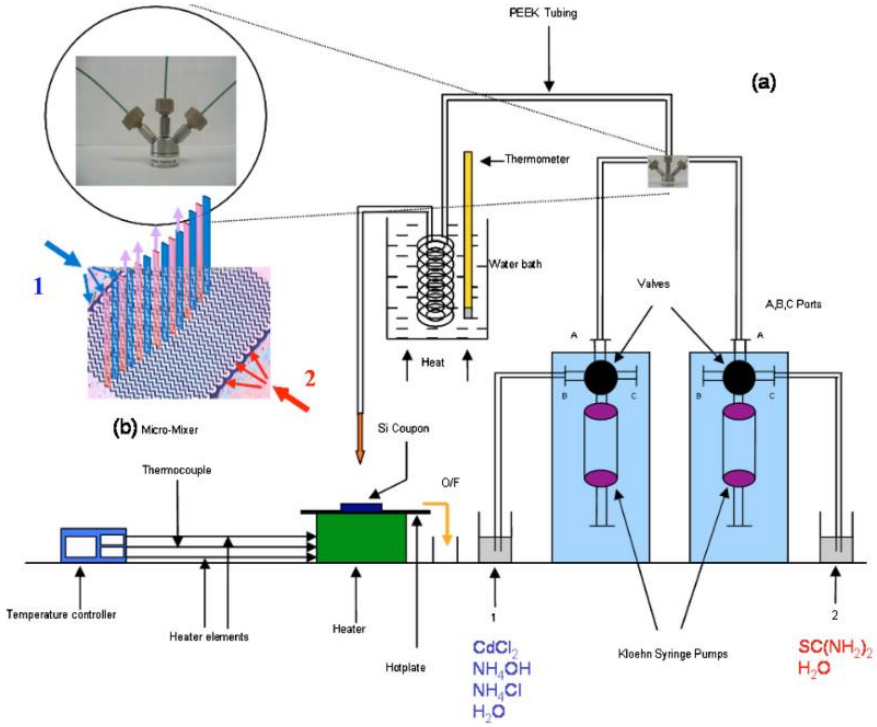

Fig. 4.2.1: Schematic diagram of a continuous flow microreactor experimental setup. [216]

The next two evolutions of CdS reactor design by Chang, et al. [220,219] address the same flow issues encountered in early Cu_3BiS_3 deposition. The simple introduction of a sloped substrate is the precursor to pumped flow through a reaction chamber (Fig. 4.2.2). Early drop-casting of Cu_3BiS_3 resulted in highly porous and highly textured coatings. The rapid heating and vaporization of

trapped solvent within the applied material for deposition produced unacceptable coatings. It was with this in mind that micro-reactor design investigation was initiated. A more complex implementation (Fig. 4.2.3) is the application of heat to the substrate while mounted on a spin-coater. This design by Chang, et al. addresses several concerns, including the rapid removal of spent precursor from the depostion area and the improved distribution of reagents on the substrate to achieve more uniform coatings. The complex relationship of revolution speed, solvent removal and induced viscosity gradient in spin-coating is an impediment to deposition optimization which was eventually overcome through the micro-reactor emulated in this thesis work.

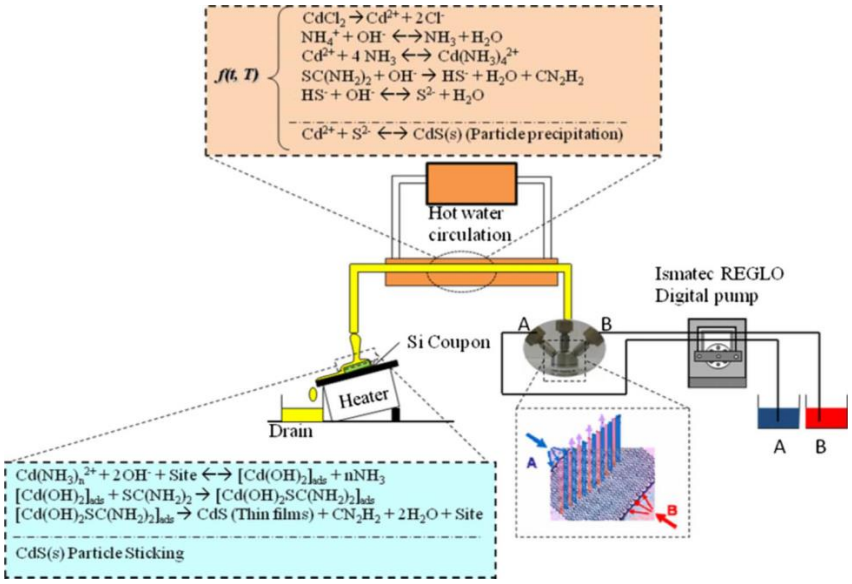

Fig. 4.2.2: Schematic diagram of further refined continous flow reactor set-up employing canted, heated coupon to provide for reacted solution removal.[219]

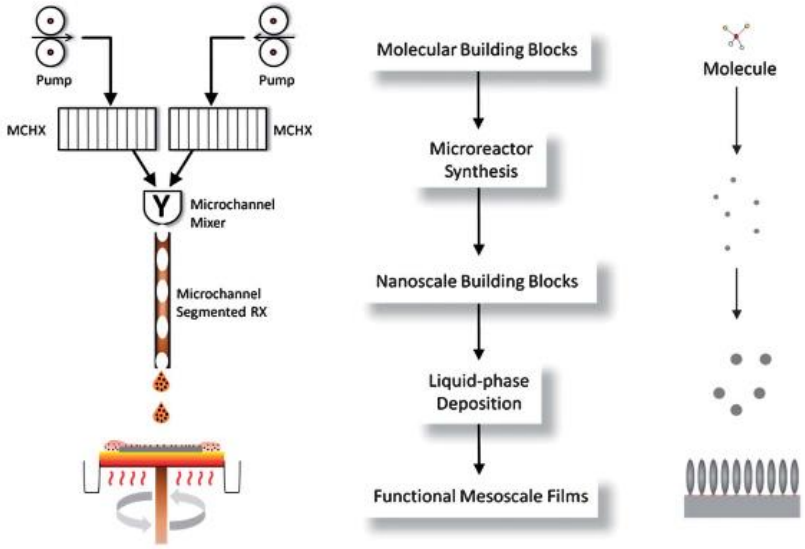

Fig. 4.2.3: Schematic diagram of spin-coating assisted continuous flow reactor improving waste solution and carrier solvent removal from a deposited film.[220]

The purpose built continuous flow micro-reactor in this Cu_3BiS_3 work most closely resembles that shown in Fig. 4.2.4, as optimized Paul, et al. [218] The figure illustrates reactants A and B mixing prior to flow through a heat exchanger, then passing through an enclosed, heated reaction chamber before the eventual discharge into a waste reservoir. Notable in this design are elements including the transparent superior platen composed of polycarbonate, the flow optimized profile of the reaction chamber spacer, and the anterior platen composed of aluminum. The low temperatures of the CdS synthesis emulated here allowed for a polymer window through which to observe the reaction, a design constraint which was elevated in the Cu_3BiS_3 reactor design to be detailed in the next section. The

aluminum anterior platen allows for thermal conduction from the resistive heater below and on to the glass depostion substrate above it.

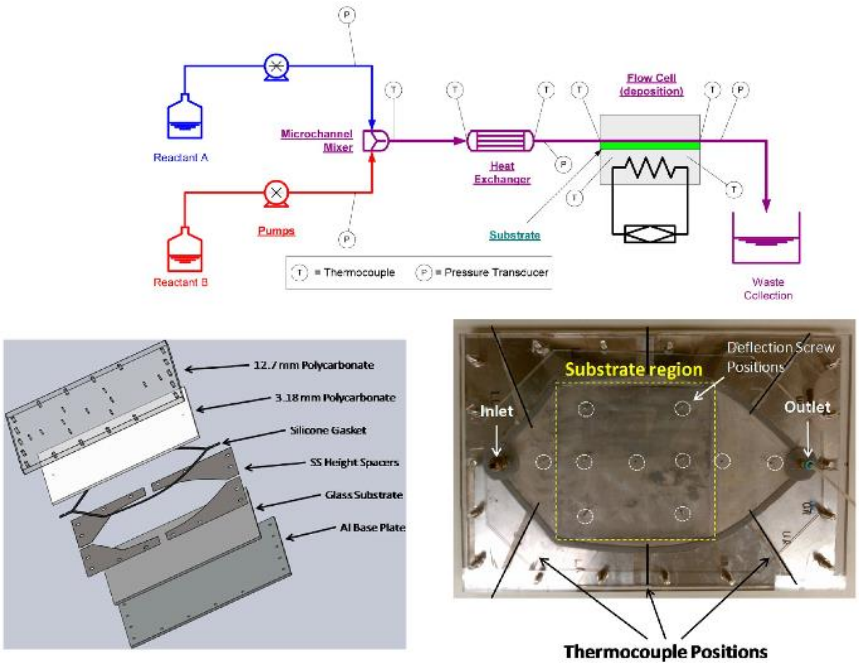

Fig. 4.2.4: Schematic of resistively heated fluidic microreactor, expanded diagram of layered reactor components, and image of assembled reactor for CdS deposition which was most closely emulated in the Cu_3BiS_3 reactor design.[218]

4.3 Design of the Cu_3BiS_3 specific continuous flow micro-reactor

As the chemical pathway has been established in literature and remains under protection of a provisional patent, it was a fundamental goal to employ the synthesis method detailed in Chapter 2 without adaptation unless required to complete the growth of a fully thick target film. The primary goal was the translation of the single-pot, two neck flask synthesis of nanoparticles generated by homogeneous nucleation and

subsequent particle growth into a continuous reactor thin-film growth synthesis generated by nucleation at the substrate surface and subsequent film growth in the normal direction.

The idealized reactor design, based on knowledge of the proven Cu_3BiS_3 synthesis and study of the CdS reactors in literature [216,218–220], is illustrated in the cartoon in Fig. 4.3.1 and each component is discussed in greater detail from the bottom of the reactor up in the following sections. A reaction space (reactor) is enclosed to contain fluid flow over a substrate on which the Cu_3BiS_3 semiconductor is to be deposited. The reactor is bounded on the bottom by a platen (See section 4.3.1), on the sides by walls (See section 4.3.3), and on the top by a lid (See section 4.3.4). The reactor has two types of fluid ports, the first of which type allows for the introduction of precursor chemical reagent fluids by one or more openings. The second type of port allows for the extraction of post-reaction fluid and particle media. These ports may exist in the lid or the walls, were initially designed to exist in the lid, and were eventually moved to the walls per design constraints (See section 4.3.4).

In between the two types of ports is a region where the deposition substrate is in contact with a heated platen. The platen is heated in two regions (Zone 1 and Zone 2) separately and at different temperatures in order to provide a temperature gradient in the platen, the substrate and the fluid along the direction of fluid flow (x-direction). Zone 2 is at a higher temperature than Zone 1. A temperature gradient profile is thus also created in the fluid in the direction perpendicular to fluid flow (z-direction) via conduction. This z-direction temperature gradient in the fluid reaches its minimum at the surface of the reactor lid, resulting in a heated region of the lid (Zone 3) via conduction which is less than that of Zone 1 and therefore Zone 2 as well.

TempZone 3 < TempZone 1 < TempZone 2

The Zone 1 and Zone 2 temperatures are controlled such that the temperature at which the desired reaction proceeds is met or is exceeded between Zone 1 and Zone 2 in a region at the surface (preferably) and immediately above the substrate (also attractive). The reaction thus proceeds to deposit and grow the semiconductor on the substrate, utilizing reagents which are delivered by fluid flow in the x-direction and by diffusion in the negative z-direction.

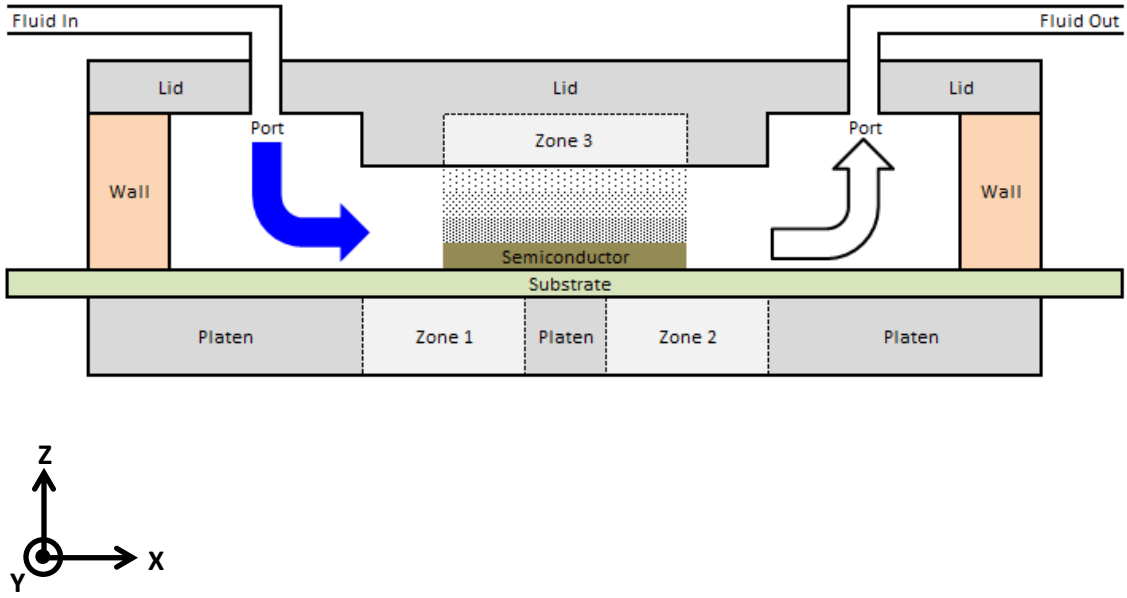

Fig. 4.3.1: Schematic of idealized continuous flow reactor for Cu_3BiS_3 deposition showing solution flow through ports, zones of differential heating and area of semiconductor deposition.

4.3.1 Reactor bottom platen

The bottom reactor platen serves two purposes. Structurally it is the backbone of the reactor, supporting the containment components in subsequent layers above as well as the heating elements within or below. Thermally it is the conduction pathway from the resistive heaters to the deposition substrate. Optimizing both constraints and considering machinability, 3/8 inch thick 6061 aluminum was sourced from McMaster-Carr. The as delivered stock was cut and drilled to produce a 102mm by 127mm plate with 3/8 inch holes at each corner, on center 12.7mm from each edge.

4.3.2 Reactor chamber bottom/substrate

Immediately above and in contact with the bottom platen is a plate of glass, which may or may not serve as the deposition substrate. When employed solely as an inert containment surface for the reaction chamber, soda-lime glass of dimensions 3 inches by 4 inches manufactured by Ted Pella, Inc. and sourced from Fisher Scientific Co. was used as delivered excepting solvent washing. In this case deposition substrates such as FTO coated glass, Molybdenum foil or Titanium foil coupons were placed on the glass chamber bottom. When employed as both the reaction chamber bottom and as a deposition substrate, FTO coated glass of the same dimensions as cut was sourced from Sigma-Aldrich and subjected to more extensive surface preparation as detailed in section 5.1.3.

4.3.3 Reactor walls

Surrounding and defining the height of the reaction chamber, the reactor wall must be chemically inert and provide a liquid-tight, non-pressurized seal between the reactor bottom and reactor lid. Red rubber silicone mat of 1/8 inch thickness was sourced from McMaster-Carr. A sealing/containment gasket was cut from the mat with outside dimensions of 76mm by 102mm, matching the reaction chamber glass bottom dimensions, and inside dimensions of 60mm by 85mm. Initial reactor trials wherein the inlet and outlet ports were placed in the lid of the reactor allowed for continuous wall sealing by the silicone gasket. Subsequent trials wherein the ports were moved to the walls required cutting the gasket, inserting the silicone transport tubing in the gap, and sealing with an air-curing RTV silicone gasket compound of the same material class as the mat itself.

4.3.4 Reactor Lid

Completing the enclosure of the reaction space, the reactor lid is preferably transparent, a non-preferential deposition surface, and the site of the inlet and outlet ports. Transparency allows for imaging of the reaction as it progresses, just as the fluid flow and reaction wave front were analyzed Paul, et al.[218] Per the description of the heating zones and the preferential deposition of semiconductor (Cu_3BiS_3) on the bottom surface, as sourced soda lime glass was used with the same dimensions as the reactor bottom glass. As noted and depicted in the cartoon (Fig. 4.4.1), the inlet and outlet ports are preferably sited within the reactor lid. Early iterations of this work attempted the use of polyethylene terephthalate (PETG) which is transparent and allowed for easy drilling of

holes for insertion of tubing fittings. Bulk PETG sheets of 1/8 inch thickness were sourced from Fisher Scientific Co. and cut dimensions matching the outside dimensions of the reactor walls and the reactor chamber bottom/substrate (76mm by 102mm). While the melting point of PETG (250ºC) is above the required reaction temperature (156ºC), the softening point under the stresses in this application (~90ºC) obviated its use.

A further intermediate iteration in lid design sourced precision drilling services to cleanly port the soda-lime glass for introduction of the inlet and outlet fittings sealed with high-temperature silicone sealant. The resulting stress risers imparted to the glass, however, in combination with the residual stresses from the glass forming process resulted in crack initiation at the ports and propagation to the point of containment failure at or above the reaction temperature (>156ºC). Thus the choice was made to move the ports to the reactor walls (See section 4.3.3) and as sourced soda-lime glass was used in all successful experimental depositions.

4.3.5 Reactor top platen

The top platen must serve as the counterpart to the bottom platen, structurally, while providing a window for observation of the reaction through the transparent reactor lid. The same 3/8 inch thick 6061 aluminum as sourced from McMaster-Carr was cut and drilled to produce a 102mm by 127mm plate with 3/8 inch holes at each corner, on center 12.7mm from each edge. Additionally a centered rectangle 68mm by 93mm was cut from the plate to provide the window required. Bolts were secured through the holes of the top and bottom platen, with the reactor bottom, walls and lid pressed between them. To ensure a liquid tight and chemically inert seal for the entire perimeter, silicone

vacuum grease was applied to the top and bottom surfaces of the silicone gasket (walls) prior to assembly.

4.3.6 Reactor heating

The two heated zones of the reactor design (See Fig. 4.4.2) required discreet heating elements each with a dedicated power channel. Kapton enclosed resistive strip heaters ½ inch wide by 4 inch long with pressure sensitive adhesive (PSA) providing a maximum 10 watts per square inch were sourced from Omega Circuits and Engineering Corp. These were adhered to the underside of the bottom platen 1.75 inch on center and 2.75 inch on center from the platen edge of the inlet side. Their placement was chosen to provide sufficiently discrete heating zones which were both oriented nearer the inlet than centered on the platen. With these design parameters and in continuous flow conditions the rate of heat transfer from the heaters through the aluminum platen and glass substrate and into the reagent solution would create a heated fluid profile over more of the chamber. The heaters were powered by a Sorenson XPF 35-10 two-channel DC power source capable of constant voltage or constant current, sourced from Test Equity, LLC and set at constant voltage (24V). In practice, the wattage limitations of the Kapton strip heaters necessitated setting the reactor on a typical laboratory heating plate to provide a heated environment around the reactor. Also implemented was an aluminum heat shield and air flow suppressor to further contain the heated air mass surrounding the reactor and reduce heat loss within the fume hood.

4.3.7 Precursor solution pre-heating and pumping

In order to meet or exceed reaction temperatures (~156ºC) within the reactor while delivering initially room temperature pre-cursor solutions to the reaction chamber, a precursor solution pre-heating bath was introduced between the peristaltic pump and the reactor inlet. The inlet tubing, platinum-cured silicone with internal diameter of 1.6mm delivered unheated but mixed precursor solution to the inlet of the Thermo Scientific FH100 peristaltic pump, both of which were sourced from Fisher Scientific Co. The outlet tubing of the pump was of sufficient length for a minimum of 100cm of tubing to be coiled and immersed in a silicone oil (high-temperature capable – sourced from Sigma-Aldrich Co.) bath under stirring, heated by a typical benchtop heating plate. The temperature of the bath was monitored by thermocouple and held in the range of 135-145ºC. The pump provided a range of volumetric delivery rates between 0.5-3000mL per minute.

4.4 Modeling and operation recommendations for reactor operation

The fluid flow and heat transfer within the reactor as designed was evaluated within the COMSOL modeling software. Initial design parameters were communicated to a colleague skilled in building models within the software, and through iterative modification and review of results a relevant model was produced to investigate the most critical aspect of the reactor, the heat profile within the reaction chamber. Input parameters included all dimensions, materials and their associated heat capacities and densities, expected flow rate bounds, and expected temperatures of the two Kapton encased strip heaters. The initial design of the upper platen is shown in blue within

Figure 4.4.1, with remaining assembly parts shown in wireframe. The initial inlet and outlet designs penetrating the upper platen are shown, and the offset of the strip heaters is apparent. The walls of the reaction chamber are shown in blue Figure 4.4.2 and the heater placement is yet more apparent.

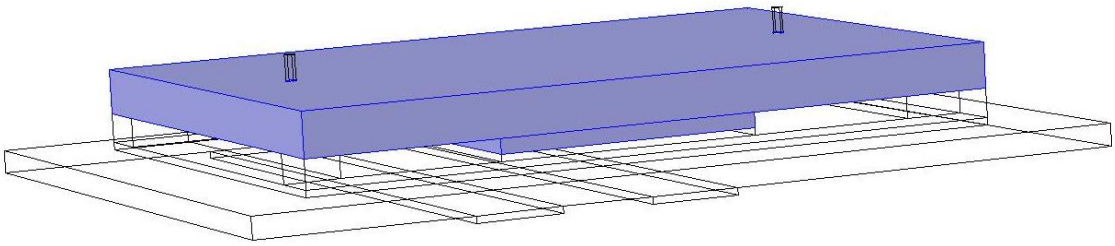

Fig. 4.4.1: COMSOL modelling structural image with reactor lid displayed in blue and remaining reactor in wireframe. Idealized fluid inlet and outlet positions are visible in the lid.

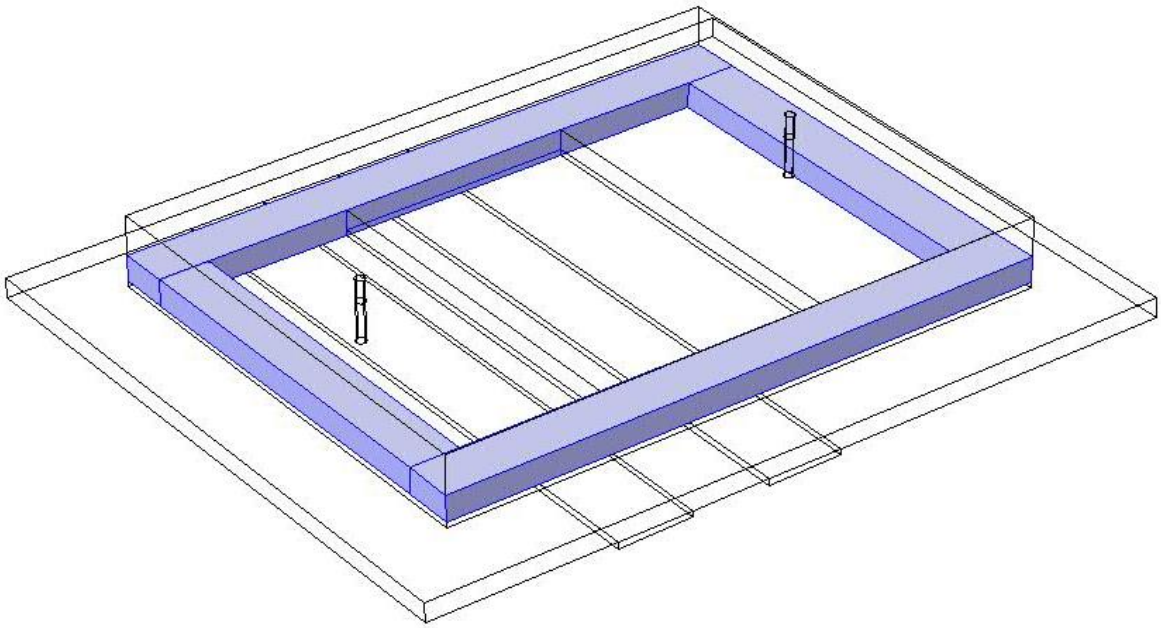

Fig. 4.4.2: COMSOL modelling structural image with reactor walls displayed in blue and remaining reactor in wireframe. Kapton encased resistive strip heater placement is evident in offset from center on the bottom platen.

The COMSOL model was run with consistent modelling parameters for structural elements and heating element temperatures, but with varying flow rates (Fig 4.4.5). This reflects the practical consideration that the low available wattage of the strip heaters necessitated providing maximum power and therefore maximum heat flow in order to meet or exceed the reaction temperature with the chamber. For modelling purposes, then, the flow rate best exemplified the degree of freedom in heat flow during steady state conditions.

The lower bound of flow rate during modelling, set at 2.3 ml/min, provided insufficient consistency across the flow plain as seen in Fig. 4.4.3. The pre-heated

precursor solution entered the chamber with a consistent temperature profile, but with such low flow conditions the temperature of the entire solution was quickly driven well above the reaction temperature. This temperature rise was great enough to negate the possibility of maintaining a temperature gradient in the z-direction which would allow synthesis and deposition at the substrate but not at the surface of the top platen.

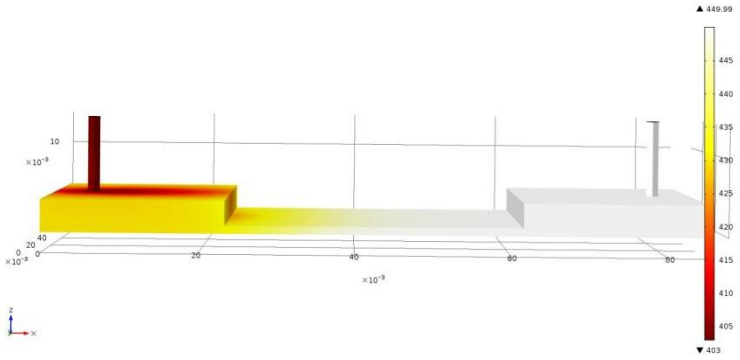

Fig. 4.4.3: COMSOL model heat flow projection for lowest flow condition (2.3ml/min), showing lack of requisite temperature profile in z-direction.

The upper flow rate bound for modelling, set at 230 ml/min, provided a more consistent temperature gradient in the z-direction from the inlet to the outlet. With such a high fluid velocity this was expected, but the resulting fluid temperatures at the substrate were below the 156ºC necessary to initiate and sustain the synthesis reaction.

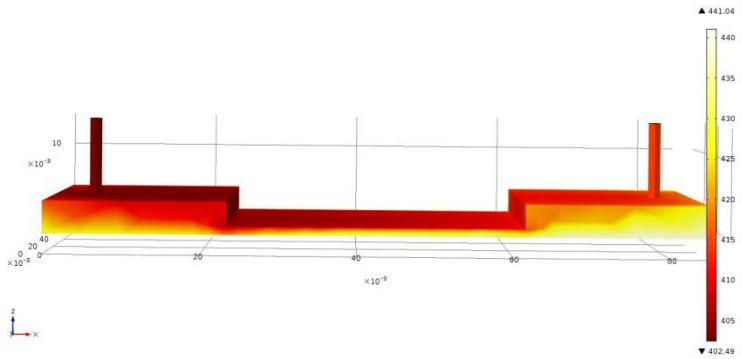

Fig. 4.4.4: COMSOL model heat flow projection for highest flow condition (230ml/min), showing temperature profile in z-direction but less than required temperature at substrate surface (156ºC).

Through iteration the model was examined for a flow rate boundary condition which would satisfy the initial design requirements. To reiterate, a temperature gradient is desired so that the temperature at the substrate surface exceeds the reaction temperature and the temperature at the top platen surface is below the reaction temperature. Additionally, it is preferable that a gradient exists at the substrate surface so that it is higher nearer the inlet and lower nearer the outlet while still exceeding the reaction temperature. Figure 4.4.5 displays discrete flow values and the corresponding critical temperatures.

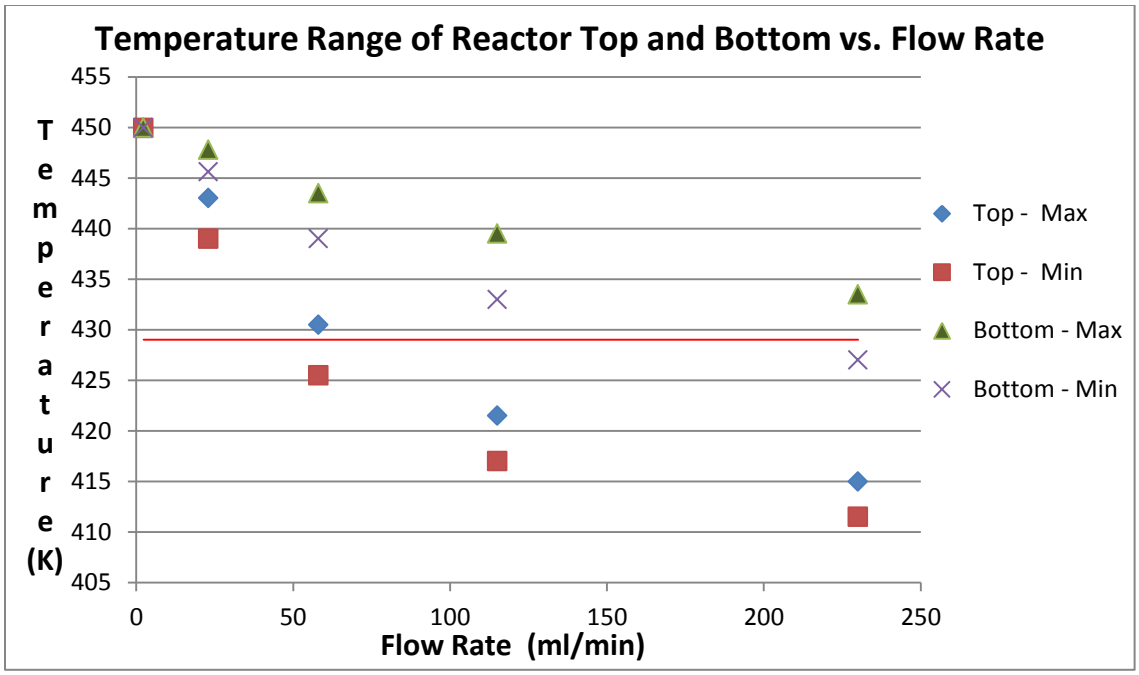

Fig. 4.4.5: Modelled temperatures for varying flow rates, including maximum at top, minium at top, maxium at bottom, and minimum at bottom. Synthesis reaction temperature required shown in red line.

From the modelling effort the ideal reactor design was shown to operate within temperature constraints well at 115 ml/min. While the model was not inclusive of surrounding thermal conditions (e.g. air flow rates within a fume hood), the exercise demonstrated the viability of such an ideal design and set initial operational flow rates for experimentation.

CHAPTER 5

Implementation of Continuous Flow Reactor for Solvothermal Cu_3BiS_3 Thing-Film Deposition

5.1 Reactor Manifestation

The extensive pre-build investigation of the continuous flow reactor detailed in Chapt. 4 provided a blueprint for the first implementation of the technology in synthesizing Cu_3BiS_3. As previously noted, early operational tests informed component dimension and material refinement resulting in the reactor set-up as utilized.

All equipment required for the reactor operation except for the reactor itself was readily and inexpensively sourced. The reactor build required intermediate machining tools, including an aluminum capable saw blade mated to a reciprocating saw, a drill press, and cutting blades sufficiently sharp to cleanly sever the red silicone gasket. Heating elements as sourced shipped with operational temperature capable adhesives, and the installation of the elements in position required only pressure. Once the individual reactor elements were produced the assembly (and disassembly) of the operational reactor was accomplished through careful alignment of the bottom platen, the bottom/substrate, the walls, the lid, and the top platen. The pre-drilled holes along the reactor platen edges allowed bolts for securing the reactor closed and for elevating the reactor for air flow.

5.1.1 Fluid Pathway

The manifestation and operation of the reactor and supporting elements is best understood by following the fluid path from pre-cursor solution as the system input toward spent solution as the output. Visible in Fig. 5.1.1.1, the input pre-cursor solution (A) (Sect. 2.4) is conveyed via silicone tubing to the input solution pre-heat bath (B) (Sect. 4.3.7). The pre-heat bath temperature is maintained between 133ºC and 145º C, slightly below reaction temperature of 156ºC, and monitored via the thermocouple (C) immersed in the bath and the temperature display (D). The pre-heat bath is heated by a heating plate (H). The pre-heated pre-cursor solution is conveyed to the peristaltic pump (E) (Sect. 4.3.7) and then to the reactor (F).

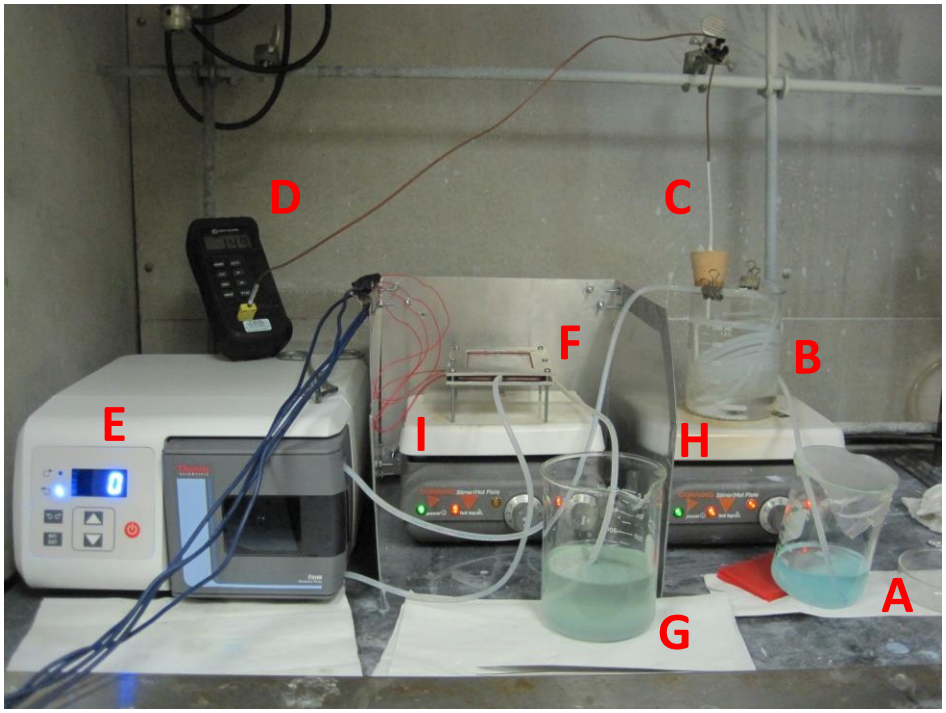

Fig. 5.1.1.1: Continuous flow reactor (F) instrumented with supporting elements: A) input pre-cursor solution, B) input solution pre-heat bath, C) pre-heat bath thermocouple, D) pre-heat bath temperature display, E) peristaltic pump, F) contiuous flow reactor, G) output spent solution, H) pre-heat bath heat source, I) supplemental reactor heat source.

The reactor is maintained at a temperature greater than the required reaction temperature (156ºC) by two means. The adhered Kapton strip heaters (Sect. 4.3.6) are integral to the reactor and are driven by an external DC power source (Fig. 5.1.1.2). As previously noted, the heat flux limitations of the reactor design necessitated the implementation of a heating plate (I) as a supplemental reactor heat source. The Cu_3BiS_3 synthesis reaction occurs entirely within the reactor, depositing crystalline product on the encased substrate, and the waste solution is conveyed to a receptacle (G).

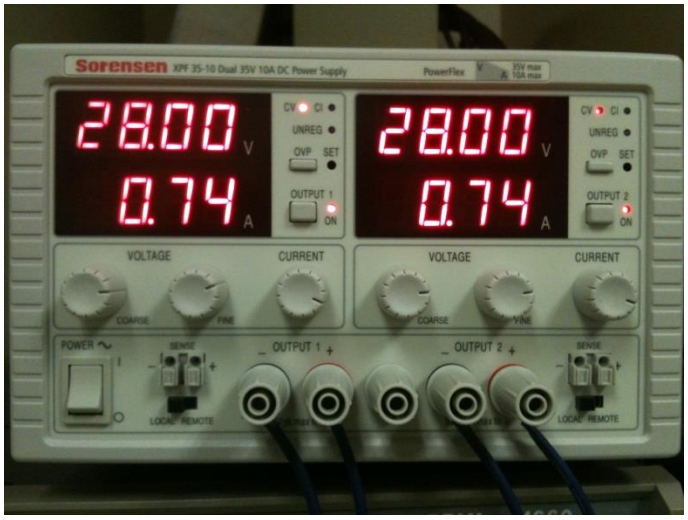

Fig. 5.1.1.2: External DC power source driving the Kapton strip heaters integral to the reactor.

5.1.2 Reactor Heat and Air Flow

Idealized reactor operation includes the presence of a temperature gradient along the reaction flow direction from input to output (Sect. 4.3), provided by the two differentially driven Kapton strip heaters attached to the bottom platen. In practice the capability of the integral heating elements was insufficient to produce an environment within the reactor suitable for reaction (>156ºC). Necessarily the reactor was placed on a supplemental heating plate (Fig. 5.1.1.1. element B). Direct contact between the heating plate and the reactor resulted in uneven heating of the reactor, as evidenced by distinct regions of pre-cursor solution boiling (>190ºC) in contrast with ideal reaction temperature regions above 156ºC but below 190ºC. By implementing longer reactor clamp bolts to function as stand-off mounts from the heating plate surface, the entire reactor chamber was able to be maintained within the temperature constraints.

Though sufficient heat flow to the reaction chamber was thus provided, consistent heat flow was inhibited by the changing environment of a laboratory fume hood. Varying conditions within the laboratory and within the hood modulated the flux and direction of air flow around the reactor, resulting in modulated heat flow to the reactor chamber. An aluminum plenum was implemented to surround the reactor and supplemental heating plate on three sides, allowing for the safe but consistent flow of air around the reactor and through the fume hood to exhaust.

5.1.3 Substrate Preparation and Operating Parameters

Successful deposition of Cu_3BiS_3 nano-crystallites within the operating reactor is enabled by consistent substrate preparation and iterative operating parameter refinement. The substrate consists of FTO coated glass sourced from Sigma-Aldrich and hand cut to the reactor perimeter dimensions (102mm by 107mm). Matching these dimensions provides for the most complete seal against the red silicone rubber reactor walls and guaranteed containment of the liquid phase within the reactor. Preparation of the substrate began with a thirty minute soak in 0.1N (0.1M) potassium hydroxide (KOH) solution in methanol in order to remove active organic species from the surface. Immediately following this is a deionized water rinse and a subsequent acetone rinse to eliminate reacted species and remaining KOH before drying under nitrogen gas flow.

Operating parameters for the various heating components and the centrifugal pump were determined by trial inside of proposed boundary conditions. These conditions were informed by the previous establishment of a flask based synthesis (Chapt. 2) and the reactor modelling performed in the reactor design phase (Chapt. 4). Most critical to

successful synthesis is the instantaneous heat of the mixed precursor solutions within the reactor. The first generation reactor used for these investigations included two 40 watt Kapton heaters encased strip heaters which were insufficient to heat the reaction space above the required 156ºC necessary for the synthesis to proceed; as such, the heaters are driven with maximum allowable power. The power supply dual channels (Sect. 4.3.6) are set to constant voltages of 28V and each channel draws 0.74A. A heating plate providing supplemental heat flow from beneath the reactor is set at level eight out of ten relative units.

The pre-cursor solution pre-heating bath is likewise heated from below by a heating plate. In order to maintain the required temperature range of 133º to 145ºC within the bath under stirring the heating plate was set at level seven out of ten relative units. The pre-cursor solution pre-heating and the reaction space mixed solution heating impart constraints on the boundary conditions for solution flow velocity. Heat transfer from the reactor platens and walls to the solution flowing within the reactor must be sufficient to maintain the solution temperature above 156ºC to drive the reaction and below 190º C to prevent solvent boiling. The window of available pump velocities for the first generation reactor and associated heating parameters is then found experimentally to be 0.5 ml/min. (the pump minimum) to 4.0 ml/min. The maximum within this range is used for the syntheses reported here, as it provides the most expedient growth on the substrate.

5.2 Results

Operation of the continuous flow micro reactor in the manifestation and utilizing the operating parameters described resulted in the growth of deposits of copper bismuth sulfide phase with varying morphologies none of which, unfortunately, were directly suitable for solar-cell device fabrication. Examination of the microstructures gives insight into ways that the structure had formed and allows suggestions for improving deposition in the future. The phases present in deposited films were characterized by X-ray diffraction and determined to be predominantly preferred Cu_3BiS_3 (Wittichenite) and some second phases, depending on reactor operating temperature. Confirmation of the presence of solely copper, bismuth and sulfur was executed through EDX analysis and revealed even spatial distribution of these elements in the film plane. FESEM imagery revealed the deposition and growth of nano-platelets, micro-platelets, dendrites and coral (or flower) like structures consistent with prior literature on solvo-thermal synthesis of Cu_3BiS_3. While the microstructures are not ideal for immediate solar device construction, the reactor was successful in making predominantly the desired phase. Together this evidence presents a successful scenario for the transfer of the original flask based synthesis employing a novel chemistry to the prototype continuous throughput micro-flow reactor designed within this body of work and provides the basis for making recommendations for further improving the reactor design and coating morphology.

5.2.1 Growth Morphologies

Microstructure details were obtained at a variety of locations from samples of reactor-grown copper bismuth sulfide on FTO coated glass. Imaging was acquired with a field-emission scanning microscope (FESEM), model Zeiss Sigma. Several morphologies were observed for the growth of copper bismuth sulfide. These included areas with evidence of surface nucleation and growth as well as more distinct platelet growth at different size scales, as shown below.

The nucleation and initial growth of copper bismuth sulfide on the FTO coated glass substrate are evident in Fig. 5.2.1.1. Bare FTO is visible in the center of the micrograph; numerous evenly-distributed nucleation sites can be seen on the right side; and, more developed advanced stages of early growth can be seen on the left of the image. The presence of many distinct islands of initial growth on the right side suggests the substrate provides many simultaneous sites for nucleation, which is an encouraging prospect for the eventual growth of a dense thin film of controlled thickness. The absence of growth from the nucleation sites in the central region is similar to the "denude zones" often seen for Ostwald ripening-type processes where there is a component of diffusive mass transport: the presence of the growing crystalline zones to the left can deplete nearby solution of reactant, which makes it less supersaturated and therefore more difficult to initiate nucleation in that zone that is close to other crystallization.

Further, the shapes of the more advanced growth on the left in Fig. 5.2.1.1 and Fig. 5.2.1.2 have patterns reminiscent of diffusion-limited-aggregation (DLA), a process where growth is accentuated at the higher spots and gets more exaggerated/rougher with time. The nucleation and growth of free-floating crystallites within the solution and

subsequent diffusion to the surface contributes to roughness exaggeration as well. Features which protrude above the surrounding surface have a greater probability of receiving diffusing crystallites. A broader view of this growth mode of copper bismuth sulfide film at progressively larger magnifications can be seen in Fig. 5.2.1.2.

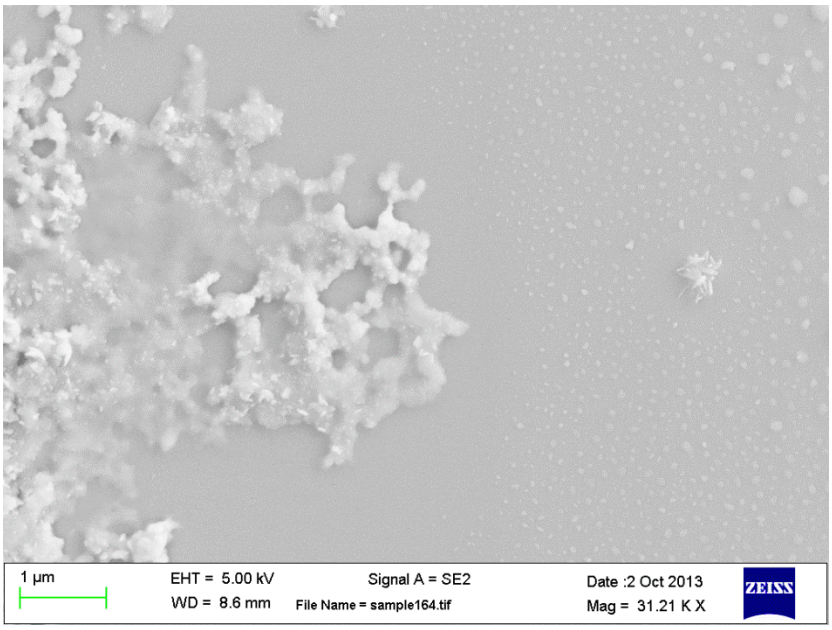

Fig. 5.2.1.1: SEM micrograph of copper bismuth sulfide grown in continous flow microreactor showing bare substrate FTO (center region), evidence of nucleation and early growth (right) and developing growth (left).

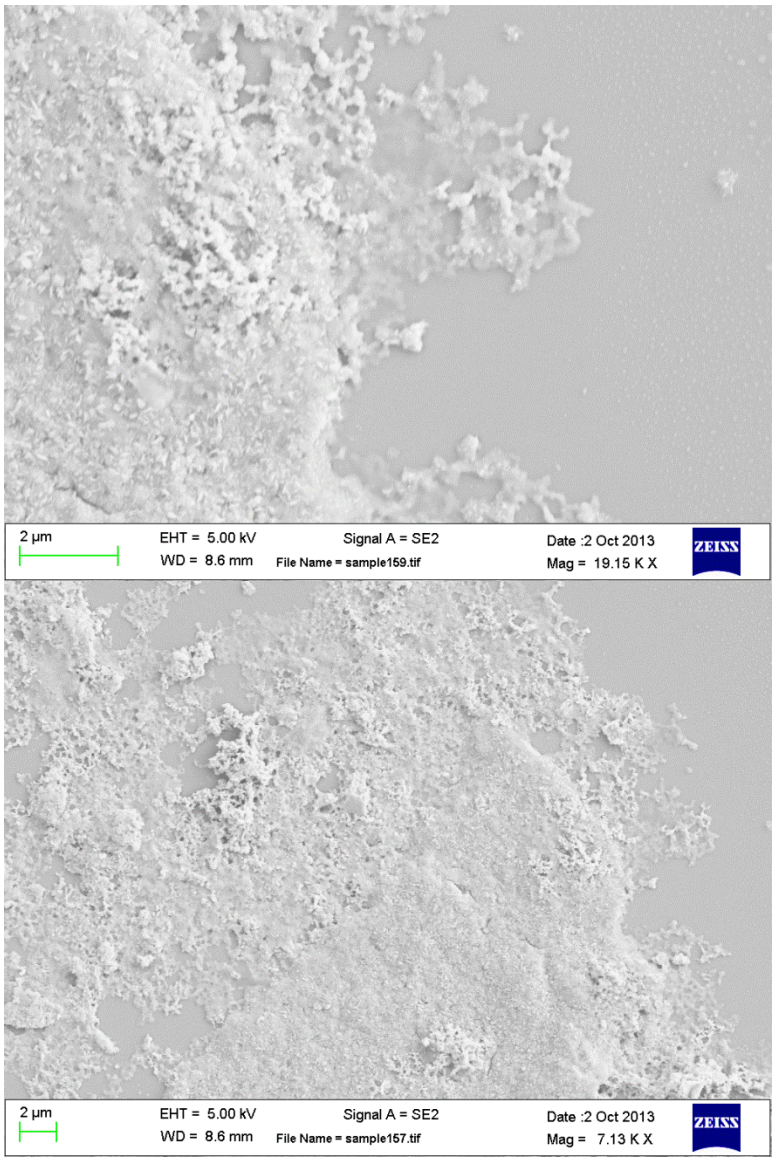

Fig. 5.2.1.2: SEM micrographs of copper bismuth sulfide grown in continous flow microreactor exhibiting zones of early particle growth (top) and with secondary particle deposition/aggregation (bottom).

Another example of this mixed deposition can be seen in Figure 5.2.1.3; the platelets (lower left) and thicker film sections (center) were the predominant forms with film section dimensions on the micrometer scale along the x-y plane corresponding to the

substrate surface. This morphology suggests the even and simultaneous deposition of an initial seeding layer (as seen initiated in Fig. 5.2.1.1) and further growth of a polycrystalline film-like structure. The presence of a majority of grown copper bismuth sulfide in this form is an encouraging step toward the deposition and growth of a fully dense Cu_3BiS_3 film on a functional substrate (FTO coated glass), which would be more suitable for device integration.

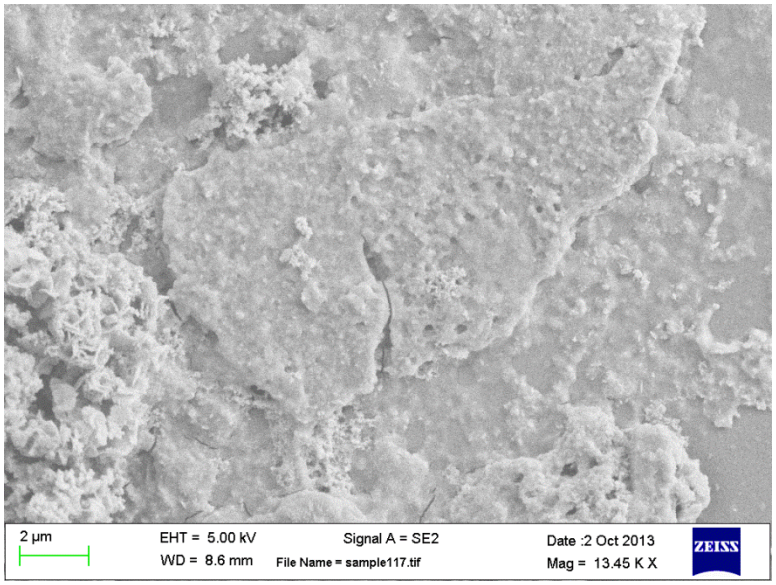

Fig. 5.2.1.3: SEM micrograph of copper bismuth sulfide grown in continous flow microreactor exhibiting platelet morphology (lower left) and a thin-film section (center).

The nano-scale platelet morphology was observed in samples having either unconstrained or constrained configurations. Unconstrained growth is evident in the lower left of Fig. 5.2.1.3 where the region is of varying thickness and is unbounded on the sides. Constrained growth occurred wherein some film sections on the micrometer

scale were composed of micro or nano scale platelets preferentially oriented in planes around the z-axis (the substrate normal). This resulted in a nano-porous film section as seen in Figure 5.2.1.4. It is suggested that under continued reaction conditions within the reaction chamber these film sections may densify through the further growth and necking of the individual nano-platelets, resulting in a more fully dense film.

The preparation of FESEM samples resulted in the dislodging and upending of some coating sections, as visible in the top third of the top image in Fig. 5.2.1.4. The pattern of growth shown here corresponds to the locations at the surface of the FTO coated glass substrate where nucleation had occurred as represented in Fig. 5.2.1.1. The density of those nucleated sites may correspond to the density of nano-platelets comprising the film section, and therefore may be useful baseline information for any research seeking the densification of the nano-porous film sections.

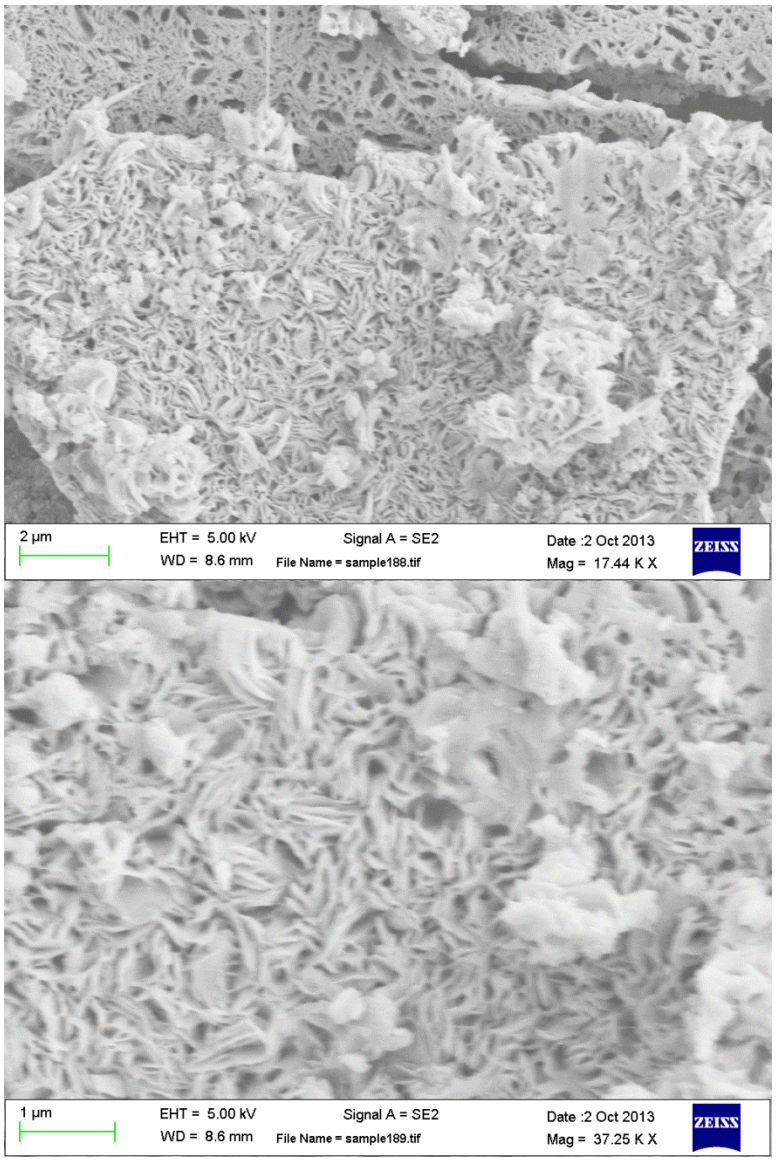

Fig. 5.2.1.4: SEM micrographs of copper bismuth sulfide grown in continous flow microreactor exhibiting semi-porous film structures composed of nano-platelets preferentially oriented in the z-direction.

Another morphology observed is coral (or flower) structures also noted in prior Cu_3BiS_3 solvothermal synthesis studies.[35] In contrast with the broadly dispersed particulate believed to have precipitated within solution and settled on the substrate, these

coral structures originate on the substrate surface in limited regions (Fig. 5.2.1.5). The packing/proximity of these structures to each other is in correspondence with the nucleation sites visible in the lower third of this micrograph and that in Fig. 5.2.1.1.

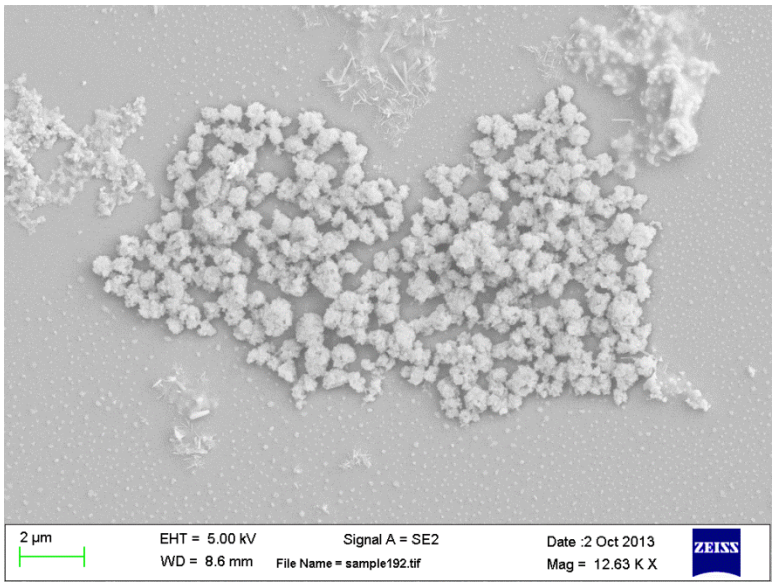

Fig. 5.2.1.5: SEM micrographs of copper bismuth sulfide grown in continous flow microreactor exhibiting coral (or flower) morphology and contained in localized regions within the reactor. Corresponding nucleation sites are present in similar spacial density.

Also notable in the top center of Fig. 5.2.1.5 is the presence of needle-like structures. These dendrites/needles are consistent with particle shapes sometimes created in other solvothermal syntheses employing L-cysteine[41,47]. Similar morphology of vertically oriented platelet growth on the scale of up to ten micrometers has also been seen in combination with a more dense microstructure (see Fig. 5.2.1.6). Elimination of these non-preferred structures (coral-like and micrometer scale platelets), which would

disrupt the growth of smooth films, may be possible with a more consistent heating profile and refinement of the fluid flow profile thus exerting more control on the growth conditions within the reactor.

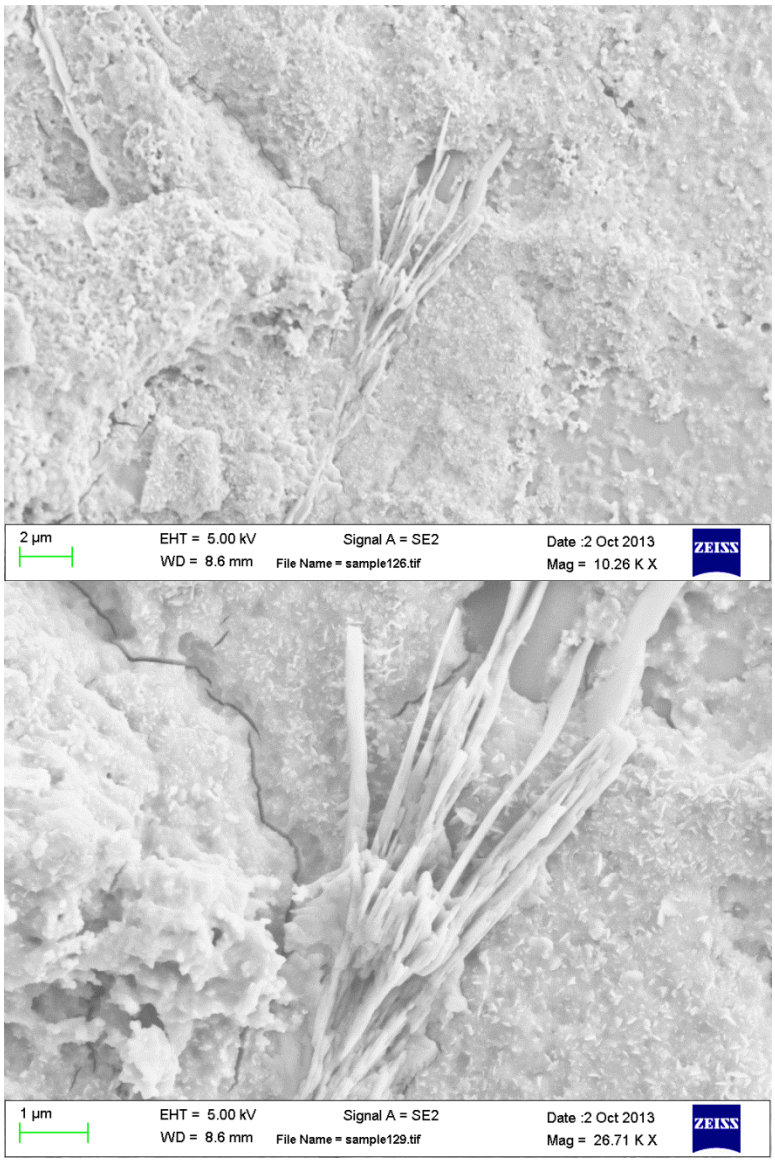

Fig. 5.2.1.6: SEM micrograph of copper bismuth sulfide grown in continous flow microreactor exhibiting vertically oriented micrometer scale platelets.

5.2.2 Phase Analysis of Copper Bismuth Sulfide Product

Elemental analysis and phase determination were performed on as-grown samples without any post-deposition chemical treatment or annealing. EDX analyses were performed with a field-emission scanning microscope (FESEM), model Zeiss Sigma, and phase determinations were performed using Cu-K_α radiation with a wavelength of 1.54 Å on a Siemens Kristalloflex diffractometer controlled by MDI Data Scan. Two separate sample regions were examined by EDX shown in Figures 5.2.2.1 and 5.2.2.2. Both of these elemental series reflect the distribution of copper, bismuth and sulfur in corresponding regions of 3-dimensional thin-film growth, platelet growth and potential particle agglomeration. The thin-film section visible in the right side of the images in Figure 5.2.2.1 corresponds to that predominantly featured in Figure 5.2.1.3, and the consistent presence of copper, bismuth and sulfur within the structure is evident.

Additionally, Figure 5.2.2.2 reflects the presence of a distribution of copper, bismuth and sulfur in region of the substrate which shows no growth (upper left of each image) apparent in the SEM micrograph. This confirms the initial seeding of the FTO coated glass substrate as discussed in Sect. 5.2.1 and suggests the potential for further growth in these regions with longer processing time within the continuous flow reactor. Visible in the bismuth series within Figure 5.2.2.2 is a notably higher concentration (pink and red) in the region of seeding as compared to growth regions (yellow and green). The potential for bismuth to be the initial seed species is suggested and may be explored in future work including substrate pretreatment.

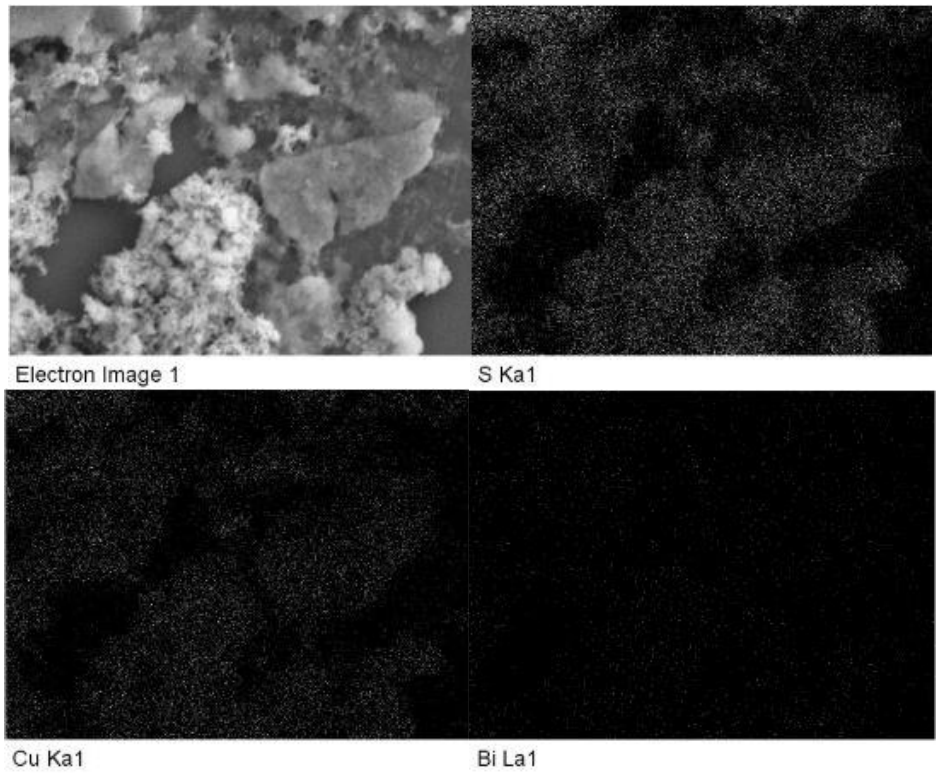

Fig. 5.2.2.1: Elemental analysis by EDX of reactor grown samples without post-processing showing copper, bismuth and sulfur in regions of 3D growth.

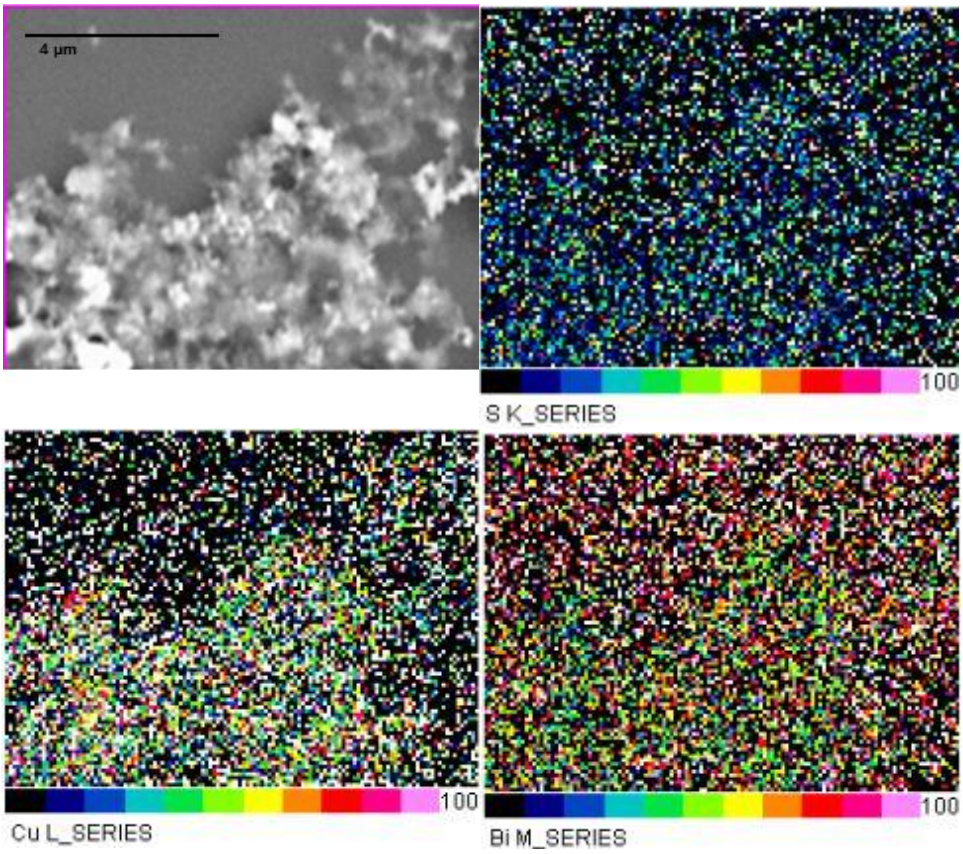

Fig. 5.2.2.2: Elemental analysis by EDX of reactor grown samples without post-processing showing copper, bismuth and sulfur in regions of 3D growth as well as initial seeding of the substrate.

Phase determination by x-ray diffraction revealed the reactor's ability to produce single phase Wittichenite growth as is evident in the collected and reference spectra shown in Figure 5.2.2.3. This experimental spectrum represents a continuous synthesis run within the reactor with no interruptions to heating or fluid flow and the substrate located on the bottom surface of the reactor.

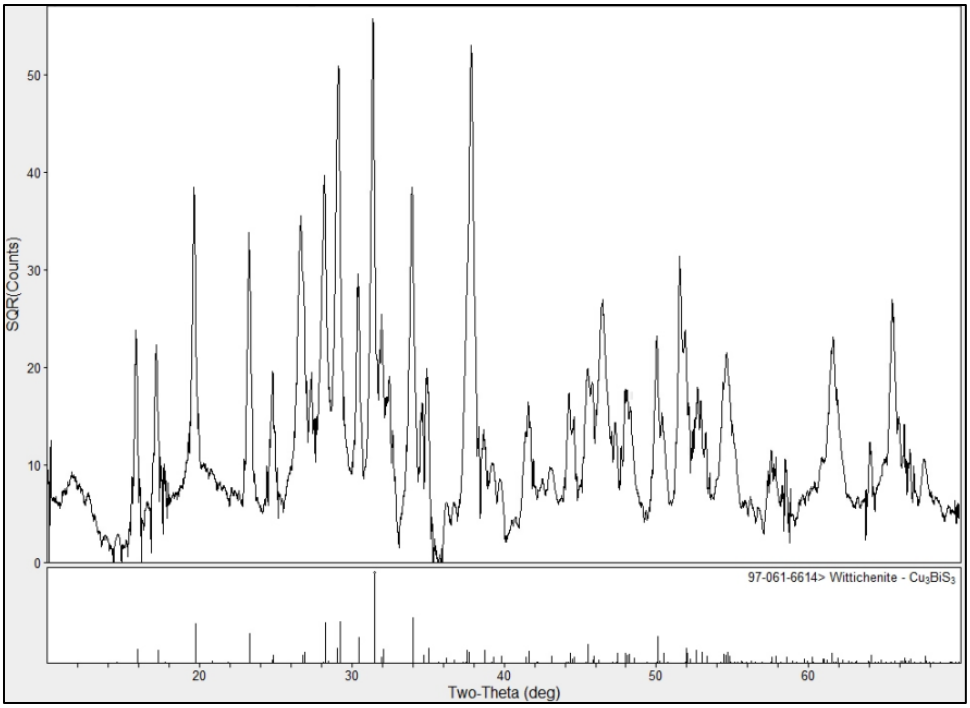

Fig. 5.2.2.3 X-Ray diffraction spectrum of reactor grown copper bismuth sulfide and reference spectrum for the same, revealing single-phase Cu_3BiS_3 (Wittichenite) product.

While the SEM observation above has indicated that the Cu_3BiS_3 nucleates on the FTO, the XRD data do not give a strong preferred growth orientation for the CBS material. If there had been preferential growth then particular Cu_3BiS_3 XRD peak intensities corresponding to select crystallographic planes would have been imbalanced significantly from what was given in the reference Wittichenite pattern, but this was not seen. The presence of agglomerated crystallites from solution having diffused/settled to the film surface with random orientation would contribute to the observation of non-preferential growth.

Film deposition was also performed with the substrate inverted within the reactor to reduce the settling of agglomerated solution-born crystallites toward the film surface. The x-ray diffraction spectrum in Fig. 5.2.2.4 represents such a synthesized film, and as the presence of obscuring particulate was reduced the underlying FTO substrate diffraction peaks are of greater intensity and denoted within the figure.

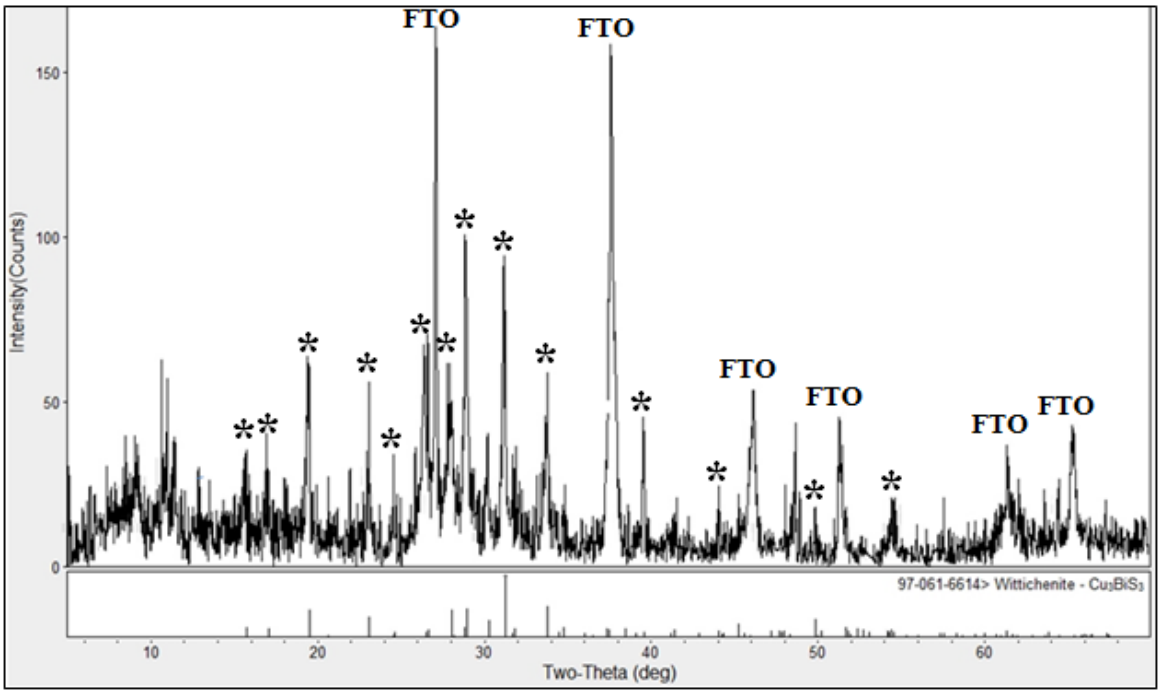

Fig. 5.2.2.4 X-Ray diffraction spectrum of reactor grown copper bismuth sulfide and reference spectra for the same, revealing Cu_3BiS_3 (*) (Wittichenite) and underlying FTO substrate (FTO).

5.3 Discussion

Crystalline copper bismuth sulfide is deposited in the continuous flow micro-reactor in the desired stoichiometry (Cu_3BiS_3). A suitable substrate for deposition has also been proven with FTO coated soda-lime glass, but the microstructures produced are

as yet not device-ready and there exists the potential for phases other than Wittichenite to be synthesized. The minimization of particulate deposition effects, the prevention of additional phase formation, and the control of surface roughness by means of preferred growth models are within the scope of the flow-through reactor system going forward.

The presence of mixed pre-cursor solution in the entire reaction chamber (not just at the substrate surface) results in the precipitation and growth of Cu_3BiS_3 particles on the nanometer scale as evidenced by the particulate seen in Fig. 5.2.1.2. These nanoparticles may then either be removed from the reaction chamber by the pumped solution flow or they may settle out of solution to deposit on the substrate and copper bismuth sulfide structures already present. Minimizing the precipitation of these particles in solution is considered possible with further efforts to manage the temperature profile in the z-direction within the reactor. That is, the unreacted solution would attain a reaction temperature above 156º only at the substrate surface as described in Section 4.3. A further management of the reactor temperature profile in combination with substrate selection and/or preparation may also take advantage of the apparent preferential nucleation at the substrate surface. It may be possible to maintain the solution temperature below the reaction temperature required for homogeneous precipitation from solution and introduce a prepared substrate that nucleates growth at and only at the substrate surface. This control may be employed whether the substrate is on the bottom of the reactor or placed in an inverted position, as discussed further in Sect. 7.1.3.

The synthesis of multiple-phases within the reactor is also possible. Though our x-ray diffraction analysis did not find definite additional copper bismuth sulfide phases, the formation of at least $Cu_4Bi_4S_9$ as has been demonstrated via solvothermal

syntheses[221,222]. While the methods employed by Li, et al relied on a different solvent (chlorobenzene) and required a higher temperature (225ºC) than that attainable within our reactor and ethylene glycol combination, it is possible that localized over-pressure or L-cystine complexing mechanisms as yet not understood may lead to varying stoichiometric ratios of copper bismuth sulfide. Maintenance of the fluid temperature below that required for $Cu_4Bi_4S_9$ and other phases as well as minimization of eddies within the fluid flow profile are therefore critical in future reactor iterations.

The desired reactor product is a Cu_3BiS_3 film of maximized density and minimized surface roughness. Control over these parameters must be exercised by a model of film growth that allows for the preferential growth of certain crystallites over others as evidenced by the microstructures that developed. The growth within our system is also made more complicated by the initiation, growth, and movement of vapor bubbles as a product of the synthesis chemistry (Fig. 5.3.1), which was described in relation to the one-pot reaction developed and described in Chapter 2. In the flow-through reactor, the initiation of vapor bubbles within the solution likely occurs preferentially at the nucleation and growing crystallite sites via the same mechanism exploited in the use of boiling chips as well as through the inherent evolution of gases via the synthesis reaction. A vapor bubble is evolved as the reaction proceeds at the surface of a growing crystallite (Fig. 5.3.1, step a); the vapor bubble expands to the point of buoyant detachment from the crystallite (step b); and convective solution replacement at the surface of the crystallite occurs as the bubble exits the region (step c). The convective motion replenishes a supersaturated region immediately above the most recently expanded portion of the film, allowing a faster growth rate and eventual prominence above the average height of the

coating (steps d, e). The continued initiation, growth and exit of vapor bubbles from these sites would cause this kind of feedback-enhanced fluid convection and growth that could interfere with flat surface growth (schematic of the preferred ideal as f). In particular, the convection would bring unreacted solution to the crystallite surface at a greater rate than would occur to the more sheltered surface conformal growth sites. The resulting structure is one including regions of smooth conformal films interrupted by growth protrusions, as seen in the previous SEM micrographs.

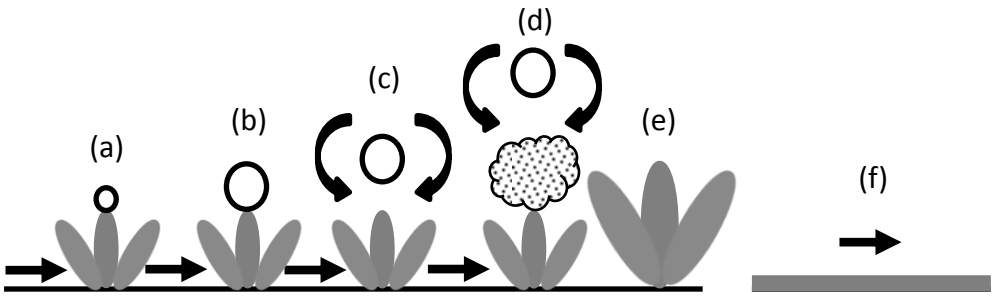

Fig. 5.3.1: Representation of preferential vapor bubble initiation (a), growth of vapor bubble (b), convective solution replacement at crystallite sites as the bubble detaches (c), supersaturated region regeneration in the bubble wake at the crystallite surface (d) driving further growth (e), versus substrate conformal sites (f).

The observed mode is in contrast to idealized growth, where a uniformly nucleated series of crystallites with sufficient spacial density to provide early contact and necking grows at a consistent rate along the substrate plane (Fig. 5.3.2). This results in a maximally dense, columnar multicrystalline film well suited for good carrier mobility in thin-film photovoltaic device P-N junctions.

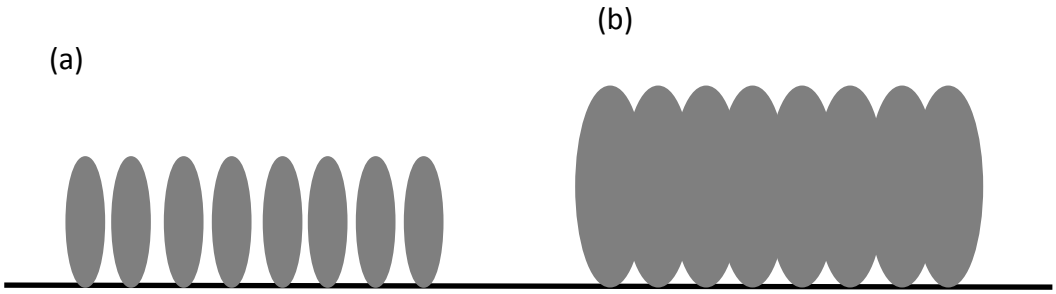

Fig. 5.3.2: Representation of ideal crystallite seeding and growth as uniformly nucleated cyrstallites (a) grow consistently resulting in columnar multicrystalline films (b).

The vapor bubble mediated growth mode instead results in selectively initiated growth which is propagated as any given crystallite protrudes above its neighbor(s), leading to uneven films (Fig. 5.3.3). It is interesting to note that even if no bubbles are generated by the precipitation process, then growth protrusions by individual particles do typically reach into the supersaturated solution further and can experience faster growth rates in a similar way.

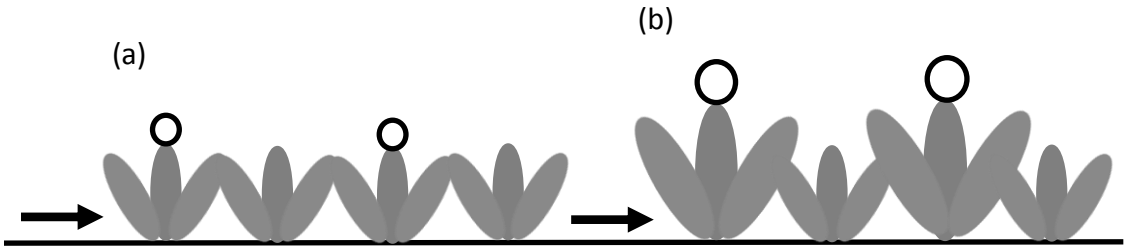

Fig. 5.3.3: Representation of non-ideal crystallite seeding and growth as uniformly nucleated crystallites may selectively initiate reactions at their surface (a) resulting in preferential growth of larger crystallites and leading to uneven films (b).

One possible control scheme implementable to alleviate uneven film growth is to maintain a temperature gradient normal to the substrate selectively providing sufficient heat to drive the synthesis reaction. If the growth rate increases with temperature (whatever the kinetic mechanism) it is possible to use this dependence to reduce the growth instabilities outlined above. Figure 5.3.4 illustrates a growth configuration with a vertical temperature gradient applied and where some surface roughness exists. If conditions are tuned properly the growth rate for the high spots (at a fluid temperature (T_2)) can be slower than the growth rate for the low spots (at a fluid temperature (T_1)). In this case the hotter (lower) regions can "catch up" with the growth that has already occurred for the grains that have protruded into the colder(higher) zone. In this way only the valleys of a growing film are promoted and prominences are retarded, driving the growth of a smooth film. This is a promising approach for the CBS materials because the one-

pot synthesis requires heating above a threshold temperature in order to drive the precipitation reaction (as discussed in Chapter 2).

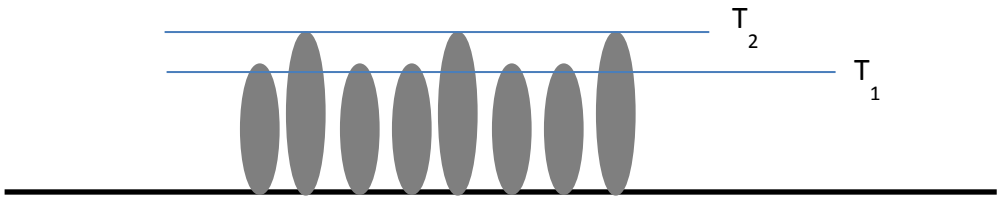

Fig. 5.3.4: Representation of potential control to alleviate uneven film growth, where a colder temperature (T_2) below the reaction temperature is maintained at the surface of the highest cystallites and a hotter temperature (T_1) above reaction temperature is maintained at the surface of the lowest crystallites; growth of a smooth film is thus driven.

5.4 Conclusion

It is evident that refinement of the reactor design and operating parameters are necessary in order to better mimic the consistent and pure synthesis enabled by the one-flask methods detailed in Chapter 2. Conditions within the flask include continuous mixing (distribution) and very rapid reaction of all pre-cursor solution. The continuous throughput requirement for improved deposition (production) speed includes the significant challenge of controlling a fluid reaction front within a constrained, heated space (reaction chamber).

Despite the challenges of transferring benchtop chemistry methods performed in traditional glassware to experimentally derived operating parameters in production-minded, prototype deposition equipment, the work here has demonstrated the ability to

deposit and grow the desired phase of copper bismuth sulfide semiconductor (Wittichenite) on an FTO coated glass substrate in a continuous flow micro-reactor. The importance of temperature and flow control within the reactor has been demonstrated, and growth models for actual and idealized films have been put forward to improve the controlled improvement of deposited film structure and roughness. Future reactor work will be required to demonstrate the viability of this p-type absorber for the implementation in thin-film photovoltaics and provide a deposition technology platform with the potential to benefit many more thin-film semiconductor deposition endeavors.

CHAPTER 6

Conclusion

The research is driven by the need for alternative global energy production. As one sector of alternative energy within the larger solar energy umbrella, photovoltaic production has been shown to provide environmentally sustainable and economically accessible means for replacing fossil fuels as our primary source for power generation. It remains the task for current and future researchers to reduce the environmental impact of new technologies while simultaneously improving the efficiency of these alternative sources. What is presented here is not a paradigm shift, but instead an investigation of how to improve existing thin-film photovoltaic technology. By reducing the cost and environmental impact of raw material sourcing, Cu_3BiS_3 is a strong candidate to pave a way for more acceptable thin-film photovoltaic absorber semiconductors.

Selection of Cu_3BiS_3 as a material of interest began with a scope of identifying alternative candidates for thin-film photovoltaic absorbers. A deep literature survey produced an array of oxides, sulfides and selenides, and the further investigation of copper sulfide (selected for its abundance and low toxicity) revealed the mineral Wittichenite (Cu_3BiS_3) stable with the inclusion of bismuth. Established synthesis methods requiring significant time and energy were the initial target for improvement,

resulting in a new environmentally friendly synthesis pathway replacing toxic reduction agents with a complexing agent and ethylene glycol solvent (Chapt. 2).

As a complexing agent, L-cystine is an abundant, natural source for the active thiol required for bismuth and copper ion complexing prior to the simultaneous breakdown at reaction temperature enabling the formation of the ternary compound. The reaction temperature required for the thiol breakdown, 158ºC, is well below previously demonstrated Cu_3BiS_3 syntheses, which at their greatest burden required up to 400ºC for up to 12 hours. The replacement of reducing agents with the thiol complexing has allowed the use of ethylene glycol as the sole solvent for dissolution of the nitrate salt precursors, resulting in an eventual production toxicity well within the bounds of even the food production industry.[13] The synthesis of Cu_3BiS_3 presented remains under consideration for a U.S. patent. The novel use of a complexing agent in the ternary compound production at low temperatures and with low toxicity solvents are the driving agents for the application.

After our bulk solution precipitation synthesis we proceeded to perform critical characterization, including using the Tauc method for band-gap determination. The Tauc analysis method is a valuable tool for extracting the bandgap of a semiconductor from UV-Vis characterization data and thereby determining the viability of a material in early development stages. As a part of the optical work we endeavored to understand more about the accuracy of the Tauc method and verify its application to polycrystalline materials (Chapt. 3). We selected the stoichiometrically simple (1:1) and oft examined zinc oxide as the commonality in our assessment with the goal of producing an evaluation

which may be extended to not just Cu_3BiS_3 but to all photoactive semiconductor analyses.

An assessment of the method with respect to consistency, accuracy, application to polycrystalline materials and potential risk of underestimation of the bandgap has been accomplished through an interrogation of zinc oxide literature. The method was found to be accurate even when applied by multiple researchers, and the precision of the method was established with the finding that among over 150 analyses, the population within one standard deviation was within 0.1 eV of the accepted bandgap. That the Tauc analyses are accurate and valid for polycrystalline zinc oxide semiconductors suggests that the analysis technique is applicable to not just the amorphous materials originally examined by Tauc et al[51], but to direct band-gap polycrystalline semiconductors as a class. Finally, a new Tauc Ratio quantification of the degree of disorder imparted by Urbach tails was presented. Using this figure of merit the potential for the distortion of an assessed bandgap was evaluated and discussed. An application of the Tauc Ratio to the previously performed Tauc analysis for flask derived Cu_3BiS_3 showed a relatively high value indicative of a larger Urbach tail and a likely larger degree of disorder within the synthesized samples. Future application of this optical metric may be used as feedback for synthesis refinement.

After the chemistry was developed, effort was aimed at designing and refining a continuous throughput micro-reactor to attempt the production of semi-conducting thin-films of this material. While the biological sciences are skilled in the art of micro-reactors, the application to semiconductor and specifically alternative energy materials is an important step forward. Flow, temperature and substrate characteristics have been

considered and a working prototype built for research. Initial films have been grown indicating the potential of this path, but also illustrating the complexity of coating growth from these solutions. Future directions of investigation have been suggested and the path for continuous advancement within the research group has been established based on this new platform of deposition.

This research seeks to capitalize on a specific novel chemistry for photoactive semiconductor synthesis by examining the opportunity for improvement within current thin-film solar cell architectures. This has been in consideration of minimizing negative environmental implications in regards to material sourcing and refining, to solvents and reducing agents employed, to energy requirements sufficient to drive the necessary reactions, and to the eventual end of life disposal or recycling of the materials involved. Our demonstration of the surface growth of Cu_3BiS_3 brings this material one step closer to establishing it as a novel and sustainable solar cell material for the future.

CHAPTER 7

Proposal for Future Work

The research undertaken within this thesis work was a starting point for thin-film photovoltaic work within the research group, for the investigation of a novel and potentially environmentally beneficial semiconductor (Cu_3BiS_3), and for the further development of continuous throughput reactors for the deposition of semiconducting thin-films. While the effort within this dissertation has been fruitful, the potential exists for refinement of the chemistry and components employed, which could help improve the microstructure of coatings that might be made in the future.

7.1 Reactor and Reaction Refinement

With regards to the reactor as built and used in this research, two fundamental refinements include the reliable outgassing of a reaction-byproducts, thought to be hydrogen sulfide, and the sufficiently powerful and controllable zone heating of the reactor itself. Modelling of thin-film growth revealed the opportunity for substrate selection and preparation to improve the nucleation and initial growth within the chamber. And, the chemistry established in the L-cystine enabled copper bismuth sulfide synthesis development (Chapter 2) should also allow for the introduction of an array of dopants for the tuning of relevant electronic and optical properties.

7.1.1 Outgassing of Reaction By-products

The copper bismuth sulfide synthesis reaction described here always involved the production of gaseous byproducts whether carried out in the flask reaction or in the flow-through-reactor. This outgassing was initially thought to be hydrogen sulfide based on the observation that the in-flask solution stoichiometry provides a double excess of sulfur; it was inferred that sulfur from the disulfide bond of the L-cystine complexing molecule was partly incorporated into the Cu_3BiS_3 and partly lost as when the disulfide bond is broken at reaction temperature (~156ºC). The initial two-neck flask synthesis was unaffected by the gas production, and the byproduct escaped to atmosphere through the reflux tube. When the reaction was contained within the continuous throughput reactor, the gas was restricted from escape by fluid movement through the outlet tube. The result was chaotic flow within the reactor, including collection of bubbles preventing even growth, both undesirable attributes for continuous and smooth semiconductor deposition. Two paths for remedy of the presence of the hydrogen sulfide gas outgassing are suggested. Firstly, one may find a chemical pathway to secure the thiol and prevent the production of a gaseous byproduct. Secondly, a suitable outgassing valve properly placed in the reactor lid may alleviate the problem allowing any gaseous by-products to exit.

7.1.2 Refinement of Zone Heating

The ideal reactor configuration as proposed includes the creation of two distinct zones of heating along the reactant fluid path within the continuous flow reactor. These

two zones are also ideally maintained at different temperatures during the reaction to create a temperature gradient along the flow direction as well as normal to the flow in the z-direction. The heaters used in the present work were not powerful enough to deliver the desired local gradient resulting in the necessity for additional heating boost by means of an ordinary laboratory heating platen beneath the reactor. This resulted in a reduction of the gradient that we could test. One large area available for further work, then, is the refinement of the heating apparatus and thermal gradient control. Ideally a plurality of heaters capable of producing greater power density yet still within control of a variable DC power output would be sourced and implemented within an adapted reactor design in order to produce the heating zones as outlined.

7.1.3 Substrate Selection and Preparation

The nucleation and initial growth of crystallites on the substrate as observed and detailed in Chapter 5 was far from smooth and controlled and certainly not ready for device implementation. The microstructures may be improved by future substrate selection and preparation, especially in ways that might promote preferred nucleation at the surface. Various fluid temperature profile control schemes were outlined in order to provide favorable growth conditions (e.g. temperature greater than the reaction threshold) only at the substrate surface and subsequently the growing thin-film surface in order to eliminate the spontaneous nucleation of crystallites within the fluid medium. The problem of nucleating, agglomerating and diffusing crystallites from within the fluid medium to the surface may instead be overcome by a catalyzing substrate that provides for crystallite nucleation below the previously established reaction temperature threshold

(158ºC). In this way the fluid may be kept below the reaction temperature threshold and nucleation would only occur at the preferred substrate surface. Initial, homogenous seeding of the substrate with previously synthesized nano-crystallites may also be employed to drive preferential growth at the surface while similarly maintaining a depressed fluid temperature.

7.1.4 Introduction of Doping to the Established Chemistry

Copper bismuth sulfide researchers have yet to investigate any potential dopants that would be necessary for good device implementation. The opportunity is evident to pursue this path, particularly considering the synthesis system available to the researcher. The ethylene glycol solvent has already proven valuable, enabling the use of nitrate salt precursors in replacement of previously employed chlorides. The availability of many possible dopant elements in nitrates as well as many in acetates should allow for simple introduction during the pre-complexing stages and have high probability of fabricating controlled doped material.

7.2 Successive Device Fabrication

The development and construction of a fully operational photovoltaic Cu_3BiS_3 cell is being attempted by select groups in South America and Asia. Device architecture has been proposed to mimic the commercially available CdTe and CIGS configurations, wherein a metal sputtered back soda-lime glass is followed by a naturally p-type Cu_3BiS_3 layer, a potentially necessary buffer layer of CdS deposited by chemical bath deposition

(CBD), an n-type ZnO deposited by sol-gel spin-coating, and finally a commercially sourced FTO or ITO coated front soda-lime glass platen (Figure 7.2.1).

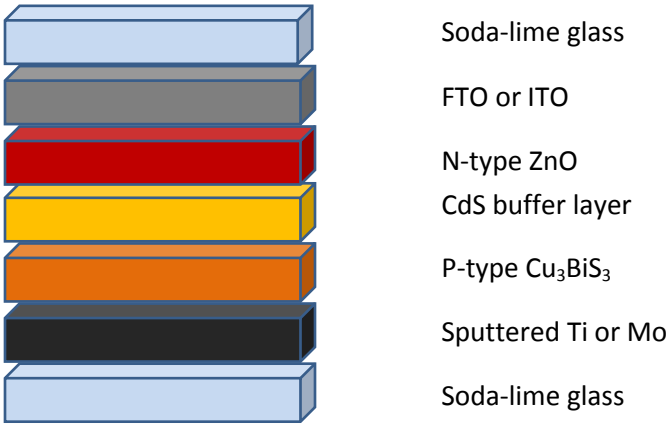

Fig. 7.2.1: Suggested thin-film photovoltaic cell architecture for incorporation of novel Cu_3BiS_3 p-type semiconductor absorber

While this research group has in the past demonstrated some expertise in sputtered glass back reflectors and individually deposited CdS and ZnO semiconductors, a functional Cu_3BiS_3 absorber layer has yet to be consistently formed and the successive deposition of all active layers in one stack is also unproven. The collaboration of the entire group, concentrating on each arena, has the potential to produce the first working Cu_3BiS_3 based thin-film photovoltaic cell.

7.3 Inks

There also exists the potential to develop printable inks from the nanoparticles grown in the previously used three neck flask synthesis arrangement. The collection,

solvent washing and eventual suspension in a medium of appropriate viscosity for the particular printing process are considered viable steps for cost-reductions in thin-film solar cell production. Whether intended for precision inkjet, drawdown rods or other production proven printing methods, the development of an ink with the correct particle concentration, particle size distribution, particle morphology, medium viscosity, and medium volatility is a complex interdependency. The aim of this thesis work was in fact to provide a Cu_3BiS_3 synthesis and a film deposition method via reactor, but the opportunity exists for eventual development of a printable nano-particle ink.

7.4 Conclusions

Potential paths for improvement and advancement of both the synthesis pathway and the continuous throughput micro-reactor deposition of Cu_3BiS_3 described above are suggested as immediate directions for furthering this research. Refinement of the synthesis to control or even eliminate gaseous byproducts, incorporating transport enhancing dopants in the semiconductor, producing functionalized substrates, and engineering future reactor generations all show great potential for productive work. Additionally, the opportunities for parlaying this body of work to other solution based semiconductor syntheses and the eventual deposition of such are present. It is hoped that future semiconductor development includes these advancements so that we may profitably reduce environmental impacts of photovoltaic production.

REFERENCES

1. Maantay, J. & Becker, S. The health impacts of global climate change: A geographic perspective. *Appl. Geogr.* **33,** 1–3 (2012).

2. Potocnik, J. Renewable Energy Sources and the Realities of Setting an Energy Agenda. *Science (80-.).* **315,** 810 (2007).

3. Service, R. F. Is It Time to Shoot for the Sun? *Science (80-.).* **309,** 548 (2005).

4. Fry, M., Hoeinghaus, D. J., Ponette-Gonzalez, A. G., Thompson, R. & Point, T. W. La. Fracking vs Faucets: Balancing Engergy Needs and Water Sustainability at Urban Frontiers. *Environ. Sci. Technol.* **46,** 7444–7445 (2012).

5. *State of the Climate: Global Analysis for October 2013*. (2013). at <retrieved on November 24, 2013 from http://www.ncdc.noaa.gov/sotc/global/>

6. Kalyanasundaram, K. *Dye sensitized Solar Cells*. (CRC Press: Florida, 2010).

7. Schiermeier, Q., Tollefson, J., Scully, T., Witze, A. & Morton, O. Energy alternatives: Electricity without carbon. *Nature* **454,** 816–823 (2008).

8. Benson, S. & Orr, F. M. Sustainability and Energy Conversions. *MRS Bull.* **33,** 297–302 (2008).

9. Dale, P., Loken, A., Peter, L. & Scragg, J. Towards Sustainable Photovoltaic Solar Energy Conversion: Studies Of New Absorber Materials. *ECS Trans.* **19,** 179–187 (2009).

10. Hossain, M. I. & Alharbi, F. H. Recent advances in alternative material photovoltaics. *Mater. Technol.* **28,** 88–97 (2013).

11. Viezbicke, B. D. & Birnie III, D. P. Solvothermal Synthesis of Cu3BiS3 Enabled by Precursor Complexing. *Sustain. Chem. Eng.* **1,** 306–308 (2013).

12. Fisher Scientific. Ethylene Glycol MSDS Sheet. (2013). at <http://fscimage.fishersci.com/msds/09400.htm>

13. Dilger, R., Toue, S., Takeshi, K., Ryosei, S. & baker, D. Excess Dietary L-Cysteine , but Not L-Cystine , Is Lethal for Chicks but Not for Rats or Pigs. *Science (80-.).* **137,** 331 (2007).

14. NREL. Best Research-Cell Efficiencies. (2013). at <http://www.nrel.gov/ncpv/images/efficiency_chart.jpg>

15. NREL. CdTe Photovoltaic Cell Graphic. (2013). at <http://www.nrel.gov/pv/images/graphic_cdte_cell.jpg>

16. Hodes, G. *Chemical solution deposition of semiconductor films*. 306 (Marcel Dekker, 2002). at <http://books.google.com/books?hl=en&lr=&id=PjmQnVX4OmUC&oi=fnd&pg=PR3&dq=Chemical+Solution+Deposition+of+Semiconductor+Films&ots=lNdtwqJb4K&sig=UaFjWHVItsF5kyDsouGSPul4Cs4>

17. Poortmans, J. & Arkhipov, V. *Thin Film Solar Cells: Fabrication, Characterization and Applications*. 265 (John Wiley & Sons, Inc., 2007).

18. Kim, H. C., Fthenakis, V. & Choi, J.-K. Life Cycle Greenhouse Gas Emissions of Thin-film Photovoltaic Electricity Generation. *J. Ind. Ecol.* **16,** S110–S121 (2012).

19. Kocman, V. & Nuffield, E. W. The Crystal Structure of Wittichenite, Cu3BiS3. *Acta Crystallogr. B* **B29,** 2528–2535 (1973).

20. Sugaki, A. & Shima, H. *Phase Relations of the Cu2S-Bi2S3 System*. 45–70 (1972).

21. TOMEOKA, K., OHMASA, M. & SADANAGA, R. Crystal chemical studies on some compounds in the Cu 2 S–Bi 2 S 3 system. *Mineral. J.* **10,** 57–70 (1980).

22. Colombara, D. *et al.* Formation of Cu3BiS3 thin films via sulfurization of Bi–Cu metal precursors. *Thin Solid Films* **520,** 5165–5171 (2012).

23. Hu, H., Gomez-Daza, O. & Nair, P. K. Screen-printed Cu3BiS3-polyacrylic acid composite coatings. *J. Mater. Res.* **13,** 2453–2456 (1998).

24. Estrella, V., Nair, M. & Nair, P. Semiconducting Cu3BiS3 thin films formed by the solid-state reaction of CuS and bismuth thin films. *Semicond. Sci. Technol.* **18,** 190 (2003).

25. Kumar, M. & Persson, C. Cu3BiS3 as a potential photovoltaic absorber with high optical efficiency. *Appl. Phys. Lett.* **102,** 062109 (2013).

26. Colombara, D., Peter, L. M., Rogers, K. D. & Hutchings, K. Thermochemical and kinetic aspects of the sulfurization of Cu–Sb and Cu–Bi thin films. *J. Solid State Chem.* **186,** 36–46 (2012).

27. Gerein, N. J. & Haber, J. A. One-Step Synthesis and Optical and Electrical Properties of Thin Film Cu3BiS3 for Use as a Solar Absorber in Photovoltaic Devices. *Chem. Mater.* **18,** 6297–6302 (2006).

28. Maiello, P., Zoppi, G., Miles, R. W., Pearsall, N. & Forbes, I. Investigations of Ternary Cu3BiS3 Thin Films as Absorber in Photovoltaic Devices. in *7th Photovolt. Sci. Appl. Technol. Conf.* (2011).

29. Mesa, F. *et al.* Junction formation of Cu(3)BiS(3) investigated by Kelvin probe force microscopy and surface photovoltage measurements. *Beilstein J. Nanotechnol.* **3,** 277–84 (2012).

30. Mesa, F., Dussan, A. & Gordillo, G. Study of the growth process and optoelectrical properties of nanocrystalline Cu 3 BiS 3 thin films. *Phys. Status Solidi* **7,** 917–920 (2010).

31. Mesa, F. & Gordillo, G. Effect of preparation conditions on the properties of Cu 3 BiS 3 thin films grown by a two – step process. *J. Phys. Conf. Ser.* **167,** 012019 (2009).

32. Murali, B., Venugopal, R., Chandan, K. G. & Krupanidhi, S. B. Solvothermal Synthesis, Structural and Optical Properties of Phase-Pure Cu₃BiS₃ Nano-Powders Exhibiting Near-IR Photodetection. *Adv. Sci. Eng. Med.* **4,** 89–95 (2012).

33. Murali, B. & Krupanidhi, S. B. Tailoring the Band Gap and Transport Properties of Cu₃BiS₃ Nanopowders for Photodetector Applications. *J. Nanosci. Nanotechnol.* **13,** 3901–3909 (2013).

34. Tablero, C. Photovoltaic application of O-doped Wittichenite- Cu 3 BiS 3 : from microscopic properties to maximum ef fi ciencies. 894–899 (2013). doi:10.1002/pip

35. Zeng, Y. *et al.* Facile synthesis of flower-like Cu3BiS3 hierarchical nanostructures and their electrochemical properties for lithium-ion batteries. *CrystEngComm* **14,** 550–554 (2012).

36. Nair, P. K. *et al.* Formation of p-type Cu2BiS3 absorber thin films by annealing chemically deposited Bi2S3 – CuS thin films. *J. Mater. Res.* **12,** 651–656 (1997).

37. Gerein, N. J. & Haber, J. A. Synthesis of Cu3BiS3 thin films by heating metal and metal sulfide precursor films under hydrogen sulfide. *Chem. Mater.* **18,** 6289–6296 (2006).

38. Mesa, F., Gordillo, G., Ellmer, K. & Baier, R. Transient surface photovoltage of p-type Cu3BiS3. *Appl. Phys. Lett.* **96,** (2010).

39. Mesa, F. *et al.* Transient surface photovoltage of p-type Cu3BiS3. *Appl. Phys. Lett.* **96,** 082113 (2010).

40. Mesa, F., Dussan, a. & Gordillo, G. Evidence of trapping levels and photoelectric properties of Cu3BiS3 thin films. *Phys. B Condens. Matter* **404,** 5227–5230 (2009).

41. Chen, D. *et al.* Microwave synthesis of AgBiS2 dendrites in aqueous solution. *Inorg. Chem. Commun.* **6,** 710–712 (2003).

42. Hu, J., Deng, B., Wang, C., Tang, K. & Qian, Y. Convenient hydrothermal decomposition process for preparation of nanocrystalline mineral Cu3BiS3 and Pb1−xBi2x/3S. *Mater. Chem. Phys.* **78,** 650–654 (2003).

43. Xinyu, Y. *et al.* l-Cystine-assisted growth of Sb2S3 nanoribbons via solvothermal route. *Mater. Chem. Phys.* **118,** 432–437 (2009).

44. Chen, D. *et al.* The synthesis of Cu3BiS3 nanorods via a simple ethanol-thermal route. *J. Cryst. Growth* **253,** 512–516 (2003).

45. Shen, G., Chen, D., Tang, K. & Qian, Y. Synthesis of ternary sulfides Cu(Ag)–Bi–S coral-shaped crystals from single-source precursors. *J. Cryst. Growth* **257,** 293–296 (2003).

46. Jiasong, Z. *et al.* A simple L-cystine-assisted solvothermal approach to Cu3SbS3 nanorods. *Mater. Lett.* **64,** 1499–1502 (2010).

47. Aup-Ngoen, K., Thongtem, S. & Thongtem, T. Cyclic microwave-assisted synthesis of Cu3BiS3 dendrites using l-cysteine as a sulfur source and complexing agent. *Mater. Lett.* **65,** 442–445 (2011).

48. Scaldaferri, M. C. L. & Pimentel, A. S. Theoretical study of the reaction of hydrogen sulfide with nitrate radical. *Chem. Phys. Lett.* **470,** 203–209 (2009).

49. *Amorphous and Liquid Semiconductor*. 159 (Plenum Press, 1974).

50. Bierman, M. J., Lau, Y. K. ., Kvit, A. V., Schmitt, A. L. & Jin, S. Dislocation-Driven Nanowire Growth and Eshelby Twist. *Science (80-.).* **1060,** (2013).

51. Tauc, J., Grigorovici, R. & Vancu, A. Optical Properties and Electronic Structure of Amorphous Germanium. *Phys. Status Solidi* **15,** 627–637 (1966).

52. Ábrahám, N. & Dékány, I. Size-dependent photoluminescence properties of bare ZnO and polyethylene imine stabilized ZnO nanoparticles and their Langmuir–Blodgett films. *Colloids Surfaces A Physicochem. Eng. Asp.* **364,** 26–33 (2010).

53. Absalan, H. & Ghodsi, F. E. Comparative study of ZnO thin films prepared by different sol-gel route. *Iran. J. Phys. …* **118,** 659–664 (2012).

54. Abu El-Fadl, A., El-Maghraby, E. M. & Mohamad, G. A. Influence of gamma radiation on the absorption spectra and optical energy gap of Li- doped ZnO thin films. *Cryst. Res. Technol.* **39,** 143–150 (2004).

55. Abu EL-Fadl, A., EL-Maghraby, E. M. & Yamazaki, T. Optical investigations on the existence of phase transition in ZnO:Li thin films prepared by DC sputtering method. *Cryst. Res. Technol.* **43,** 302–307 (2008).

56. Ahn, S., Kwon, T.-G. & Lee, S.-Y. Synthesis of zinc tin oxide (ZTO) nanocrystallites at room temperature through association with peptide-containing bolaamphiphile molecules. *J. Colloid Interface Sci.* **362,** 292–9 (2011).

57. Al-Kuhaili, M. F., Durrani, S. M. a. & Bakhtiari, I. a. Carbon monoxide gas-sensing properties of CeO2–ZnO thin films. *Appl. Surf. Sci.* **255,** 3033–3039 (2008).

58. Bandyopadhyay, S., Paul, G. K. & Sen, S. K. Study of optical properties of some sol–gel derived films of ZnO. *Sol. Energy Mater. Sol. Cells* **71,** 103–113 (2002).

59. Baviskar, P. K., Tan, W., Zhang, J. & Sankapal, B. R. Wet chemical synthesis of ZnO thin films and sensitization to light with N3 dye for solar cell application. *J. Phys. D. Appl. Phys.* **42,** 125108 (2009).

60. Baviskar, P. K., Nikam, P. R., Gargote, S. S., Ennaoui, A. & Sankapal, B. R. Controlled synthesis of ZnO nanostructures with assorted morphologies via simple solution chemistry. *J. Alloys Compd.* **551,** 233–242 (2013).

61. Bilgin, V. Preparation and Characterization of Ultrasonically Sprayed Zinc Oxide Thin Films Doped with Lithium. *J. Electron. Mater.* **38,** 1969–1978 (2009).

62. Biswas, P., Kundu, S., Banerji, P. & Bhunia, S. Super rapid response of humidity sensor based on MOCVD grown ZnO nanotips array. *Sensors Actuators B Chem.* **178,** 331–338 (2013).

63. Bojorge, C. D. *et al.* Synthesis and optical characterization of ZnO and ZnO:Al nanocrystalline films obtained by the sol-gel dip-coating process. *J. Mater. Sci. Mater. Electron.* **18,** 1119–1125 (2007).

64. Bojorge, C. D. *et al.* Zinc-oxide nanowires electrochemically grown onto sol-gel spin-coated seed layers. *Phys. Status Solidi* **208,** 1662–1669 (2011).

65. Bouznit, Y., Beggah, Y. & Ynineb, F. Sprayed lanthanum doped zinc oxide thin films. *Appl. Surf. Sci.* **258,** 2967–2971 (2012).

66. Bruncko, J. *et al.* Annealing and recrystallization of amorphous ZnO thin films deposited under cryogenic conditions by pulsed laser deposition. *Thin Solid Films* **520,** 866–870 (2011).

67. Buchholz, D. B., Liu, J., Marks, T. J., Zhang, M. & Chang, R. P. H. Control and characterization of the structural, electrical, and optical properties of amorphous zinc-indium-tin oxide thin films. *ACS Appl. Mater. Interfaces* **1,** 2147–53 (2009).

68. Caglar, M., Ilican, S., Caglar, Y. & Yakuphanoglu, F. The effects of Al doping on the optical constants of ZnO thin films prepared by spray pyrolysis method. *J. Mater. Sci. Mater. Electron.* **19,** 704–708 (2007).

69. Caglar, M., Ilican, S., Caglar, Y. & Yakuphanoglu, F. Electrical conductivity and optical properties of ZnO nanostructured thin film. *Appl. Surf. Sci.* **255,** 4491–4496 (2009).

70. Cao, F., Wang, Y. & Liu, D. Influence of O2/Ar ratio on properties of transparent conductive tantalum-doped ZnO films. *Electron. Lett.* **45,** 324 (2009).

71. Chan y Díaz, E., Duarte-Moller, a., Camacho, J. M. & Castro-Rodríguez, R. SnO2 thin films grown by pulsed Nd:YAG laser deposition. *Appl. Phys. A* **106,** 619–624 (2011).

72. Chand, P., Gaur, A. & Kumar, A. Structural and optical properties of ZnO nanoparticles synthesized at different pH values. *J. Alloys Compd.* **539,** 174–178 (2012).

73. Chawla, A. K., Kaur, D. & Chandra, R. Structural and optical characterization of ZnO nanocrystalline films deposited by sputtering. *Opt. Mater. (Amst).* **29,** 995–998 (2007).

74. Chen, J., Deng, H., Li, N., Tian, Y. & Ji, H. Realization of nonpolar a-plane ZnO films on r-plane sapphire substrates using a simple single-source chemical vapor deposition. *Mater. Lett.* **65,** 716–718 (2011).

75. Choi, S. Y. *et al.* Electrical and optical properties of ZnO films deposited by ECR-PECVD. *Phys. Status Solidi* **203,** R73–R75 (2006).

76. Chouikh, F., Beggah, Y. & Aida, M. S. Optical and electrical properties of Bi doped ZnO thin films deposited by ultrasonic spray pyrolysis. *J. Mater. Sci. Mater. Electron.* **22,** 499–505 (2010).

77. Craciun, V., Elders, J., Gardeniers, J. G. E. & Boyd, I. W. Characteristics of high quality ZnO thin films deposited by pulsed laser deposition. *Appl. Phys. Lett.* **65,** 2963 (1994).

78. Craciun, V., Craciun, D., Bunescu, M. ., Dabu, R. & Boyd, I. . Growth of highly transparent oxide layers by pulsed laser deposition: reduction of droplet density. *Appl. Surf. Sci.* **109-110,** 354–358 (1997).

79. Dakhel, A. A. Nanocrystalline Pr-doped ZnO insulator for metal–insulator–Si Schottky diodes. *J. Cryst. Growth* **311,** 4183–4187 (2009).

80. Dekkers, M., Rijnders, G. & Blank, D. H. a. ZnIr2O4, a p-type transparent oxide semiconductor in the class of spinel zinc-d6-transition metal oxide. *Appl. Phys. Lett.* **90,** 021903 (2007).

81. Di Trolio, A., Bauer, E. M., Scavia, G. & Veroli, C. Blueshift of optical band gap in c-axis oriented and conducting Al-doped ZnO thin films. *J. Appl. Phys.* **105,** 113109 (2009).

82. Dimitriev, Y., Gancheva, M. & Iordanova, R. Effects of the mechanical activation of zinc carbonate hydroxide on the formation and properties of zinc oxides. *J. Alloys Compd.* **519,** 161–166 (2012).

83. Eita, M., Wågberg, L. & Muhammed, M. Spin-Assisted Multilayers of Poly(methyl methacrylate) and Zinc Oxide Quantum Dots for Ultraviolet-Blocking Applications. *ACS Appl. Mater. Interfaces* **4,** 2920–2925 (2012).

84. Faraj, M. G. & Ibrahim, K. Optical and Structural Properties of Thermally Evaporated Zinc Oxide Thin Films on Polyethylene Terephthalate Substrates. *Int. J. Polym. Sci.* **2011,** 1–4 (2011).

85. Franklin, J. B. *et al.* Optimised pulsed laser deposition of ZnO thin films on transparent conducting substrates. *J. Mater. Chem.* **21,** 8178 (2011).

86. Ganesh, I., Sekhar, P. S. C., Padmanabham, G. & Sundararajan, G. Influence of Li-doping on structural characteristics and photocatalytic activity of ZnO nano-powder formed in a novel solution pyro-hydrolysis route. *Appl. Surf. Sci.* **259,** 524–537 (2012).

87. Gulino, A., Lupo, F. & Fragalà, M. Substrate-free, self-standing ZnO thin films. *J. Phys. Chem. …* **3,** 13869–13872 (2008).

88. Gurav, K. V., Fulari, V. J., Patil, U. M., Lokhande, C. D. & Joo, O.-S. Room temperature soft chemical route for nanofibrous wurtzite ZnO thin film synthesis. *Appl. Surf. Sci.* **256,** 2680–2685 (2010).

89. Hammarberg, E., Prodi-Schwab, A. & Feldmann, C. Microwave-assisted polyol synthesis of aluminium- and indium-doped ZnO nanocrystals. *J. Colloid Interface Sci.* **334,** 29–36 (2009).

90. Hammouda, a., Canizarès, a., Simon, P., Boughalout, a. & Kechouane, M. Improving the sensitivity of Raman signal of ZnO thin films deposited on silicon substrate. *Vib. Spectrosc.* **62,** 217–221 (2012).

91. Hantehzadeh, M. R., Salavati Dezfooli, P. & Hoseini, S. a. Effect of O2/Ar Mixture on the Structural and Optical Properties of ZnO Thin Films Fabricated by DC Cylindrical Magnetron Sputtering. *J. Fusion Energy* **31,** 298–303 (2011).

92. He, R. & Tsuzuki, T. Low-Temperature Solvothermal Synthesis of ZnO Quantum Dots. *J. Am. Ceram. Soc.* **93,** 2281–2285 (2010).

93. Ho, Y.-S. & Lee, K.-Y. Fabrication of highly oriented (002) ZnO film on glass by sol–gel method. *Thin Solid Films* **519,** 1431–1434 (2010).

94. Hong, R., Shao, J., He, H. & Fan, Z. Influence of buffer layer thickness on the structure and optical properties of ZnO thin films. *Appl. Surf. Sci.* **252,** 2888–2893 (2006).

95. Hsu, J.-C., Lin, Y.-H., Wang, P. W. & Chen, Y.-Y. Spectroscopic ellipsometry studies on various zinc oxide films deposited by ion beam sputtering at room temperature. *Appl. Opt.* **51,** 1209–15 (2012).

96. Hu, Y. M. *et al.* The morphology and optical properties of Cr-doped ZnO films grown using the magnetron co-sputtering method. *Appl. Surf. Sci.* **254,** 3873–3878 (2008).

97. Huang, C. *et al.* Effects of hydrogen annealing on the structural, optical and electrical properties of indium-doped zinc oxide films. *J. Mater. Sci. Mater. Electron.* **21,** 1221–1227 (2010).

98. Ilican, S., Caglar, Y. & Caglar, M. Preparation and characterization of ZnO thin films deposited by sol-gel spin coating method. *J. Optoelectron Adv. Mater* **10,** 2578–2583 (2008).

99. Ilican, S., Caglar, M. & Caglar, Y. Sn doping effects on the electro-optical properties of sol gel derived transparent ZnO films. *Appl. Surf. Sci.* **256,** 7204–7210 (2010).

100. Ilican, S., Caglar, Y., Caglar, M. & Yakuphanoglu, F. Structural, optical and electrical properties of F-doped ZnO nanorod semiconductor thin films deposited by sol–gel process. *Appl. Surf. Sci.* **255,** 2353–2359 (2008).

101. Jia, J., Takasaki, A., Oka, N. & Shigesato, Y. Experimental observation on the Fermi level shift in polycrystalline Al-doped ZnO films. *J. Appl. Phys.* **112,** 013718 (2012).

102. Ju, J., Wu, X. & Zhuge, L. Study on the Structure and Optical Properties of Zn1-xCrxO Films by RF Magnetron Sputtering Technique. *Int. J. Mod. Phys. B* **22,** 5279–5287 (2008).

103. Kamiya, T. *et al.* Electrical Properties and Structure of p-Type Amorphous Oxide SemiconductorxZnO·Rh2O3. *Adv. Funct. Mater.* **15,** 968–974 (2005).

104. Kang, D. *et al.* Effect of Ga⁄In ratio on the optical and electrical properties of GaInZnO thin films grown on SiO[sub 2]⁄Si substrates. *Appl. Phys. Lett.* **91,** 091910 (2007).

105. Karamat, S. *et al.* Structural, optical and magnetic properties of (ZnO)1−x(MnO2)x thin films deposited at room temperature. *Appl. Surf. Sci.* **254,** 7285–7289 (2008).

106. Karmakar, R., Neogi, S. K., Banerjee, A. & Bandyopadhyay, S. Structural; morphological; optical and magnetic properties of Mn doped ferromagnetic ZnO thin film. *Appl. Surf. Sci.* **263,** 671–677 (2012).

107. Kaur, R., Singh, a. V. & Mehra, R. M. Physical properties of natively textured yttrium doped zinc oxide films by sol-gel. *J. Mater. Sci. Mater. Electron.* **16,** 649–655 (2005).

108. Kavak, H., Senadım Tuzemen, E., Ozbayraktar, L. N. & Esen, R. Optical and photoconductivity properties of ZnO thin films grown by pulsed filtered cathodic vacuum arc deposition. *Vacuum* **83,** 540–543 (2008).

109. Kim, H. *et al.* Pulsed laser deposition of Zr–N codoped p-type ZnO thin films. *Appl. Phys. A* **93,** 593–598 (2008).

110. Kim, H.-R. *et al.* Effects of Ga Concentration on Electrical and Physical Properties of Amorphous Ga-Zn-Sn-O Semiconductor Thin Films. *Electrochem. Solid-State Lett.* **14,** H411 (2011).

111. Kim, Y. *et al.* Optical and electronic properties of post-annealed ZnO:Al thin films. *Appl. Phys. Lett.* **96,** 171902 (2010).

112. Krithiga, R. & Chandrasekaran, G. Synthesis, strucutral and optical properties of vanadium doped zinc oxide nanograins. *J. Cryst. Growth* **311,** 4610–4614 (2009).

113. Krithiga, R. & Chandrasekaran, G. Ferromagnetic signature in nanoparticles of diluted magnetic semiconductors of ZnO:V. *J. Mater. Sci. Mater. Electron.* **22,** 1229–1233 (2011).

114. Kukreja, L. ., Barik, S. & Misra, P. Variable band gap ZnO nanostructures grown by pulsed laser deposition. *J. Cryst. Growth* **268,** 531–535 (2004).

115. Kulyk, B. *et al.* Structural Properties and Temperature Behaviour of Optical Absorption Edge in Polycrystalline ZnO:X (Cu,Ag) Films. *Acta Phys. Pol. A* **123,** 92 (2013).

116. Kumar, B. R. & Rao, T. S. Investigations on opto-electronical properties of DC reactive magnetron sputtered zinc aluminum oxide thin films annealed at different temperatures. *Appl. Surf. Sci.* **265,** 169–175 (2013).

117. Kumar, S. & Sahare, P. D. Observation of band gap and surface defects of ZnO nanoparticles synthesized via hydrothermal route at different reaction temperature. *Opt. Commun.* **285,** 5210–5216 (2012).

118. Li, S. Y. Field emission and photofluorescent characteristics of zinc oxide nanowires synthesized by a metal catalyzed vapor-liquid-solid process. *J. Appl. Phys.* **95,** 3711 (2004).

119. Li, Z. Q., Zhang, D. X. & Lin, J. J. Optical and electrical transport properties of facing-target sputtered Al doped ZnO transparent film. *J. Appl. Phys.* **99,** 124906 (2006).

120. Li, Z. W., Gao, W. & Reeves, R. J. Zinc oxide films by thermal oxidation of zinc thin films. *Surf. Coatings Technol.* **198,** 319–323 (2005).

121. Lien, S.-T. *et al.* Atmospheric pressure plasma jet annealed ZnO films for MgZnO/ZnO heterojunctions. *J. Phys. D. Appl. Phys.* **46,** 075202 (2013).

122. Lin, W., Ma, R., Shao, W. & Liu, B. Structural, electrical and optical properties of Gd doped and undoped ZnO:Al (ZAO) thin films prepared by RF magnetron sputtering. *Appl. Surf. Sci.* **253,** 5179–5183 (2007).

123. Liu, K.-C., Lu, Y.-H., Liao, Y.-H. & Huang, B. Utilizing Transparent ZnO Thin Film as Permeation Barrier to Improve Light Outcoupling and Longevity of Top-Emission Polymer Light-Emitting Devices. *Jpn. J. Appl. Phys.* **47,** 3162–3166 (2008).

124. Liu, S.-J. *et al.* Physical properties of amorphous InGaZnO[sub 4] films doped with Mn. *Appl. Phys. Lett.* **94,** 092504 (2009).

125. Liu, S.-J., Su, S.-H., Fang, H.-W., Hsieh, J.-H. & Juang, J.-Y. Effects of Cr doping on physical properties of amorphous In–Ga–Zn–O films. *Appl. Surf. Sci.* **257,** 10018–10021 (2011).

126. Liu, X., Bi, W. & Liu, Z. Influence of post-annealing on the properties of Sc-doped ZnO transparent conductive films deposited by radio-frequency sputtering. *Appl. Surf. Sci.* **255,** 7942–7945 (2009).

127. Lu, X.-H. *et al.* Controllable Electrochemical Synthesis of Hierarchical ZnO Nanostructures on FTO Glass. *J. Phys. Chem. C* **113,** 13574–13582 (2009).

128. Ma, X., Zhang, J., Lu, J. & Ye, Z. Room temperature growth and properties of ZnO films by pulsed laser deposition. *Appl. Surf. Sci.* **257,** 1310–1313 (2010).

129. Majeed Khan, M. a., Wasi Khan, M., Alhoshan, M., AlSalhi, M. S. & Aldwayyan, a. S. Influences of Co doping on the structural and optical properties of ZnO nanostructured. *Appl. Phys. A* **100,** 45–51 (2010).

130. Malek, M. F. *et al.* Influence of various sol concentrations on stress/strain and properties of ZnO thin films synthesised by sol–gel technique. *Thin Solid Films* **527,** 102–109 (2013).

131. Mandal, S., Singha, R. K., Dhar, a. & Ray, S. K. Optical and structural characteristics of ZnO thin films grown by rf magnetron sputtering. *Mater. Res. Bull.* **43,** 244–250 (2008).

132. Marotti, R. E., Badán, J. a., Quagliata, E. & Dalchiele, E. a. Red photoluminescence and band edge shift from ZnO thin films. *Phys. B Condens. Matter* **398,** 337–340 (2007).

133. Millon, E. *et al.* Growth of heteroepitaxial ZnO thin films by femtosecond pulsed-laser deposition. *J. Appl. Phys.* **88,** 6937 (2000).

134. Ming-Dong, W. *et al.* Determination of Thickness and Optical Constants of ZnO Thin Films Prepared by Filtered Cathode Vacuum Arc Deposition. *Chinese Phys. Lett.* **25,** 743–746 (2008).

135. Mir, N., Salavati-Niasari, M. & Davar, F. Preparation of ZnO nanoflowers and Zn glycerolate nanoplates using inorganic precursors via a convenient rout and application in dye sensitized solar cells. *Chem. Eng. J.* **181-182,** 779–789 (2012).

136. Mishra, D. K. *et al.* Ferromagnetism in ZnO single crystal. *Phys. B Condens. Matter* **405,** 2659–2663 (2010).

137. Mohajerani, M. S., Lak, A. & Simchi, a. Effect of morphology on the solar photocatalytic behavior of ZnO nanostructures. *J. Alloys Compd.* **485,** 616–620 (2009).

138. Mohamed, S. & Ali, H. Effect of annealing and In content on the properties of electron beam evaporated ZnO films. *Eur. Phys. …* **99,** 95–99 (2005).

139. Moore, J. C., Covington, L. R. & Stansell, R. Affect of film thickness on the blue photoluminescence from ZnO. *Phys. Status Solidi* **209,** 741–745 (2012).

140. Mosbah, A. *et al.* Comparison of the structural and optical properties of zinc oxide thin films deposited by d.c. and r.f. sputtering and spray pyrolysis. *Surf. Coatings Technol.* **200,** 293–296 (2005).

141. Mouet, T. *et al.* Growth and characterization of thin ZnO films deposited on glass substrates by electrodeposition technique. *Appl. Surf. Sci.* **256,** 4114–4120 (2010).

142. Moustaghfir, A. & Tomasella, E. Structural and optical studies of ZnO thin films deposited by r.f. magnetron sputtering: influence of annealing. *Surf. Coatings …* **174-175,** 193–196 (2003).

143. Mridha, S. & Basak, D. Effect of thickness on the structural, electrical and optical properties of ZnO films. *Mater. Res. Bull.* **42,** 875–882 (2007).

144. Nagaraja, K. K., Pramodini, S., Poornesh, P. & Nagaraja, H. S. Effect of annealing on the structural and nonlinear optical properties of ZnO thin films under cw regime. *J. Phys. D. Appl. Phys.* **46,** 055106 (2013).

145. Nagaraju, J. & Krupanidh, S. B. Investigations on multimagnetron sputtered Zn[1−x]Mg[x]O thin films through metal-ferroelectric-semiconductor configuration. *J. Appl. Phys.* **104,** 043510 (2008).

146. Natsume, Y. & Sakata, H. Zinc oxide films prepared by sol-gel spin-coating. *Thin Solid Films* **372,** 30–36 (2000).

147. Natsume, Y. & Sakata, H. Electrical conductivity and optical properties of ZnO films annealed in hydrogen atmosphere after chemical vapor deposition. *J. Mater. Sci. Mater. …* **12,** 87–92 (2001).

148. Nayak, J., Kasuya, J., Watanabe, a & Nozaki, S. Persistent photoconductivity in ZnO nanorods deposited on electro-deposited seed layers of ZnO. *J. Phys. Condens. Matter* **20,** 195222 (2008).

149. Nehru, L. C., Swaminathan, V. & Sanjeeviraja, C. Rapid synthesis of nanocrystalline ZnO by a microwave-assisted combustion method. *Powder Technol.* **226,** 29–33 (2012).

150. Ng, Z.-N., Chan, K.-Y. & Tohsophon, T. Effects of annealing temperature on ZnO and AZO films prepared by sol–gel technique. *Appl. Surf. Sci.* **258,** 9604–9609 (2012).

151. Okazaki, R., Horikawa, A., Yasui, Y. & Terasaki, I. Photo-Seebeck Effect in ZnO. *J. Phys. Soc. Japan* **81,** 1–5 (2012).

152. Ozutok, F. & Demirselcuk, B. Study of Ultrasonically Sprayed ZnO Films: Thermal Annealing Effect. *Acta Phys. Pol. A* **121,** 53–55 (2012).

153. Pál, E., Seemann, T., Zöllmer, V., Busse, M. & Dékány, I. Hybrid ZnO/polymer thin films prepared by RF magnetron sputtering. *Colloid Polym. Sci.* **287,** 481–485 (2009).

154. Panda, S. K. & Jacob, C. Preparation of transparent ZnO thin films and their application in UV sensor devices. *Solid. State. Electron.* **73,** 44–50 (2012).

155. Pang, H. F. *et al.* Substrate-tilt angle effect on structural and optical properties of sputtered ZnO film. *Appl. Surf. Sci.* **259,** 747–753 (2012).

156. Pérez-Casero, R. *et al.* Er-doped ZnO thin films grown by pulsed-laser deposition. *J. Appl. Phys.* **97,** 054905 (2005).

157. Pradhan, D. & Leung, K. T. Controlled growth of two-dimensional and one-dimensional ZnO nanostructures on indium tin oxide coated glass by direct electrodeposition. *Langmuir* **24,** 9707–16 (2008).

158. Qiu, Z., Nadamura, Y. & Ishiguro, T. Formation of zinc oxide film by boiling metallic zinc film in ultrapure water. *Thin Solid Films* **518,** 5912–5915 (2010).

159. Ramírez, D. *et al.* Electrodeposition of ZnO thin films by using molecular oxygen and hydrogen peroxide as oxygen precursors: Structural and optical properties. *Sol. Energy Mater. Sol. Cells* **91,** 1458–1461 (2007).

160. Raoufi, D. & Raoufi, T. The effect of heat treatment on the physical properties of sol–gel derived ZnO thin films. *Appl. Surf. Sci.* **255,** 5812–5817 (2009).

161. Rusu, D., Rusu, G. & Luca, D. Structural characteristics and optical properties of thermally oxidized Zinc films. *Acta Phys. Pol. A* **119,** 850–856 (2011).

162. Saal, H. *et al.* Unusual optical properties of Mn-doped ZnO: the search for a new red pigment-a combined experimental and theoretical study. *Chemistry* **15,** 6408–14 (2009).

163. Sali, S., Boumaour, M., Kechouane, M., Kermadi, S. & Aitamar, F. Nanocrystalline ZnO film deposited by ultrasonic spray on textured silicon substrate as an anti-reflection coating layer. *Phys. B Condens. Matter* **407,** 2626–2631 (2012).

164. Saravanakumar, K. & Ravichandran, K. Synthesis of heavily doped nanocrystalline ZnO:Al powders using a simple soft chemical method. *J. Mater. Sci. Mater. Electron.* **23,** 1462–1469 (2012).

165. Saravanan, R., Francis, S. & Berchmans, J. L. Doping level of Mn in high temperature grown Zn1−x Mn x O studied through electronic charge distribution, magnetization, and local structure. *Chem. Pap.* **66,** 226–234 (2011).

166. Şenadim Tüzemen, E., Kavak, H. & Esen, R. Influence of oxygen pressure of ZnO/glass substrate produced by pulsed filtered cathodic vacuum arc deposition. *Phys. B Condens. Matter* **390,** 366–372 (2007).

167. Şenadım, E., Eker, S., Kavak, H. & Esen, R. Optical and structural parameters of the ZnO thin film grown by pulsed filtered cathodic vacuum arc deposition. *Solid State Commun.* **139,** 479–484 (2006).

168. Şenadim, E., Kavak, H. & Esen, R. The effect of annealing on structural and optical properties of ZnO thin films grown by pulsed filtered cathodic vacuum arc deposition. *J. Phys. Condens. Matter* **18,** 6391–6400 (2006).

169. Sharma, P. K., Pandey, A. C., Zolnierkiewicz, G., Guskos, N. & Rudowicz, C. Relationship between oxygen defects and the photoluminescence property of ZnO nanoparticles: A spectroscopic view. *J. Appl. Phys.* **106,** 094314 (2009).

170. Shinde, V. R., Gujar, T. P. & Lokhande, C. D. Studies on growth of ZnO thin films by a novel chemical method. *Sol. Energy Mater. Sol. Cells* **91,** 1055–1061 (2007).

171. Singh, P., Chawla, A. K., Kaur, D. & Chandra, R. Effect of oxygen partial pressure on the structural and optical properties of sputter deposited ZnO nanocrystalline thin films. *Mater. Lett.* **61,** 2050–2053 (2007).

172. Singh, P., Kumar, A. & Kaur, D. Growth and characterization of ZnO nanocrystalline thin films and nanopowder via low-cost ultrasonic spray pyrolysis. *J. Cryst. Growth* **306,** 303–310 (2007).

173. Singh, P., Kumar, A. & Kaur, D. ZnO nanocrystalline powder synthesized by ultrasonic mist-chemical vapour deposition. *Opt. Mater. (Amst).* **30,** 1316–1322 (2008).

174. Singh, P. *et al.* In situ high temperature XRD studies of ZnO nanopowder prepared via cost effective ultrasonic mist chemical vapour deposition. *Bull. Mater. Sci.* **31,** 573–577 (2008).

175. Smirnov, M., Baban, C. & Rusu, G. I. Structural and optical characteristics of spin-coated ZnO thin films. *Appl. Surf. Sci.* **256,** 2405–2408 (2010).

176. Sorar, I., Saygin-Hinczewski, D., Hinczewski, M. & Tepehan, F. Z. Optical and structural properties of Si-doped ZnO thin films. *Appl. Surf. Sci.* **257,** 7343–7349 (2011).

177. Tahar, R. B. H. & Tahar, N. B. H. Boron-doped zinc oxide thin films prepared by sol-gel technique. *J. Mater. Sci.* **40,** 5285–5289 (2005).

178. Talebian, N., Nilforoushan, M. R. & Maleki, N. Ultraviolet to visible-light range photocatalytic activity of ZnO films prepared using sol–gel method: The influence of solvent. *Thin Solid Films* **527,** 50–58 (2013).

179. Talebian, N., Nilforoushan, M. R. & Zargar, E. B. Enhanced antibacterial performance of hybrid semiconductor nanomaterials: ZnO/SnO2 nanocomposite thin films. *Appl. Surf. Sci.* **258,** 547–555 (2011).

180. Tan, S. T. *et al.* Blueshift of optical band gap in ZnO thin films grown by metal-organic chemical-vapor deposition. *J. Appl. Phys.* **98,** 013505 (2005).

181. Tan, S. T. *et al.* Realization of intrinsic p-type ZnO thin films by metal organic chemical vapor deposition. *J. Electron. Mater.* **34,** 1172–1176 (2005).

182. Tan, S. T. *et al.* Properties of polycrystalline ZnO thin films by metal organic chemical vapor deposition. *J. Cryst. Growth* **281,** 571–576 (2005).

183. Tanskanen, J. T., Bakke, J. R., Pakkanen, T. a. & Bent, S. F. Influence of organozinc ligand design on growth and material properties of ZnS and ZnO deposited by atomic layer deposition. *J. Vac. Sci. Technol. A Vacuum, Surfaces, Film.* **29,** 031507 (2011).

184. Tari, O. *et al.* Sol–gel synthesis of ZnO transparent and conductive films: A critical approach. *Sol. Energy Mater. Sol. Cells* **105,** 179–186 (2012).

185. Tong, H. *et al.* Effects of post-annealing on structural, optical and electrical properties of Al-doped ZnO thin films. *Appl. Surf. Sci.* **257,** 4906–4911 (2011).

186. Tricot, S. *et al.* Epitaxial ZnO thin films grown by pulsed electron beam deposition. *Surf. Sci.* **604,** 2024–2030 (2010).

187. Tsay, C.-Y., Fan, K.-S., Chen, C.-Y., Wu, J.-M. & Lei, C.-M. Effect of preheating process on crystallization and optical properties of sol-gel derived ZnO semiconductor thin films. *J. Electroceramics* **26,** 23–27 (2010).

188. Tsay, C.-Y., Fan, K.-S., Chen, S.-H. & Tsai, C.-H. Preparation and characterization of ZnO transparent semiconductor thin films by sol–gel method. *J. Alloys Compd.* **495,** 126–130 (2010).

189. Tsay, C.-Y. *et al.* Transparent semiconductor zinc oxide thin films deposited on glass substrates by sol–gel process. *Ceram. Int.* **36,** 1791–1795 (2010).

190. Tsay, C.-Y., Wang, M.-C. & Chiang, S.-C. Characterization of Zn1−x Mg x O Films Prepared by the Sol–Gel Process and Their Application for Thin-Film Transistors. *J. Electron. Mater.* **38,** 1962–1968 (2009).

191. Tüzemen, E. Ş., Eker, S., Kavak, H. & Esen, R. Dependence of film thickness on the structural and optical properties of ZnO thin films. *Appl. Surf. Sci.* **255,** 6195–6200 (2009).

192. Wang, T. *et al.* Low temperature synthesis wide optical band gap Al and (Al, Na) co-doped ZnO thin films. *Appl. Surf. Sci.* **257,** 2341–2345 (2011).

193. Wang, Y. G. *et al.* Comprehensive study of ZnO films prepared by filtered cathodic vacuum arc at room temperature. *J. Appl. Phys.* **94,** 1597 (2003).

194. Wang, Y. *et al.* Preparation and properties of surface textured ZnO: Al films by direct current pulse magnetron sputtering. *J. Mater. Sci. Mater. Electron.* **24,** 53–57 (2012).

195. Wei, X. Q., Huang, J. Z., Zhang, M. Y., Du, Y. & Man, B. Y. Effects of substrate parameters on structure and optical properties of ZnO thin films fabricated by pulsed laser deposition. *Mater. Sci. Eng. B* **166,** 141–146 (2010).

196. Xia, J., Lu, X., Wang, C., Tong, Y. & Chen, L. Electrochemical Assemble of Single Crystalline Twin ZnO Nanorods. *J. Electrochem. Soc.* **158,** D244 (2011).

197. Xue, S., Zu, X. & Xiang, X. Effects of Ge doping through ion implantation on the structural and optical properties of ZnO thin films prepared by sol-gel technique. *Int. J. …* **21,** 5257–5263 (2007).

198. Yang, C. *et al.* ZnO based oxide system with continuous bandgap modulation from 3.7 to 4.9 eV. *Appl. Phys. Lett.* **93,** 112114 (2008).

199. Yang, L., May, P. W., Yin, L. & Scott, T. B. Growth of self-assembled ZnO nanoleaf from aqueous solution by pulsed laser ablation. *Nanotechnology* **18,** 215602 (2007).

200. Yang, S., Liu, Y., Zhang, Y. & Mo, D. Investigation of annealing-treatment on structural and optical properties of sol-gel-derived zinc oxide thin films. *Bull. Mater. Sci.* **33,** 209–214 (2010).

201. Yang, S. & Zhang, Y. Structural, optical and magnetic properties of Mn-doped ZnO thin films prepared by sol–gel method. *J. Magn. Magn. Mater.* **334,** 52–58 (2013).

202. Yang, W., Li, Q., Gao, S. & Shang, J. K. NH4+ directed assembly of zinc oxide micro-tubes from nanoflakes. *Nanoscale Res. Lett.* **6,** 491 (2011).

203. Zhou, X., Zhang, Y., Shi, W. & Guo, T. Growth and properties of HfxZn1−xO thin films on flexible PET substrate using pulsed laser deposition. *J. Mater. Sci. Mater. Electron.* **24,** 362–367 (2012).

204. Jin, M., Feng, J., De-Heng, Z., Hong-lei, M. & Shu-ying, L. Optical and electronic properties of transparent conducting ZnO and ZnO:Al films prepared by evaporating method. *Thin Solid Film.* **357,** 98–101 (1999).

205. Nagase, T., Ooie, T. & Sakakibara, J. A novel approach to prepare zinc oxide films: excimer laser irradiation A novel approach to prepare zinc oxide films: excimer laser irradiation. *Thin Solid Films* **357,** 151–158 (1999).

206. *Handbook of Zinc Oxide and Related Materials*. (CRC Press: Florida, 2013).

207. Mitra, P., Chatterjee, A. P. & Maiti, H. S. ZnO thin film sensor. *Mater. Lett.* **35,** 33–38 (1998).

208. Rao, B. Zinc oxide semiconductor gas sensor for ethanol vapours. *Mater. Chem. Phys.* **64,** 62–65 (2000).

209. Birkmire, R. & Eser, E. Polycrystalline Thin Film Solar Cells: Present Status and Future Potential. *Annu. Rev. Mater. Sci.* **27,** 625–653 (1997).

210. Scheer, R., Walter, T., Schock, H. & Fearheiley, M. CuInS2 based thin film solar cell with 10.2% efficiency. *Appl. Phys. Lett.* **63,** 3294–3296 (1993).

211. Jager, S., Szyszka, B., Szczyrbowski, J. & Brauer, G. Comparison of transparent conductive oxide thin films prepared by a.c. and d.c. reactive magnetron sputtering. *Surf. Coatings Technol.* **98,** 1304–1314 (1998).

212. Yoshino, Y., Makino, T., Katayama, Y. & Hata, T. Optimization of zinc oxide thin film for surface acoustic wave filters by radio frequency sputtering. *Vacuum* **59,** 538–545 (2000).

213. Allsopp, H. J. & Roberts, J. P. Non-Stoichiometry of Zinc Oxide and its Relation to Sintering. *Trans. Faraday Soc.* **55,** 1386–1393 (1959).

214. Urbach, F. The Long-Wavelength Edge of Photographic Sensitivity and of the Electronic Absorption of Solids. *Phys. Rev.* **92,** 1324 (1953).

215. Voss, C. *et al.* Growth Kinetics of Thin-Film Cadmium Sulfide by Ammonia-Thiourea Based CBD. *J. Electrochem. Soc.* **151,** C655 (2004).

216. Chang, Y.-J. *et al.* Nanocrystalline CdS MISFETs Fabricated by a Novel Continuous Flow Microreactor. *Electrochem. Solid-State Lett.* **9,** G174 (2006).

217. Mugdur, P. H. *et al.* A Comparison of Chemical Bath Deposition of CdS from a Batch Reactor and a Continuous-Flow Microreactor. *J. Electrochem. Soc.* **154,** D482 (2007).

218. Paul, B. K. *et al.* A Uniform Residence Time Flow Cell for the Microreactor-Assisted Solution Deposition of CdS on an FTO-Glass Substrate. *Cryst. Growth Des.* **12,** 5320–5328 (2012).

219. Chang, Y.-J., Su, Y.-W., Lee, D.-H., Ryu, S. O. & Chang, C.-H. Investigate the Reacting Flux of Chemical Bath Deposition by a Continuous Flow Microreactor. *Electrochem. Solid-State Lett.* **12,** H244 (2009).

220. Chang, Y.-J., Lee, D.-H., Herman, G. S. & Chang, C.-H. High-Performance, Spin-Coated Zinc Tin Oxide Thin-Film Transistors. *Electrochem. Solid-State Lett.* **10,** H135–H138 (2007).

221. Li, J. *et al.* The length controllable synthesis and near-infrared photoluminescence of one-dimensional ternary Cu4Bi4S9 semiconductor nanobelts. *Mater. Res. Bull.* **49,** 180–186 (2014).

222. Li, J. *et al.* One dimensional ternary Cu–Bi–S based semiconductor nanowires: synthesis, optical and electrical properties. *J. Mater. Chem.* **22,** 17813–17819 (2012).